Characterization of extrasolar multi-planet systems by transit timing variation

Inaugural-Dissertation
zur
Erlangung des Doktorgrades
der Mathematisch-Naturwissenschatlichen
Fakultät
der Universität zu Köln

vorgelegt von
Judith Korth
aus Mönchengladbach

Mönchengladbach
2020

Berichterstatter/in:	PD Dr. Martin Pätzold
	Prof. Dr. Joachim Saur
Tag der mündlichen Prüfung:	22.04.2020

"Phantasie ist wichtiger als Wissen, denn Wissen ist begrenzt."

-A. Einstein-

Kurzzusammenfassung

Die Kenntnis der inneren Struktur, Zusammensetzung und Dichteverteilung von Exoplaneten ist wesentlich für das Verständnis der Entstehung, Migration und Evolution von Planetensystemen. Planetensysteme mit transitierenden Planeten eignen sich hervorragend für diese Charakterisierung, da sie die Messung des Planetenradius ermöglichen, der für die Bestimmung der Evolution des Planeten sowie seiner inneren Struktur unerlässlich ist. Der zweite entscheidende Parameter neben dem Planetenradius ist die Planetenmasse, die in Kombination mit dem Planetenradius die Bestimmung der Raumdichte des Planeten ermöglicht, die wiederum Rückschlüsse auf seine mögliche Zusammensetzung erlaubt. Allerdings sind präzise Messungen der Planetenmasse oft schwierig, vor allem für kleine Planeten. Jedoch können die Planetenmassen, sobald mehrere Planeten in einem System sind, durch Variationen in den Transitzeiten bestimmt werden. Da die Änderungen in den Transitzeiten hauptsächlich durch die Gravitationswechselwirkung zwischen den Planeten verursacht werden, können die Planetenparameter einschließlich der Massen der Planeten durch die Inversion des Transitzeitensignals bestimmt werden.

Die vorliegende Arbeit charakterisiert extrasolare Mehrplanetensysteme anhand der Änderungen ihrer Transitzeiten. Im Rahmen dieser Arbeit, wurde mit Python Tool for Transit Variations (`PyTTV`) ein OpenSource-Programm entwickelt, das (1) Transitvariationen suchen und identifizieren

kann und (2) die Parameter von Planeten in Mehrplanetensystemen mithilfe der Änderungen in den Transitzeiten bestimmen kann. `PyTTV` ist in der Lage, die zunehmende Anzahl von Lichtkurven, die eine manuelle Suche erschwert, zu verarbeiten. Das Programm eignet sich bestens, um nach Variationen in Lichtkurven zu suchen, die mit verschiedener zeitlicher Auflösung, mit unterschiedlichen Rauscheigenschaften und von verschiedenen Teleskopen aus beobachtet werden. Dadurch ist `PyTTV` hervorragend für die Suche nach Transitvariationen mit aktuellen und zukünftigen Instrumenten geeignet. `PyTTV` bestimmt die Parameter eines Planeten in einem Mehrplanetensystem mittels einer n-body Integration, die die Gravitationskräfte zwischen den Körpern, den Einfluss von allgemein relativistischen Effekten und der Gezeitenwechselwirkungen berücksichtigt.

Es wird zum einen gezeigt, dass `PyTTV` Änderungen in den Transitzeiten auf kurzen Zeitskalen in Systemen detektieren kann (Kepler-9, K2-146 und Kepler-88, Kepler-117, Kepler-693, Kepler-448), sowie zudem Änderungen auf längeren Zeitskalen aufspüren kann, wie für WASP-18, HAT-P-7 und Kepler-13 präsentiert. Zum ersten Mal werden hier die Ergebnisse der Suche nach Änderungen in den Transitzeiten für die Systeme TOI-1130, TOI-1136 and WASP-126 unter Berücksichtigung aller verfügbaren Lichtkurven präsentiert; für die Systeme Kepler-448, HAT-P-7, and Kepler-13 wurden erstmalig die Lichtkurven von Kepler und TESS zusammen untersucht. Gezeigt wird zum anderen, dass `PyTTV` die Planetenparameter anhand der Änderungen der Transitzeiten und -dauern sowie der Hinzunahme von Radialgeschwindigkeitsmessungen bestimmen kann. Diese Analysen wurden für das Kepler-9 System, das Kepler-289 System und das K2-146 durchgeführt und werden hier zum ersten Mal vorgestellt.

Abstract

Knowledge of the structure and composition of extrasolar planets is a key element for understanding how planetary systems form and evolve. Planetary systems with transiting planets are markedly well-suited for this characterization, since they allow the measurement of the planetary radius, which is essential to constrain the planet's evolution and migration history, as well as to characterize the internal structure of the planet. The second fundamental parameter for the characterization is the planetary mass, that together with the radius allows the bulk density of a planet to be estimated, thereby constraining its composition. However, precise measurements of the planetary mass are difficult to obtain, in particular for small planets. If there are multiple planets in a system, the planetary masses can be determined using transit timing variations (TTVs). Since TTVs are mainly caused by the gravitational interaction between the planets, the planetary parameters including their masses can be estimated by inverting the transit timing variation signal.

This thesis focuses on the characterization of extrasolar multi-planet systems using TTVs. An open-source package, Python Tool for Transit Variations (`PyTTV`), was developed to (1) search and identify transit variations and (2) estimate the physical quantities of planets in multi-planet systems based on the derived TTVs. `PyTTV` is able to process the increasing amount of light curves from past, current, and upcoming exoplanet

missions for which a manual search is impractical. `PyTTV` is suitable for the search of variations in light curves observed in different cadences, with different noise properties, and from different telescopes, putting it in an excellent position for the search of transit variations using current and upcoming facilities. `PyTTV` determines the physical quantities of planets in multi-planet systems by an n-body orbit integration which considers the gravitational forces, the effects of general relativity, and tidal interactions.

This thesis shows that `PyTTV` can (1) detect short-term transit variations in systems with either planets close to a mean-motion-resonance (Kepler-9, and K2-146, Kepler-88) or far away from it (Kepler-117, Kepler-693, Kepler-448), as well as long-term transit variations as presented for WASP-18b, HAT-P-7b and Kepler-13Ab. For the first time, a TTV search has been carried out for the systems TOI-1130, TOI-1136, and WASP-126 using all the available *TESS* light curves. Kepler-448, HAT-P-7, and Kepler-13A are searched for variations using *Kepler* and *TESS* light curves combined for the first time. Furthermore, it is shown, that (2) `PyTTV` is able to estimate planetary parameters by simultaneously modeling transit timing variations, transit duration variations, and radial velocity observations. The simultaneous modeling of transit timing variations, transit duration variations, and radial velocity observations has been carried out for the Kepler-9, Kepler-289 and K2-146 systems and is presented in this thesis for the very first time.

Contents

1 Introduction **1**

2 Characterization of extrasolar planetary systems **11**

3 Transit Variations **21**

3.1 Transit Timing Variations 24

3.1.1 Orbital precession 26

3.1.2 Orbital decay 30

3.1.3 Time scales 32

3.1.4 Application 35

3.2 Transit Duration Variations 40

3.3 Challenges 41

4 PyTTV: Detection of Transit Variations **47**

4.1 Estimation of Transit Center Times, Durations, and Depths 50

4.1.1 Data download 51

4.1.2 Initial transit estimation 52

4.1.3 Simultaneous transit modeling 52

4.1.4 Individual transit modeling 54

4.2 Identification of Variations 58

4.3 Validation of PyTTV 63
4.4 New TTV systems with PyTTV 81
4.4.1 Non Detection of TTVs 82
4.4.2 Detection of TTVs 90
4.4.3 Conclusions 106

5 PyTTV: Estimation of physical quantities 109
5.1 Parameter estimation 111
5.1.1 Formalism 112
5.1.2 Priors 114
5.2 Characterization of the Kepler-9 system 116
5.3 Characterization of the Kepler-289 system 127
5.4 Characterization of the K2-146 system 139

6 Summary and future prospects 145
6.1 Summary of the results 147
6.2 Future prospects 155

Appendices 159

A Abbreviations 161

Bibliography 165

Acknowledgments 195

Erklärung 197

List of Figures

2.1 Transit diagram 15

3.1 TTV diagram 25
3.2 Main contributions to the orbital precession 33
3.3 Tidal and rotational contributions to the orbital precession . 35
3.4 Transit shifts caused by orbital decay 36
3.5 TTV vs. RV 43

4.1 Kepler-9: Light curve 51
4.2 Initial transit center estimates 53
4.3 Kepler-9: Phase-folded transits 53
4.4 Simultaneous transit modeling 54
4.5 Difference in transit center estimates 56
4.6 Accuracy of the transit center estimates 57
4.7 Kepler-9: TTVs 59
4.8 Kepler-9: TDVs and TPVs 60
4.9 Kepler-9: Periodogram 61
4.10 Kepler-117: TTVs 65
4.11 Kepler-117: Periodogram 67
4.12 Kepler-693: TTVs, TDVs and TPVs 70
4.13 Kepler-88: TTVs and TDVs 73

4.14 Kepler-88: Periodogram 74
4.15 TOI-193: TTVs 76
4.16 WASP-18: TTVs, TDVs and TPVs 79
4.17 WASP-18: Long-term TTVs 81
4.18 K2-180: TTVs 84
4.19 Keper-106: Simultaneous transit modeling 86
4.20 TOI-1136: TTVs 90
4.21 WASP-126: TTVs 91
4.22 K2-146: TTVs 93
4.23 Kepler-448: TTVs, TDVs and TPVs 94
4.24 HAT-P-7: TTVs, TDVs and TPVs 97
4.25 HAT-P-7: TPVs 99
4.26 Kepler-13Ab: TTVs, TDVs and TPVs 103

5.1 Coordinate system 113
5.2 Eccentricity priors 115
5.3 Kepler-9: Planet mass vs. eccentricity prior 118
5.4 Kepler-9: Eccentricity priors 119
5.5 Kepler-9: Estimated parameters 121
5.6 Kepler-9: Best-fit TTVs 126
5.7 Kepler-9: Best-fit RVs 126
5.8 Kepler-289: TTVs 130
5.9 Kepler-289: Estimated parameters 134
5.10 Kepler-289: Best-fit TTVs and RVs 138
5.11 K2-146: Estimated parameters 141
5.12 K2-146: Best-fit TTVs 143

6.1 Mass vs. Radius 153

6.2 Mass vs. Density 154

List of Tables

1.1 Abbreviations 10

3.1 Reference values 34

4.1 Kepler-9:Diagnostics 63
4.2 Kepler-117: Diagnostics 68
4.3 Kepler-693: Diagnostics 71
4.4 Kepler-88: Diagnostics 75
4.5 TOI-193.01 and WASP-18b: Diagnostics 80
4.6 K2-180: Diagnostics 83
4.7 K2-140: Diagnostics 85
4.8 K2-100: Diagnostics 85
4.9 K2-106: Diagnostics 87
4.10 TOI-263: Diagnostics 88
4.11 TOI-1130: Diagnostics 89
4.12 TOI-1136: Diagnostics 89
4.13 WASP-126: Diagnostics 90
4.14 K2-146: Diagnostics 95
4.15 Kepler-448: Diagnostics 96
4.16 HAT-P-7: Diagnostics 100
4.17 Kepler-13Ab: Diagnostics 105

5.1 Kepler-9: Estimated parameters 125
5.2 Kepler-289: Diagnostics 131
5.3 Kepler-289: Estimated parameters 137
5.4 K2.146: Estimated parameters 144

A.1 Symbols 161

1

Introduction

Since centuries people have been asking the question of whether there are other Earth-like planets in our universe or not. And if yes, do these planets resemble the Earth in the Solar System or is the Solar System unique? These fundamental questions began the search for planets outside the Solar System (extrasolar planets). Since the announcement of the first extrasolar planet around the neutron star PSR1257+12 (Wolszczan & Frail, 1992), and of the first exoplanet around a sun-like star (51 Pegasi) by Nobel prize laureates D. Queloz and M. Mayor 1995 (Mayor & Queloz, 1995), the speed of discoveries has increased dramatically.

The direct optical detection of an extrasolar planet via direct imaging is difficult, and so far only possible within the accretion disk. However, they can be detected indirectly through their influence on the host star, e.g., by radial velocity (RV) or transit observations. In the first case, the planet influences the motion of the star, and in the second case, the planet influences the brightness of the star when it is transiting in front of the star.

The numerous indirect discoveries were possible thanks to various space-based missions and ground-based facilities: Hungarian Automated Telescope Network (*HATNet;* Bakos et al., 2004), Wide Angle Search for Plan-

ets (*WASP*; Pollacco et al., 2006), *MEarth* (Nutzman & Charbonneau, 2008), COnvection, ROtation and planetary Transits (*CoRoT*; Auvergne et al., 2009), *Kepler* (Borucki et al., 2010), The Kilodegree Extremely Little Telescope (*KELT*; Siverd et al., 2012), *K2* (Howell et al., 2014), and Transiting Exoplanet Survey Satellite (*TESS*; Ricker et al., 2014), and Next-Generation Transit Survey (*NGTS*; Wheatley et al., 2018).

The extrasolar planetary systems discovered to date are diverse and show a wide range of evolutionary states but the detection of an Earth twin or a counterpart to the Solar System is still pending. The diversity is one of the main discoveries in exoplanet research. Some planets orbit their star on very eccentric orbits ($e > 0.3$), while other extrasolar planets are located on orbits that have much shorter distances from their star than Mercury is orbiting the Sun (0.39 AU). Not only the orbits of the planets show a high diversity, but the extrasolar planets also differ in their inner structure, composition, and mass. The diversity ranges from small evaporating comet-like objects with rapidly varying dust halos and tails to massive gas giants close to the brown dwarf regime. Against this background, the question arose which objects can be called planets, answered by the Working Group on Extrasolar Planets of the International Astronomical Union: a planet is defined as an object with mass below the mass limit for thermonuclear fusion of deuterium ($< 13\ M_{\mathrm{Jup}}$). This definition can be seen as a working definition that will evolve as the knowledge about extrasolar planets improves. The stars themselves show an equally wide variety. Not only main sequence stars like the Sun host planets, but also low-mass stars, giants, white dwarfs, and pulsars (see the Hertzsprung-Russel diagram). Because of their high diversity, the extrasolar planets and sub-stellar objects provide insights into the different evolutionary states of planetary systems. Thus, they give the opportunity to understand the Solar System and hence

the question of the uniqueness of the Earth.

While novel discoveries are ongoing, exoplanetary science has now entered the era of characterization and the focus is shifting from detection to characterization to understanding the formation and dynamics of these systems. Studying the dynamical interaction in a planetary system is important for understanding the evolution of planetary systems, and various theories have been developed to explain the observed diversity in orbital configurations and planetary densities (Super-Earth, Sub-Neptune, hot Jupiter, warm Jupiter, ultra-short-period (USP) planets) (e.g Petrovich et al., 2014; Petrovich & Tremaine, 2016; Sotiriadis et al., 2017). These theories rely on the currently characterized systems, in particular on the accuracy with which the masses and orbital parameters are determined.

The majority of the currently known exoplanets are transiting exoplanets detected by the *Kepler* mission. Transiting exoplanets, planets that periodically cross in front of their host stars, are valuable targets for further characterization since they allow the measurement of their true planetary masses, radii, orbital obliquities, and atmospheres. Knowledge of these properties is crucial for the detailed characterization of a planet. Without planetary masses and radii, the density of the planet cannot be determined and therefore the internal structure stays inaccessible. Additionally, the characterization of the atmosphere requires knowledge of the planetary mass for deriving the scale height, a parameter that is in turn essential for interpreting transmission spectroscopy observations.

RV and transit method are the two methods mainly used for this characterization. The RV method estimates the planetary minimum mass while the transit method measures the planet to star radius ratio and the orbital inclination. The former method spectroscopically observes the line-of-sight component of the stellar reflex motion induced by the planet, mea-

suring the Doppler shift of the stellar spectral lines very precisely. The latter method photometrically detects the decrease in the stellar flux that occurs when a planet crosses the stellar disk. The true planetary mass and thus, the planetary bulk density is determined by combining both methods. In contrast to the Solar System, where the internal density distribution can be determined by measuring the higher-order gravitational field coefficients with spacecrafts as carried out for, e.g., for Venus using line of sight *Magellan* residual Doppler data (Barriot et al., 1998), for the Mars moon Phobos using *Mars Express* radio-tracking data (Andert et al., 2010), and for the comet 67P/Churyumov-Gerasimenko using *Rosetta* radio-tracking data (Pätzold et al., 2019), for exoplanets only interior models are used without direct measurements.

Unfortunately, only a few of the known small planets have measured masses with high-enough accuracy to constrain their physical nature, e.g., their composition. In contrast, orbital periods and planetary radii are well measured making these two properties the best-studied parameters so far. Some fascinating discoveries have been made by characterizing the *Kepler* sample by statistical studies: the radius gap possibly sculpted by photoevaporation (Fulton et al., 2017; Fulton & Petigura, 2018); the occurrence rate of planets concerning their sizes and orbital periods (Petigura et al., 2013; Zhu et al., 2018); the orbital period distribution (Lissauer et al., 2011; Fabrycky et al., 2014; Malhotra, 2015; Steffen & Hwang, 2015), the low mutual inclinations of compact multi-planet systems (Fabrycky et al., 2014; Steffen & Hwang, 2015), and their eccentricity distribution (Xie et al., 2016).

Another result from the *Kepler* mission is that multi-planet systems seem to be common (Lissauer et al., 2012; Fabrycky et al., 2014; Rowe et al., 2014). Most of the detected multi-planet systems reside in compact

configurations where the planets interact gravitationally with each other. These systems come with many unknowns. What do we know about the existence, formation, and evolution of these planets? What is the main reason for their current configuration? Will they remain in their current orbits, or do their orbits become chaotic? By studying the dynamics of these multi-planet systems it becomes clear that the existence of long period and/or inclined planets plays a critical role in their formation (Hands & Alexander, 2016; Lai & Pu, 2016; Pu & Lai, 2018; Becker & Adams, 2017; Contreras & Boley, 2018; Mills et al., 2019; Denham et al., 2019; Xu & Fabrycky, 2019; Huang et al., 2017). Massive outer planets are essential for the evolution of planetary systems; they are often crucial to stabilize or destabilize the inner planets. For example, the inner Solar System is gravitationally dominated by Jupiter.

The strong gravitational interaction between the planets in compact multi-planet systems leads to deviations in the observed transit times and durations (transit timing variations (TTVs) and transit duration variations (TDVs); Agol et al., 2005; Holman & Murray, 2005; Agol & Fabrycky, 2018). The deviations are observable in their light curves depending on the orbital configuration, and are the strongest when the orbital periods of the planets are close to a commensurability. The system properties, like planetary mass and orbital parameters, are embedded in these deviations. Thus, measurements of these deviations reveal the orbital architecture.

The first application of TTVs was in the 19th century in the Solar System. Neptune was detected via its perturbations on the other planets and its mass and position were estimated by inverting the interaction (Adams, 1846; Le Verrier, 1877). Nowadays, one of the most used applications of TTVs is the determination of the masses, and therefore the densities, of planets that have host stars which are too faint for characterization via

RV observation (Xie, 2013, 2014; Jontof-Hutter et al., 2016; Hadden & Lithwick, 2016, 2017; Hadden et al., 2019). Besides, TTVs are sensitive to low-mass planets below the current RV detection limit, as well as to non-transiting planets and therefore, gain knowledge about systems that are inaccessible with other techniques. For these reasons, TTVs are often the best method to characterize multi-planet systems.

Since the launch of *Kepler* in 2009, the search for light curve variations has increased dramatically. An advantage of transit observations from space is that a continuous observation can be carried out over a long time. Without the Earths' observation-disturbing atmosphere and the day-night changes, precise uninterrupted light curves of the stars can be observed, which allow the detection of small variations in the transit. The *Kepler* sample with its long observational time span has revealed up to now not only the first transiting multi-planet system, Kepler-9 (Holman et al., 2010), but also the largest number of systems exhibiting TTVs (Holczer et al., 2016; Kane et al., 2019; Gajdoš et al., 2019).[1]

WASP-47 is an example of a system exhibiting TTVs with a complex architecture that has been studied in more detail. It consists of different planetary types: a hot Jupiter with outer and inner sub-Neptune planets and a long-period eccentric giant planet. This system shows similarities to the Solar System: the planets are diverse in composition, are on coplanar and nearly circular orbits, and also in an orbital configuration not trapped in resonance (Weiss et al., 2017). K2-146 is another dynamically fascinating TTV system. K2-146 is a compact multi-planet system with two Neptune-sized planets likely trapped in a 3:2 MMR that shows interesting dynamical evolution, where the outer planet K2-146c changes its orbital

[1] The first extrasolar planet system with one transiting planet and another non-transiting planet was HAT-P-13 (Bakos et al., 2009).

plane during the span of the observations from *K2* (2014-2018) (Hamann et al., 2019; Lam et al., 2020).

An interesting feature has been discovered by using the TTV method to extract the masses and densities, the so-called "puffy planets" (e.g. Masuda, 2014; Jontof-Hutter et al., 2017). "Puffy planets" are planets that have a very low mass for their size and therefore extremely low densities. Additional measurements and updated stellar parameters can significantly reduce the uncertainties in the derived planet masses (e.g. Vissapragada et al., 2020) and thus, lead to more robustly estimated planetary masses.

Moreover, additional measurements (transit or RV) can help to solve ambiguities and uniquely characterize the planet system. The combination with RV observations, if possible, offers the best chance to find the cause of the TTVs. RV measurements also allow the detection of non-transiting planets and the determination of their minimum masses. The combination of TTV and RV observations was not possible for most of the *Kepler* discoveries, since most of the *Kepler* stars are too faint for RV observations. Fortunately, this changed with the launch of the *TESS*, and the combination of TTV with RV measurements is feasible on large scale for the first time. Therefore, the characterization and study of the dynamical evolution of the systems containing smaller planets has started.

However, the orbits of planets in some exoplanet systems cannot be explained purely by gravitational perturbations. The orbit of a planet can undergo orbital precession also due to general relativistic effects, non-sphericity, and tidal interactions. Therefore, it is necessary to consider additional forces, such as general relativistic effects and tidal interactions. This is in particular essential for systems with USP planets or very compact multi-planet systems. HD 209458b works as a prime example where the inclusion of tidal forces leads to different orbital solutions (Mardling,

2007; Laskar et al., 2012). Delisle et al. (2017) showed that the spin can be forced into non-synchronous or chaotic state via planet-planet perturbations and that TTVs are well suited to study the spin dynamics. Moreover, Essick & Weinberg (2015) noted that WASP-19b undergoes orbital decay, and therefore a shift in the transit center times might be detectable in a few years. Although transit times for WASP-12b were identified to have a quadratic trend (Maciejewski et al., 2016, 2018), the trend cannot uniquely be attributed to orbital decay. The shift in the transit times can also be a result of long-term perturbations caused by either tidally induced orbital precession (Maciejewski et al., 2016; Patra et al., 2017; Bailey & Goodman, 2019) or dynamical interactions with a planetary companion (Maciejewski et al., 2018; Bailey & Goodman, 2019). The unambiguous differentiation between orbital decay and precession requires a few more years of monitoring. Altogether, most studies with the focus on the detectability of long-term perturbations of planetary orbits concluded that the effect of orbital perturbations would be measurable within a time span of ten years. Combining *Kepler* and *TESS* light curves, and in the future light curves from the CHaracterising ExOPlanets Satellite (*CHEOPS;* Fortier et al., 2014) and PLAnetary Transits and Oscillations of stars (*PLATO*; Rauer et al., 2014), produces the perfect data set to search for these long-term perturbations.

This thesis focuses on the characterization of extrasolar multi-planet systems using transit timing variations. The thesis begins with an outline of the characterization of extrasolar planets, and gives a short summary about the transit and RV method, the two widely used methods for the characterization of extrasolar planets (Chpt. 2). The chapter continues with an overview about multi-planet systems and their characterization method, transit variations, that is explained in more detail in Chpt. 3, with

a particular focus on transit timing variations. The next chapters deal with the scientific part of the thesis. First, Chpt. 4 focuses on the search and identification of transit variations. Next, Chpt. 5, details the characterization and parameter estimation of multi-planet systems. The latter two chapters present novel work carried out with an open-source Python Tool for Transit Variations (`PyTTV`) developed within the framework of the thesis. This tool combines the search and identification of transit variations with the inversion of the variations, that is, the parameter estimation from the variation signal. Several multi-planet systems are searched for variations using the *Kepler* and *TESS* photometry. Some results are novel work, some analyses have been presented in publications, and some analyses extend the published analyses from other authors and are compared with them. The parameter estimation is carried out for three systems that are modeled simultaneously with all available observations for the first time. The science chapters share a common structure, starting with an introduction describing the research case, followed by the presentation of the analyses carried out within this thesis, and concluding with results and discussion. Chapter 6 discusses and summarizes the main findings of the thesis.

A list with all the abbreviations used in the thesis is given in Table 1.1

Table 1.1.: Abbreviations and their corresponding definition used in the text.

Abbreviation	Definition
BIC	Bayesian Information Criterion
CHEOPS	CHaracterising ExOPlanets Satellite
CoRoT	COnvection, ROtation and planetary Transits
FAP	False Alarm Probability
FFI	Full Frame Image
GLS	Generalized Lomb-Scargle
GP	Gaussian Process
GR	General Relativity
HATNet	Hungarian Automated Telescope Network
KELT	The Kilodegree Extremely Little Telescope
KOI	Kepler Object of Interest
MCMC	Markov Chain Monte Carlo
MMR	Mean-Motion Resonance
NGTS	Next-Generation Transit Survey
PDCSAP	Pre-Search Data Conditioning Simple Aperture Photometry
PH	Planet Hunters
PLATO	PLAnetary Transits and Oscillations of stars
PyTTV	Python Tool for Transit Variations
Q	Quarter
RV	Radial Velocity
S/N	Signal-to-Noise
TESS	Transiting Exoplanet Survey Satellite
TOI	Tess Object of Interest
TTV	Transit Timing Variation
TDV	Transit Duration Variation
TPV	Transit dePth Variation
USP	Ultra-Short-Period
WASP	Wide Angle Search for Planets

2

Characterization of extrasolar planetary systems

Planetary systems with transiting planets are markedly well-suited for their characterization. Transiting planets allow the measurement of the planetary radius, which is essential to constrain the planet's evolution and migration history. The radius also provides constraints on the planet's composition and atmosphere through evolutionary models. Further, combining transit measurements with RVs delivers the true planetary mass, because the inclination of the transiting planet, i, can be determined, and hence also the true mass of the planet. In order to estimate the absolute dimensions of the system, like the planetary radius $R_{\rm p}$ and the planetary mass $M_{\rm p}$, the stellar parameters, like the effective temperature, surface gravity, and metallicity, need to be known to high precision. These parameters are usually obtained spectroscopically. In addition, also the stellar luminosity and spectral type can be derived. Stellar mass, radius, and age are usually derived by the comparison of the observed data with stellar evolution models, e.g., BAyesian STellar Algorithm (Silva Aguirre et al., 2015), and Spectroscopy Made Easy (SME; Piskunov & Valenti, 2017). Astrometric

measurements (e.g. *Gaia*; Brown et al., 2018) and asteroseismology can also help to constrain some stellar parameters. This means that the planetary parameters depend always on the accuracy with which the stellar parameters can be estimated.

The planetary mass and radius provide an estimate of the bulk density of a transiting planet, thereby constraining its possible composition. However, the internal planetary structure is ambiguous and not fully determined by the planetary bulk density. One solution is the direct measurement of an additional observable (e.g. the fluid Love number $k_{2,\mathrm{p}}$ as in (Patra et al., 2017; Csizmadia et al., 2019).

Two methods mainly used to measure the planetary mass and radius are the transit and RV method.

Radial velocity Measuring the RV variations of a star as it moves around the center of the mass of the star-planet system is the most reliable method to determine the minimum mass of a planet $M_{\mathrm{p}} \sin i$ (Hatzes, 2016b). This velocity variation is measured through the Doppler effect, that is, the shift in the wavelength of spectral lines due to the motion of the star (Hatzes, 2016a). The amplitude of the RV signal, K, induced by a planet on its host star is (Cumming et al., 1999)

$$K = \left(\frac{2\pi G}{P_{\mathrm{orb}}}\right)^{1/3} \frac{M_{\mathrm{p}} \sin i}{(M_\star + M_{\mathrm{p}})^{2/3}} \frac{1}{\sqrt{1-e^2}}, \tag{2.1}$$

where G the Newtonian gravitational constant, P_{orb} the orbital period of the planet, $M_\star$ the stellar mass, M_{p} the planetary mass, and e the orbital eccentricity (see Table A.1 for a list of all variables). However, the determination of the planetary mass depends on the stellar mass. The RV

method measures small velocity variations of a star that can be attributed to the existence of orbiting planets. This technique is most sensitive to massive planets on short orbital periods, but the current accuracy of the instruments ($\sim 10\,\mathrm{cm\,s^{-1}}$) allows also the detection of low-mass planets (Hernández et al., 2018).

The direction of the planetary orbit, e.g., prograde or retrograde, can be obtained from RV observations during transits. When a transiting planet crosses the stellar disc, an anomalous RV signal is generated due to the occultation of portions of the rotationally Doppler-shifted star. When the planet overlaps the blueshifted part of the stellar disk, the integrated starlight becomes redshifted, and vice versa (Winn, 2010). This effect is known as the Rossiter-McLaughlin effect (Rossiter, 1924; McLaughlin, 1924) due to stellar rotation, and is sensitive to the projected angle between the stellar spin axis and the orbital plane of the planet, λ. The signal for an aligned planet is antisymmetric about the transit center time, while a misaligned planet produces an anomalous shift. The Rossiter-McLaughlin effect is difficult to measure and was observed only for a few planet systems.

Another physical quantity that can be measured via RVs is the orbital eccentricity. Eccentricities are fundamental to understand the evolution and formation of planetary systems.

One drawback of the RV method is that the method measures only $M_\mathrm{p} \sin i$ for non-transiting planets. Even for transiting planets of low mass, it is often difficult to determine the masses using the RV method alone, since the signal scales with the planet mass. In addition, the ability for accurate mass measurements depends on the star itself; the uncertainty of the RVs increases with the increase of the stellar mass and for rapidly rotating stars. Moreover, the RV method requires long-term

observations of individual stars with large telescopes and highly stable instruments. Since the RV method depends upon precise measurements of small shifts in spectral lines that demand high signal-to-noise (S/N) ratio and narrow, non-broadened lines, RV measurements are useful only for a subset of planets orbiting bright and slowly-rotating stars. Methods that were cheaper, and easier to automatize were developed to compensate for the shortcomings of the RV surveys.

Transit method A planet crossing in front of the stellar disc blocks a part of the star and leads to a dip in its observed brightness, as described by e.g. Struve (1952). Depending on the size of the planet relative to the star, the light decrement can be percents of the apparent brightness of the star. Transiting planets are of particular interest, since their light curves allow to determine their radii. Furthermore, they allow the exploration of the planetary structure and atmospheric properties from photometry and spectroscopy during the transit.

Three geometric parameters describe the duration and shape of the transit in addition to the orbital period $P_{\rm orb}$ (Seager & Mallen-Ornelas, 2003; Winn, 2010). Assuming both the planet and the star to be spherical, and also assuming negligible flux from the planet, the transit depth ΔF (Fig. 2.1) is related to the ratio of the

$$\Delta F \sim k^2 = \left(\frac{R_{\rm p}}{R_\star}\right)^2, \tag{2.2}$$

where the transit depth, ΔF, would equal to the squared radius ratio, $(R_{\rm p}/R_\star)^2 = k^2$, if the stellar limb darkening could be ignored (Seager & Mallen-Ornelas, 2003; Winn, 2010). The duration of a transit is determined by the length of the transit chord in front of its host star divided by

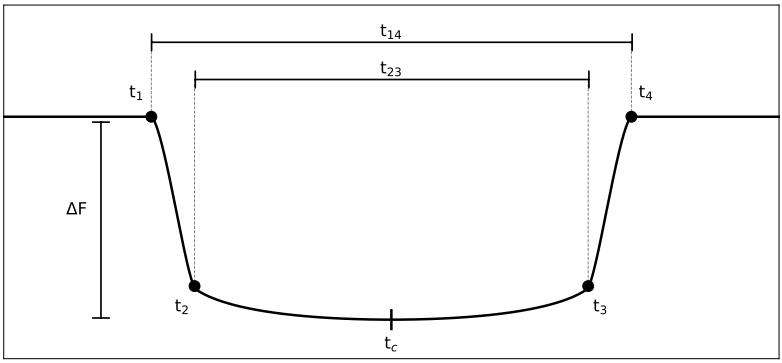

Figure 2.1.: Diagram of the transit shape of a limb-darkened transit light curve. The symbols t_1 and t_4 mark the times of first and last contact points, respectively. The symbols t_2 and t_3 mark the end of ingress and the start of egress, respectively. The time $t_{14} = t_T$ marks the total duration of the transit, and $t_{23} = t_F$ is the duration of the full transit. The transit center time is marked with t_c, and the transit depth is marked by ΔF.

its velocity. The total transit duration, the time between ingress and egress, $t_{\rm T}$ (Fig. 2.1), is for non-grazing and circular orbits

$$t_{\rm T} = \frac{P_{\rm orb}}{\pi} \arcsin\left(\frac{R_\star}{a}\left(\frac{(1+k)^2 - b^2}{\sin^2 i}\right)^{1/2}\right), \tag{2.3}$$

where a is the semi-major axis, and b is the impact parameter and defined as the projected distance between the planet and star centers during transit center time in units of the stellar radius $R_\star$

$$b = \frac{a\cos i}{R_\star} \tag{2.4}$$

(Seager & Mallen-Ornelas, 2003; Winn, 2010). The time during which the

planet is fully in front of the stellar disk, the full duration, t_{F}, (Fig. 2.1) is

$$t_{\mathrm{F}} = \frac{P_{\mathrm{orb}}}{\pi} \arcsin\left(\frac{R_\star}{a}\left(\frac{(1-k)^2 - b^2}{\sin^2 i}\right)^{1/2}\right) \tag{2.5}$$

(Seager & Mallen-Ornelas, 2003; Winn, 2010).

Transit durations for eccentric orbits are approximated by multiplying Eq. 2.3 and Eq. 2.5 with $\left(\sqrt{1-e^2}\right)(1+e\sin\omega)^{-1}$, where ω is the argument of periastron (Winn, 2010). The shape of a transit is defined as the ratio between the total and full duration, t_{T} and t_{F}, respectively. Physical quantities can be derived from these geometric equations, which, in combination, define the properties of the transit light curve. The shape of the transit light curve is additionally influenced by the limb-darkening, which refers to the decrease in brightness from the center to the edge of the star.

The expressions above can be inverted to give geometrical parameters under the assumption of $R_{\mathrm{p}} \ll R_\star \ll a$ and circular orbits (Seager & Mallen-Ornelas, 2003; Winn, 2010):

$$k = \frac{R_{\mathrm{p}}}{R_\star} \sim \sqrt{\Delta F}, \tag{2.6}$$

$$b^2 = \frac{(1-k)^2 - (t_{\mathrm{F}}/t_{\mathrm{T}})^2 (1+k)^2}{1-(t_{\mathrm{F}}/t_{\mathrm{T}})^2}, \tag{2.7}$$

$$\frac{a}{R_\star} = \frac{2P_{\mathrm{orb}}}{\pi} \frac{k^{1/4}}{\sqrt{t_{\mathrm{T}}^2 - t_{\mathrm{F}}^2}}, \tag{2.8}$$

Besides, the mean stellar density, $\rho_\star$, can be derived from the light curve

using Kepler's third law and assuming that $M_{\rm p} \ll M_\star$

$$\rho_\star + k^3 \rho_{\rm p} = \frac{3\pi}{G {P_{\rm orb}}^2} \left(\frac{a}{R_\star} \right)^3 , \tag{2.9}$$

where $\rho_{\rm p}$ is the planet density (Winn, 2010). Since the value for k^3 is usually very small, it can be ignored. Estimating $\rho_\star$ from the light curve alone is an essential diagnostic for verifying that the transit is produced by a planet. A transit signal from a planet should yield the same values for $\rho_\star$ as spectroscopically or asteroseismology determined (Winn, 2010). If a planetary system is observed via transit and RVs, the planetary surface gravity, $g_{\rm p}$, can be derived (Winn, 2010)

$$g_{\rm p} = \frac{2\pi}{P_{\rm orb}} \frac{K}{\sin i} \left(\frac{a}{R_{\rm p}} \right)^2 . \tag{2.10}$$

The transit technique is most sensitive to short-period planets with large radii orbiting around small stars. The sensitivity decreases as a function of increasing star-planet distance. In addition, due to the small geometric probability for a transit, a large number of stars must be monitored for each discovery.

False detections, also called false positives, are also a problem for transit surveys. Several astrophysical phenomena can mimic planetary transits, e.g. blends or background eclipsing binaries. Thus, the planet candidates found by the transit method need to be confirmed by other methods. The most secure confirmation method so far is the determination of the transiting object's mass using RV measurements. Complementary methods for the characterization are needed, but it is unlikely that a single method will be able to characterize all planets sufficiently well. Instead, the char-

acterization of planet candidates will likely be based on the combination of many different methods, such as gravitational microlensing (Batista, 2018), direct imaging (Pueyo, 2018), stellar pulsation (Hermes, 2018), radio observations (Lazio, 2018; Griessmeier, 2018), direct spectroscopic observations (Birkby, 2018), secondary eclipses (Alonso, 2018), and astrometry (Malbet & Sozzetti, 2018).

Multi-planet systems The extrasolar planetary systems discovered to date are diverse and show a wide range of evolutionary states (for an overview see Hatzes, 2016a; Winn, 2018; Dawson, 2018). The observed diversity in the planetary architecture led to new planet formation theories: gravitational interactions between planets in the same system excite the orbital eccentricity through planet-planet scattering or secular perturbations; the existence of giant planets on close orbits is explained by disk migration. Hot Jupiters are mainly single planet systems and rarely accompanied by additional close-in planets. These observations agree with the formation of hot Jupiters via eccentricity excitation coupled with tidal circularization, and disagree with the formation via disc migration. Some observations, on the other hand, revealed that hot Jupiters can be accompanied by long-period companions (e.g. Knutson et al., 2014).

Indeed, more than one-third of the planets discovered by the *Kepler* mission belongs to transiting multi-planet systems (Batalha et al., 2013). These systems contain often more than two small planets ($1\,R_\oplus < R_\mathrm{p} < 4\,R_\oplus$), forming compact planetary systems ($P_\mathbf{orb} < 100$ days) with nearly co-planar orbits (Lissauer et al., 2011; Fabrycky et al., 2014), and have low eccentricities. Transiting multi-planet systems constrain the mutual inclination of exoplanetary orbits. One possible mechanism for the formation of these sub-Neptune-sized planets is, in contrast to the for-

mation of giants planets, the in situ formation since they consist mostly of silicates, ice or water. After a planet has formed in situ, it can perturb the disk with the result that additional planets can form or be trapped in resonances. Dynamical interaction can lead to wider orbital separation afterwards, and to a break of the resonant configurations (Ford, 2014). Another mechanism for the formation of compact planetary systems is the formation at larger distances followed by a migration to their current configuration.

Orbital resonance between a planet pair occurs when the mean motion of each planet, n_1 and n_2, is nearly commensurate, that is, the ratio n_1/n_2 is close to small integers, $p : q$, where $p \neq 0$ and $q > 0$. Most of the planets in compact systems are not trapped in MMR (Fabrycky et al., 2014), but have period ratios slightly above the perfect integer ratios for first-order resonance, especially the 2:1 and 3:2 (Delisle & Laskar, 2014). The configuration in mean-motion resonance is an outcome of slow convergent orbital migration within the protoplanetary disk. Further dissipative damping will cause divergent migration whereby the orbits will leave the resonant configuration and produce orbit ratios slightly above the resonant values (e.g. Pichierri et al., 2019). The excess of systems found by *Kepler* not being trapped in mean-motion resonances contradicts with the architecture of the Solar System and with the detection made by RV surveys. Resonant systems exist in the Solar System. The most prominent examples are the resonant 4:2:1 chain also called Laplace resonance of Jupiter's moons Ganymede, Europa, and the 2:3 resonance between Pluto and Neptune. Other examples are Saturns moons Dione and Enceladus in a 2:1 resonance. Orbital resonances are of particular interest and shed light into the planetary evolution and formation (for an overview see Correia et al., 2018). They occur as a result of long-term non-vanishing periodical grav-

itational interactions between the planets. On one hand, orbital resonance can destabilize the system through momentum exchange between planets, whereupon the planets can leave the system or change their orbits. On the other hand, resonant interaction can stabilize the orbits and be self-adjusting, so that the planets stay in their configuration.

Planetary systems containing a low-mass planet and a high-mass outer planet on a wider orbit exist (e.g. Uehara et al., 2016; Foreman-Mackey et al., 2016), and a few of them have been characterized (e.g. Kepler-65, Kepler-25, Kepler-68 (Mills et al., 2019), Kepler-11 and Kepler-90 (Jontof-Hutter et al., 2017; Contreras & Boley, 2018), WASP-47 (Becker et al., 2015; Dai et al., 2015; Neveu-VanMalle et al., 2016; Almenara et al., 2016; Sinukoff et al., 2017b; Weiss et al., 2017). These systems are particularly interesting because they resemble the Solar System, with smaller inner planets and larger outer planets. These systems are more suitable to be habitable because a massive outer planet protects the inner system from asteroid impacts gravitationally, and it is important to know how common such systems are. Low-mass planets in systems that do not have massive outer planets are in danger of being hit by asteroids and comets from Kuiper belt-like regions.

Another advantage of transiting multi-planet systems is that the planetary masses can be estimated through their mutual gravitational interactions that affect the times the planets transit in front of their star. This has led to a new technique for characterizing a multi-planet system: Transit Timing Variation. TTVs can constrain the planetary masses and orbits. Especially, they can be used to characterize the masses and eccentricities for small planets that cannot be measured easily with RVs. Therefore, TTVs are a powerful tool to characterize planetary systems even with low-mass planets, and to constrain their evolution and formation.

3

Transit Variations

Transit Timing Variations (TTV), Transit Duration Variations (TDV), and Transit dePth Variations (TPV) are indirect tools for characterizing exoplanet systems. These variations are caused by perturbations of the Keplerian motion of the planet, and can be measured from transit light curves. The variations can be detected if their effect is strong enough, the transit S/N is high enough, and the time span of observations is sufficiently long. Different effects can cause these perturbations. Non-Keplerian interaction can be caused by external potentials, e.g., the centrifugal potential of a rotating body and the tidal potential. Together with general relativistic effects, all perturbations cause orbital precession (Miralda-Escude, 2002; Heyl & Gladman, 2007; Pál & Kocsis, 2008; Jordan & Bakos, 2008; Ragozzine & Wolf, 2009; Damiani & Lanza, 2011; Csizmadia et al., 2019). The orbital precession consists of two components.

Nodal precession The rotation of the orbit around the stellar angular momentum is known as the precession of the line of nodes. Nodal precession occurs when the orbital plane is not aligned with the stellar equator. In the case of equatorial and polar orbits, the torque

exerted by the star is zero and the nodal precession vanishes (see Sec. 3.2, and Iorio (2011b) and Ragozzine & Wolf (2009)).

Periastron precession The rotation of an eccentric orbit within the plane of the orbit is known as the precession of the periastron, where the periastron is the point in the orbit with the minimal distance to the star (Ragozzine & Wolf, 2009).

Gravitational interactions, stellar quadrupole moment, and tidal distortions can all cause nodal and periastron precession (Miralda-Escude, 2002; Heyl & Gladman, 2007; Iorio, 2011a; Jordan & Bakos, 2008; Damiani & Lanza, 2011). Additionally, General Relativity (GR) induces periastron precession (Heyl & Gladman, 2007; Pál & Kocsis, 2008; Iorio, 2011a; Jordan & Bakos, 2008).[1] The nodal precession causes variations in the transit durations and depths, while the periastron precession causes variations in the transit durations and times. TTVs are the most commonly observed effects out of the three, since the variations in the transit times are relatively easy to measure with high precision (Ragozzine & Wolf, 2009; Ragozzine & Holman, 2010).

In addition to these precessions, orbital decay of close-in massive planets causes transit timing variations on longer time scales (decades), and helps to improve the knowledge of the evolution of planetary systems and the stellar interiors (e.g. Ragozzine & Wolf, 2009; Birkby et al., 2014).

Each perturbation acts on its own time scale with a particular shape and strength. Which perturbation dominates the system depends on the planetary configuration. Planets in multi-planet systems exhibit non-Keplerian orbits

[1] The argument of periastron can also be changed by magnetic interaction between the star and the planet, but this effect is not considered here.

mostly as a result of the gravitational interactions with other objects in the system. The gravitational interactions act on the shortest time-scale compared to the long-term perturbations while exerting the strongest variations. The physical quantities of the planets perturbing a transiting planet can be inferred through the inversion of the TTV signal. This inversion can be done using analytical or numerical methods. The TTV method has mainly been used for measuring the masses and eccentricities of small transiting planets near mean-motion resonance (e.g Hadden & Lithwick, 2014, 2016, 2017; Jontof-Hutter et al., 2016), whereas the mass measurements have not been possible with RVs.

The idea of extracting information from the transit variations originates from the studies of the eclipsing binary interiors via the apsidal motion (e.g. Sterne, 1939; Shakura & I., 1985). The basic concept is that the orbit precesses due to the non-point mass component of the gravitational field changing the timing of the primary and secondary eclipses (Sterne, 1939). The deviations in the timing allow the determination of the apsidal motion constant k_2. Ragozzine & Wolf (2009) transferred this idea to exoplanet systems in order to measure the interiors of hot Jupiters. They discovered that the TDVs are more essential than TTVs for deriving $k_{2,\mathrm{p}}$ accurately, and their result was later corroborated by Csizmadia et al. (2019).

Transit depth variations are due to changes in the planet's projected path across the stellar disk. Transit depth variations are harder to detect than TDVs and TTVs. They can be caused by the spin precession of an oblate planet and help to measure its oblateness and obliquity (Carter & Winn, 2010; Biersteker & Schlichting, 2017). Changes in the transit geometry caused by nodal precession can also change the impact parameter and therefore the transit depths. However, transit depths are affected by various physical and observational effects, such as seasonal variations, cross-

ing of stellar spots, brightness variations due to non-occulted stellar spots, stellar rotation, disintegrating planets, and contamination differences (e.g. Kipping, 2012; Rappaport et al., 2012; Croll et al., 2015), which mask the orbital effects. Therefore, only transit times and durations are considered in the next section.

3.1. Transit Timing Variations

If a planetary orbit is not subject to perturbations, its orbital period is constant (Fig. 3.1 top panel), and the transit centers are

$$t_{\mathrm{N}} = t_0 + N \times P_{\mathrm{orb}}, \tag{3.1}$$

where t_0 is the time of first transit, N is the transit number also called transit epoch and t_{N} is the transit center for transit number N (Agol & Fabrycky, 2018). If the orbit is perturbed, the transit times are not strictly periodic and vary around the mean orbital period (blue line in Fig. 3.1 lower panel). These variations around the mean orbital period (green line in Fig. 3.1) are called transit timing variations. The variations follow a sine where the period of the sine is called the TTV period (P_{TTV})[2], which is the time it takes for the planets to return to their initial configurations. Precise measurements of the transit times can reveal these deviations from a constant period. These deviations are signs for perturbations of the Keplerian motion of a planet, e.g. by gravitational interaction with another planet.

[2]The correct mean orbital period of a planet is known only after a complete TTV cycle and represents the time between two consecutive periastron passages.

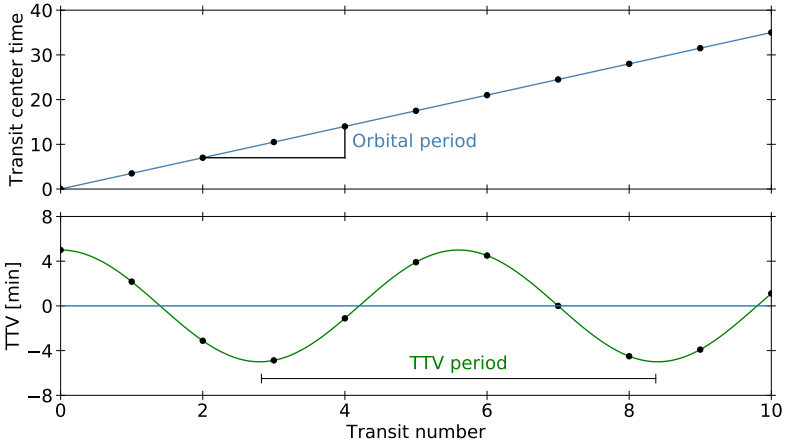

Figure 3.1.: Top panel: transit times assuming a constant period. The black triangle marks the slope of the blue line (orbital period). Lower panel: transit times subtracted by a mean orbital period (green line) when the orbit is perturbed by external forces. The blue line correspond the constant period. The transits occur earlier or later compared to the mean orbital period with a period of P_{TTV}.

Gravitational Interaction The TTV period depends, i.a., on the proximity of the planetary orbital periods to a period commensurability. If the orbital periods are close to a period commensurability, it is likely that the perturbing planets are in a mean-motion resonance. The periodicity of the TTVs for planets near first order resonances depends on its actual separation from the exact resonance value (Agol et al., 2005; Lithwick et al., 2012)

$$P_{\mathrm{TTV}} = \frac{1}{\frac{p}{P_2} - \frac{q}{P_1}}, \tag{3.2}$$

where p and q are small integers indicating the first order resonances. The closer the period ratio is to the exact period commensurability, the

longer the TTV period. For planets exactly in resonance, the longitude of conjunctions occurs always at the same orbital position with a period of $P_{\rm TTV}$. The perturbations between planets are strongest during orbital conjunctions, changing the semi-major axes and orbital periods, and therefore leading to variations in transit times. Other effects causing the transit timing variations are discussed in the following.

3.1.1. Orbital precession

In the presence of orbital precession, the transit times are calculated up to first-order in eccentricity as:

$$t_{\rm N} \approx t_0 + N \times P_a \left(1 - \frac{\dot{\omega}}{n}\right) + \frac{\vartheta_{\rm n} P_a}{2\pi} - \frac{e P_a}{\pi} \cos\left(\omega_0 + \dot{\omega}\left(t_{\rm N} - t_0\right)\right), \tag{3.3}$$

where P_a is the anomalistic period, the time between two successive periastrons, (Csizmadia et al., 2019). The correction factor ϑ accounts for mid-transit times occurring at the minimal sky-projected distances instead of at conjunctions (e.g. Csizmadia et al., 2019):

$$\tan\vartheta = -\frac{e\cos\omega\cos^2 i}{e\sin\omega + \sin^2 i\cos\vartheta}. \tag{3.4}$$

The precession can be caused, in addition to gravitational interaction, by the following effects.

General Relativity leads to periastron precession rates of

$$\dot{\omega}_{\rm GR} = \frac{3GM_\star}{ac^2\left(1-e^2\right)} n \tag{3.5}$$

in radians per second (Perryman, 2018, p. 259), where c is the speed of light. This rate arises from the relativistic effects caused by the host star's mass. Mercury is undergoing periastron precession where its perihelion advances with a rate of 0.42 arcsec year^{-1} faster than predicted by the perturbations from all other planets (Le Verrier, 1859). This advance is explained by GR in Einstein (1916). In the context of exoplanets, Heyl & Gladman (2007) mentioned that the relativistic effects are not negligible for close-in hot Jupiters and could be measurable within an observation time span of ten years.

Tidal interaction and rotation can significantly influence the planets orbiting close to their host star. The tidal force is inversely proportional to the cube of the distance between the bodies, and proportional to the mass of the tide-rising body. Tidal forces cause several effects (e.g. Matsumura et al., 2010): tidal or orbital decay, orbit circularization, orbit synchronization, and orbital precession. The former effects are due to a decrease in the semi-major axis, the eccentricity, and the rotation period. The latter effect is caused by the deformation of the planet provoked by the adjustment of the mass distribution inside a planet (see previous section). The time-scale of each effect is different; the orbit precession acts on the shortest time scale (10-1000 years). The other effects have even longer time scales, and are therefore more difficult to detect.

Tidal interactions and rotational bulges lead to precession rates under

the assumption of zero obliquity (Sterne, 1939)

$$\begin{aligned}\dot{\omega}_{\rm tide,rot} = &\frac{nk_{2,\star}}{2}\left(\frac{R_\star}{a}\right)^5\left(\frac{15M_{\rm p}\widetilde{g}\,(e)}{M_\star}+\frac{P_{\rm rot,\star}^2 a^3\widetilde{f}\,(e)}{GM_\star}\right)\\ &+\frac{nk_{2,p}}{2}\left(\frac{R_p}{a}\right)^5\left(\frac{15M_\star\widetilde{g}\,(e)}{M_p}+\frac{P_{\rm rot,p}^2 a^3\widetilde{f}\,(e)}{GM_p}\right),\end{aligned} \tag{3.6}$$

with $\widetilde{g}\,(e) = \left(1-e^2\right)^{-5}\left(1+3/2e^2+1/8e^4\right)$ and $\widetilde{f}\,(e) = \left(1-e^2\right)^{-2}$ and $P_{\rm rot}$ the rotation period. The first terms in the brackets of Eq. 3.6 are the precession rates including the planetary and stellar tidal bulges, and the second terms are the rates due to rotational bulges of the planet and the star. The precession depends linearly on the stellar and planetary Love numbers, $k_{2,\star}$ and $k_{2,\rm p}$, respectively, that are twice the apsidal motion constant k_2. Besides these two quantities, all other quantities can be determined spectroscopically and photometrically. Therefore, the detection of precession enables the determination of the internal structure possible. In the hydrostatic equilibrium, the internal density distribution is characterized by the Love number (Love, 1911; Kramm et al., 2011). Ragozzine & Wolf (2009) derived from an approximated relation for stellar quadrupole moment, J_2, under the assumption of zero obliquity that considers the Love number

$$\begin{aligned}J_2 &= \frac{k_2}{3}\left(q_{\rm r}-\frac{q_{\rm t}}{2}\right),\\ q_{\rm r} &= \frac{P_{\rm rot,p}^2 R_{\rm p}^3}{GM_{\rm p}},\\ q_{\rm t} &= -3\frac{M_\star}{M_{\rm p}}\left(\frac{R_{\rm p}}{r}\right)^2.\end{aligned} \tag{3.7}$$

The stellar rotational terms agree with the equation derived in Heyl & Gladman (2007) if Eq. 3.7 is taken into account. In general, the factor determining the oblateness is defined via the equatorial radius $R_{\rm eq}$ and the polar radius $R_{\rm pol}$ via $f = (R_{\rm eq} - R_{\rm pol})/R_{\rm eq}$. The oblateness factor f for rotationally induced oblateness is approximately (Murray & Dermott, 1999):

$$f = \frac{3}{2} J_2 + \frac{1}{2} \frac{R_{\rm eq}^3}{G M_{\rm p}} \left(\frac{2\pi}{P_{\rm rot}} \right)^2 . \tag{3.8}$$

The periastron precession occurs only if the planetary orbit is non-circular. However, tidal interactions tend to circularize the planetary orbit in relatively short timescales. This means that other mechanisms excite the eccentricity, e.g. gravitational interaction with a nearby low-mass planet. Moreover, if more than one massive planet orbits the host star, tidal interaction between the planets can also excite the eccentricity. Tidal forces acting on planets in multi-planet systems near or in MMR can lead to changes in the period that displaces the planets from their resonances on the long-term time scale (Papaloizou, 2011; Lee et al., 2013). Furthermore, if an inner planet is accompanied by a more massive planet on a wider orbit and both planets are in the same plane, the tides of the outer companion increase the orbital period of the inner planet while decreasing its rotation. In contrast, when the massive planet is out of the plane of the inner planet, its tides decrease the orbital period of the inner planet while increasing its rotation period. The inner orbit exhibits periodical variations with the period of the outer companion (e.g. Borkovits et al., 2003; Agol et al., 2005; Dawson et al., 2014).

Whether a planet experiences significant tidal interaction with its host star can be calculated via the following parameters (Korth et al., 2019):

The Doodson constant, $D_{\rm p}$, defines the magnitude of the tidal forces exerted by the planet to the star (Pätzold et al., 2004)

$$D_{\rm p} = \frac{3GM_{\rm p}R_\star^2}{4a^3}. \tag{3.9}$$

The stellar property factor, $F_\star$, defines the magnitude of orbital decay (Pätzold & Rauer, 2002)

$$F_\star = \frac{M_{\rm p}R_\star^5}{\sqrt{M_\star}}. \tag{3.10}$$

The synchronous orbit defines the orbit of a planet undergoing orbital decay, where the semi-major axis is

$$a_{\rm sync} = \left(\frac{G\left(M_\star + M_{\rm p}\right)}{P_{{\rm rot},\star}^2}\right)^{\frac{1}{3}}. \tag{3.11}$$

3.1.2. Orbital decay

Close-in planets that are not in tidal equilibrium are expected to spiral towards their host stars as a result of tidal dissipation (Levrard et al., 2009).

Orbital decay means that due to tides raised by a close-in planet, the tidal bulge of the star exerts a torque on the planet that transfers energy and angular momentum to the star (Zahn, 1977; Hut, 1981; Eggleton et al., 1998).

As long as there is only one planet orbiting a star, tidal interaction results in orbit circularization. In the solar system, the opposite mechanism leads to an increasing orbital period of the Moon, since the orbital period is longer than the Earth's rotational period.

The rate of decay of the semi-major axis under the assumption of circular orbit and zero stellar obliquity is (Murray & Dermott, 1999)

$$\dot{a} = sign\left(P_{\mathrm{rot},\star} - n\right) \frac{3k_{2,\star}}{Q_\star} \frac{M_\mathrm{p}}{M_\star} \left(\frac{R_\star}{a}\right)^5 na, \tag{3.12}$$

where $Q_\star$ is the tidal dissipation factor. Assuming a circular orbit and a constant change in the orbital period, orbital decay leads to changes in the transit times of (Ragozzine & Wolf, 2009; Birkby et al., 2014)

$$t_\mathrm{N} = t_0 + N \times P_\mathrm{orb} + \frac{1}{2} N^2 \frac{P_\mathrm{orb}}{2\pi} \dot{n}. \tag{3.13}$$

The orbital decay translates into changes in the transit times via the change in the orbital angular frequency. Under the assumption of zero stellar obliquity, negligible tidal dissipation, circularized orbits, and synchronized stellar spin (see Birkby et al., 2014)

$$\dot{n} = -\frac{27}{4} n^2 \frac{M_p}{M_\star} \left(\frac{R_\star}{a}\right)^5 \frac{1}{Q'_\star}, \tag{3.14}$$

where $Q'_\star$ is the tidal quality factor defined in Dobbs-Dixon et al. (2004) as of $Q'_\star = 3Q_\star/2k_{2,\star}$. Furthermore, assuming the constant time lag model, where Δt denoted the time lag, the dissipation factor is given by $Q_\star = 1 / \Delta t$. The tidal quality factor depends on the properties of the star (mass, structure, and rotation rate) and measures the strength of tidal dissipation where higher values mean weaker tidal dissipation.

Unfortunately, the tidal quality factor is not well constrained by observations. Meibom & Mathieu (2005) determined $Q'_\star \approx 10^6$ for binary stars and Jackson et al. (2008) estimated a range between $10^6 < Q'_\star < 10^9$. Bonomo et al. (2017) studied a sample of hot planets and found a range be-

tween $10^6 < Q'_\star < 10^7$. In the Solar System rocky planets and large rocky moons have values for $Q'_\star$ between 10 and 500, while gas-giant planets have values of $10^5 < Q'_\star < 10^6$ (Goldreich & Soter, 1966; Peale, 1999). The exact value for $Q'_\star$ for a particular star is uncertain and there is no way to measure it directly except via orbital decay. Therefore, measurements of $Q'_\star$ through a detection of orbital decay via TTVs is highly beneficial (Watson & Marsh, 2010; Birkby et al., 2014; Valsecchi & Rasio, 2014). Essick & Weinberg (2015) calculated the detectability of tidally induced TTVs and suggested that orbital decay could explain the observed lack of massive ultra-short period (USP) planets and could generate detectable TTVs in the near future.

3.1.3. Time scales

Each effect acts on its own time scale with a specific shape. TTVs produced by an additional planet that is relatively close or in resonance with the transiting planet can be easily distinguished from the TTVs induced by long-term perturbations. The TTVs produced by planets near resonance show a sinusoidal shape with a large amplitude on a time scale of days (see Fig. 3.1) while the TTVs produced by the periastron precession act on a much longer time scale (10-1000 years). The TTVs caused by orbital decay show in contrast a parabolic trend (see Eq. 3.13). However, perturbations induced by an outer companion or a body not close to resonances can lead to similar TTVs as produced by the planetary tidal bulges (e.g Miralda-Escude, 2002; Heyl & Gladman, 2007; Jordan & Bakos, 2008). Therefore, it is essential to know the contributions to the periastron precession from GR, non-sphericity, and tidal interaction.

The contributions to the periastron precession are shown in Fig. 3.2 for

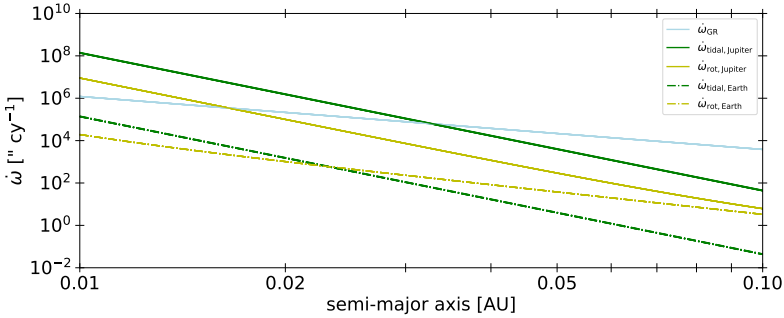

Figure 3.2.: Precession of the periastron for the particular contributions by a Sun-like star, a Jupiter-like (solid lines), and Earth-like planet (dashed lines) in arcsecond per century. The precession of a hot Jupiter caused by tidal interaction (green solid line) dominates over the contribution from general relativity (light blue solid line) for orbits within 0.04 AU. The precession caused by the rotational bulge of the planet (yellow solid line) dominates over the contribution from general relativity for even closer orbit (<0.02 AU). The precession rates of Earth-like planets are magnitudes smaller than the precession of hot Jupiters.

a solar-like star, a Jupiter-like planet, and an Earth-like planet. Since the amplitudes of each effect depend on several parameters, the significance of each effect might be different. All these effects and the orbital decay depend on the semi-major axis and are stronger close to the star. Therefore, the contributions are calculated for close-in planets between 0.01 and 0.1 AU on slightly eccentric orbits (e=0.01)[3]. The planetary and stellar parameters are summarized in Table 3.1.

The precession caused by tidal interactions has the strongest influence in close proximity to the star followed by the relativistic precession and the precession caused by non-sphericity. The precession rates for Jupiter-like planets are magnitudes higher than the rates for Earth-like planets.

[3]Higher eccentricity does not change the qualitative trend of the individual precession rates.

Table 3.1.: Reference values for the stellar and planetary parameters under the assumption of synchronous orbits ($P_{\rm rot} = n$). Masses, radii, and the gravitational constant G (6.67408×10^{-11} m^3 kg^{-1} s^{-2}) are taken from astropy.units (Robitaille et al., 2013; Price-Whelan et al., 2018). Further, the stellar and planetary equators are aligned with the orbital plane ($\Psi_\star = \psi_{\rm p} = 0$), $i = 90°$ and $\omega = 90°$.

Parameter	Star	Jupiter-like planet	Earth-like planet
Mass [kg]	1.9884754×10^{30}	1.8981872×10^{27}	5.9723647×10^{24}
Radius [m]	6.957×10^{8}	7.1492×10^{7}	6.3781×10^{6}
$P_{\rm rot}$ [rad/s]	2.9×10^{-6}	n	n
k_2	0.035[a]	0.53[b]	0.29[c]

Taken from [a] Ogilvie (2014), [b] Ni (2018) and [c] Kozai (1968).

Since the tidal and rotational induced precessions have planetary and stellar contributions, these precession rates are separately considered in more detail in Fig. 3.3. The planetary contributions to the tidal and rotational precession (dash-dotted line in Fig. 3.3) dominate over the stellar contribution (solid line in Fig. 3.3). This is in good agreement with the findings by Ragozzine & Wolf (2009). They found that the planet's tidal contribution to the periastron precession is about 100 times larger than the star's tidal contribution. The mass ratio is the dominant quantity in this context, and stars are more massive than planets. The rotational contribution varies depending on the rotation and spins rates of the planet and the star. Ragozzine & Wolf (2009) estimated that for synchronized orbits of the star and the planet, both contributions are comparable, while for all other states the tidal bulge of the planet is more essential.

The shift in the transit times caused by orbital decay for a solar-like star and a Jupiter-like planet assuming $Q'_\star = 10^6$ is shown in Fig. 3.4. Orbital decay occurs on various time scales (e.g. decades; Birkby et al., 2014).

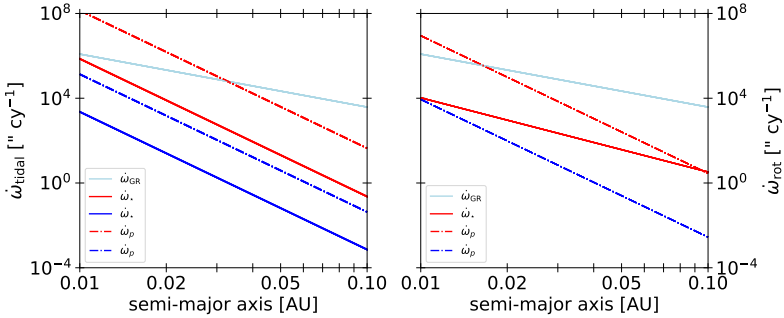

Figure 3.3.: Tidal (left) and rotational (right) contributions to the precession of the periastron for a Sun-like star, a Jupiter-like (red lines), and Earth-like planet (blue lines). The stellar (solid lines) and planetary (dashed-dotted lines) contributions are visualized separately. The planetary contributions dominate the precession rates induced by both the tidal and rotational bulges. For a direct comparison, the relativistic precession rate is plotted in light blue.

Compared to the other TTV contributions, orbital decay has the smallest amplitude and affects very close-in planets. Therefore, the expected transit shifts for some USP planets and hot Jupiters are shown also. A shift in the transit times after ten years is considered because the combination of *Kepler* and *TESS* data enables the search for variations on this time scale.

3.1.4. Application

TTVs can reveal the existence of additional objects in the planetary system: small objects (Agol et al., 2005) preferably in a compact orbital configuration (e.g. WASP-47; Becker et al., 2015; Dai et al., 2015; Neveu-VanMalle et al., 2016; Almenara et al., 2016; Sinukoff et al., 2017b; Weiss et al., 2017), non-transiting objects (e.g. Kepler-19; Ballard et al., 2011; Malavolta et al., 2017), co-orbital objects (Ford & Holman, 2007; Leleu

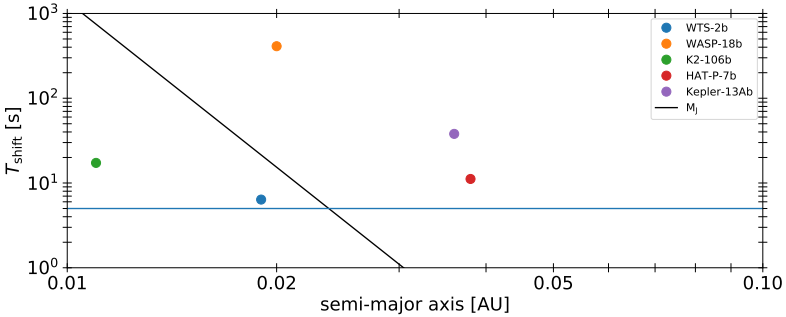

Figure 3.4.: Transit shifts after 10 years for a solar-like star and a Jupiter-like planet (black line) caused by orbital decay assuming $Q'_\star = 10^6$. The transit shifts for some USP planets and hot Jupiters that are discussed in subsequent sections (Sect. 4.3 and Sect. 4.4) are shown as colored circles; WTS-2b is also shown for comparison. The blue line marks the 5 second precision limit that is achievable for *Kepler* short cadence light curves for hot Jupiters (e.g. Kepler-13Ab), see also Doyle & Deeg (2004).

et al., 2019) or at least they can place limits on their existence (Steffen & Agol, 2005; Csizmadia et al., 2010). The application of TTVs to detect exomoons was suggested and presented by Sartoretti & Schneider (1999), Szabó et al. (2006), Simon et al. (2007), and Kipping (2009a,b). The non-detection of interactions give hints that the hypothetical planets have either low masses, small eccentricities, or are on wide orbits. The successful application of the TTV method became only feasible since the start of the *Kepler* mission (e.g. Xie, 2013, 2014; Hadden & Lithwick, 2014; Jontof-Hutter et al., 2016; Hadden & Lithwick, 2016, 2017). Before *Kepler* was launched, some ground-based studies carried out searches for TTVs in systems mainly consisting of hot Jupiters (e.g. Pál, 2012; Nascimbeni et al., 2011; Fulton et al., 2011; Maciejewski et al., 2010; Montalto et al., 2012; Nascimbeni et al., 2013; Gibson et al., 2008, 2009; Steffen

& Agol, 2005; Fukui et al., 2011; Maciejewski et al., 2011; Miller-Ricci et al., 2008; Bean, 2009; Ballard et al., 2010; Adams et al., 2010, 2011a,b). These studies were limited by the observation precision and could mostly only exclude some scenarios for hypothetical planets. Merely, with the launch of *Kepler*, it became possible to detect small variations in the transit times, starting the era of TTV science. Since then, TTVs have been used to detect, confirm, and characterize transiting and non-transiting planets, demonstrating the high potential of this method.

The detection of additional (non)-transiting planets was the first application of the TTV method. In systems where only one planet exhibiting TTVs has been detected in transit, the TTVs can be used to discover additional planetary or sub-stellar objects. Kepler-19 was the first system where an additional non-transiting planet was detected via TTVs (Ballard et al., 2011). These detected objects can be further analyzed by their TTV signal.

The confirmation of planetary candidates is the major application of the TTV method. The method was widely applied to confirm candidates in multi-planet systems detected by *Kepler*. The *Kepler* mission detected thousands of planet candidates that needed further follow-up observations to verify them as planets or unveil them as, e.g., blends or background eclipsing binaries. The limited follow-up resources triggered the development of new methods to confirm planet candidates. One of those new approaches was the TTV method. Two planet candidates forming a potential multi-planet system are confirmed as planets if they exhibit anti-correlated TTVs verifying that they interact dynamically and orbit the same star.

The characterization of exoplanets is the most critical and computationally challenging application of the TTV method. Since the TTVs are caused mainly by the gravitational interaction between the objects, the physical quantities can be determined by inverting the TTV signal. The amplitude and periodicity of the TTVs depend on the physical quantities (e.g. mass) of the perturbing planets and the orbital architecture of the system (e.g. Holman & Murray, 2005; Agol et al., 2005; Veras et al., 2011). Amplitudes and periods of the TTVs can be revealed if sufficient transits are observed. Therefore, the TTV method offers a way to measure the masses of planets and complements the RV method. The TTV amplitude is enhanced when the planets are in or near mean-motion resonances (Agol et al., 2005; Holman & Murray, 2005; Agol & Steffen, 2007; Lithwick et al., 2012; Nesvorný & Vokrouhlický, 2016; Hadden & Lithwick, 2016). This feature makes this approach an ideal method for the characterization of low-mass planets that are not easy to observe with RV. Unfortunately, the characterization of non-transiting planets via TTVs is particularly challenging because of ambiguities in the orbital periods. For the general case of N interacting planets that are not in resonances, Agol & Fabrycky (2018) give an expression for the TTVs

$$\mathrm{TTV}_k = P_{\mathrm{orb},k} \sum_{j \neq k} \frac{M_{\mathrm{p}j}}{M_\star} F_{kj}\left(\alpha_{kj}, \theta_{kj}\right) \qquad \text{for } k = 1, ..., N, \quad (3.15)$$

where M_p and $M_\star$ are the planetary and stellar masses. The perturbations F are functions of the semi-major axis ratios with $\alpha_{kj} = \min\left(\alpha_k/\alpha_j, \alpha_j/\alpha_k\right)$ and the orbital elements for each planet $(\theta_{kj} = \nu_k, e_k, \omega_k, i_k, \Omega_k, \nu_j, e_j, \omega_j, i_j, \Omega_j)$. These functions can be solved analytically or numerically via the perturbation theory (e.g. Nesvorný &

Morbidelli, 2008; Agol & Deck, 2016; Deck & Agol, 2016). An analytical approach is only feasible if the problem is simplified and reduced typically to first or second order in the orbital elements. Some analytical expressions have been derived for the case of two transiting perturbing planets (Agol et al., 2005; Linial et al., 2018), close to first-order resonances (Agol et al., 2005; Lithwick et al., 2012; Hadden & Lithwick, 2014; Nesvorný et al., 2014; Nesvorný & Vokrouhlický, 2016; Hadden & Lithwick, 2016; Agol & Deck, 2016), or second-order resonances (Hadden & Lithwick, 2016; Deck & Agol, 2016). Some numerical approaches based on n-body integration can be found by Borsato et al. (2014), Deck et al. (2014), and Hadden & Lithwick (2016, 2017). Since mutual inclinations are not strongly influencing the TTV amplitudes, most studies assume coplanarity (e.g. Lithwick et al., 2012; Nesvorný et al., 2014; Jontof-Hutter et al., 2016; Hadden & Lithwick, 2016; Agol & Deck, 2016).

In addition to the estimation of the orbital elements and masses, TTVs observed over a long time span can help to constrain the internal structure via measurements of the planetary Love number (Ragozzine & Wolf, 2009; Patra et al., 2017; Csizmadia et al., 2019), and to constrain the tidal dissipation factor (e.g. Birkby et al., 2014; Maciejewski et al., 2018; Petrucci et al., 2018; Zhao et al., 2018; Bouma et al., 2019). An example of a planet undergoing an orbital decay that could lead to measurable variations in the transit times is WTS-2b (Birkby et al., 2014). After 15 years the transit times could be shifted around 17 seconds assuming a $Q'_\star = 10^{-6}$. These authors note that a smaller change in the transit times would constrain the lower limit of the tidal dissipation factor.

3.2. Transit Duration Variations

Not only the transit times are perturbed by external forces, but also the transit durations. Transit duration variations are variations in the transit chord length, meaning changes in the time that it takes for the planet to fully transit the star. Nodal precession changes the impact parameter (orbital inclination) of the transit, which leads to variations in the transit chord length (Eq. 2.3), and therefore in the transit duration. Miralda-Escude (2002) and Iorio (2011b,a) calculated the effect on the transit duration for a circular orbit due to the nodal precession caused by the stellar quadrupole moment and a second planet. A more general derivation of the transit duration variation including nodal and apsidal precession is presented in Damiani & Lanza (2011)

$$\dot{t}_{\mathrm{d}} = \frac{2}{v_{\tan}\sqrt{{R_\star}^2 - b'^2}} \left(b'^2 \tan i \left\langle \frac{di}{dt} \right\rangle + \left(2b'^2 - {R_\star}^2\right) \frac{e\cos\omega}{1+e\sin\omega} \left\langle \frac{d\omega}{dt} \right\rangle \right), \tag{3.16}$$

with the tangential velocity $v_{\tan} = (a\,n + a\,n\,e\sin\omega)/(\sqrt{1-e^2})$ and the impact parameter $b' = (a(1-e^2)\cos i)/(1+e\sin\omega)$. The first and second term denote the nodal and periastron precession, respectively. This expression is valid for arbitrary obliquities. The equation for the orbital elements averaged over an orbit are

$$\begin{aligned}
\left\langle \frac{di}{dt} \right\rangle &= -\frac{k_{2,\mathrm{p}}\widetilde{f}\,(e)}{2n} \left(1 + \frac{M_{\mathrm{p}}}{M_\star}\right) \left(\frac{R_\star}{a}\right)^5 P_{\mathrm{rot},\star}^2 \cos\psi \sin i_\star \sin\lambda, \\
\left\langle \frac{d\omega}{dt} \right\rangle &= \frac{k_{2,\star}\widetilde{f}\,(e)}{2n} \left(1 + \frac{M_{\mathrm{p}}}{M_\star}\right) \left(\frac{R_\star}{a}\right)^5 \left(\frac{P_{\mathrm{rot},\star}}{2} \left(3\cos\psi - 1\right) + \frac{15GM_{\mathrm{p}}\widetilde{g}\,(e)}{a^3} \right) \\
&\quad + \frac{k_{2,\mathrm{p}}\widetilde{f}\,(e)}{2n} \left(1 + \frac{M_\star}{M_{\mathrm{p}}}\right) \left(\frac{R_{\mathrm{p}}}{a}\right)^5 \left(n^2 + \frac{15GM_\star\widetilde{g}\,(e)}{a^3} \right) \\
&\quad + \frac{3a^2n^3}{c^2\left(1-e^2\right)} - \left\langle \frac{d\Omega}{dt} \right\rangle \cos i,
\end{aligned} \tag{3.17}$$

$$\left\langle \frac{d\Omega}{dt} \right\rangle = -\frac{k_{2,\mathrm{p}} \widetilde{f}(e)}{2n} \left(1 + \frac{M_\mathrm{p}}{M_\star}\right) \left(\frac{R_\star}{a}\right)^5 P_{\mathrm{rot},\star}^2 \frac{\cos\psi \left(\cos i_\star - \cos i \cos\psi\right)}{\sin i}.$$

In the case of equatorial and polar orbits, the torque exerted by the star on the planet is zero, and the nodal precession vanishes. In contrast, the periastron precession causes TDVs for all obliquities. In the case of zero obliquity, Eqs. 3.17 simplifies to the precession rates given in Eqs. 3.5 and 3.6, and the contributions are the same as in Sect. 3.1.3.

Nodal precession was detected in the WASP-33 system via Doppler tomography by Johnson et al. (2015). They measured that the ascending node changes, leading to transits be observable from Earth from 1970 to 2060. This finding allowed them to set limits on the stellar gravitational quadrupole moment J_2, as suggested by Miralda-Escude (2002).

If TTVs and TDVs are identified for the same planet, they can help to uniquely constrain the masses of the perturbing object even if the planet is not transiting. Examples, where TDVs were detected and used to constrain the physical quantities, are Kepler-88 (Nesvorný et al., 2013), Kepler-108 (Mills & Fabrycky, 2017a), and Kepler-117 (Almenara et al., 2015).

3.3. Challenges

The inversion of the TTV signal is ambiguous Many physically different solutions in the parameter space can lead to TTVs and TDVs that are identical within the observational errors, and some parameters are strongly correlated, e.g., planetary mass and orbital eccentricity (Lithwick et al., 2012; Deck & Agol, 2015). The mass determination by TTVs is complicated by the fact that there is a cross-talk between the planetary masses and orbital eccentricities. The orbital eccentricity may either be derived from

statistics (Lithwick et al., 2012; Wu & Lithwick, 2013), by using a photodynamical model (e.g. Cochran et al., 2011; Huber et al., 2013; Almenara et al., 2016, 2018a; Freudenthal et al., 2018; Mills et al., 2019) or through the combination with RV measurements (e.g. Nespral et al., 2017; Petigura et al., 2018). The ambiguity between planetary mass and orbital eccentricity may also be solved if additional harmonics, the so-called "chopping" signal, are detected in the TTVs (Nesvorný et al., 2013, 2014; Nesvorný & Vokrouhlický, 2014; Deck & Agol, 2015; Agol & Deck, 2016; Linial et al., 2018). The "chopping" signal has a smaller amplitude than the overlying resonant signal and occurs at the planetary conjunctions with the synodic period

$$P_{\mathrm{syn}} = \frac{1}{\frac{1}{P_1} - \frac{1}{P_2}}. \tag{3.18}$$

Another ambiguity occurs when the perturbing planet is not transiting and no further harmonics are detected in the TTVs. In this case, the degrees of freedom are simply too large to determine all physical parameters, and additional constraints are needed to solve the ambiguity. Generally speaking, several orbital configurations can reproduce the observed TTVs that might be indistinguishable and complicate or prevent the inference of the physical quantities if the TTVs do not reveal the full information about all of the planets in the planetary system. Nevertheless, if all planets are transiting, the orbital periods, phases, and sizes can be directly constrained.

Puffy planets Comparing the masses of planets determined by RVs and TTVs reveals a systematic discrepancy (Fig. 3.5). TTV mass estimates are systematically smaller than RV mass estimates, and therefore the densities derived from TTVs are also lower compared to the bulk densities in the solar system, leading to the so-called 'puffy' planets (Lissauer et al.,

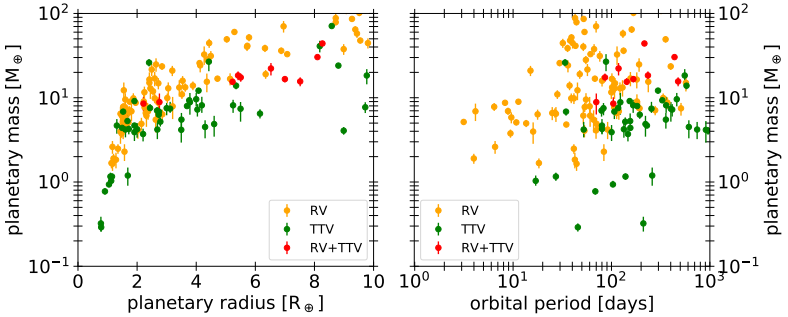

Figure 3.5.: Mass-radius (left) and mass-period (right) diagram for mass determinations better to 30% from RVs (yellow), TTVs (green), and a combination of both methods (red). The data are taken from the TEPCat catalog(Southworth, 2011) and have been checked and updated with literature values.

2011, 2013; Wu & Lithwick, 2013; Masuda, 2014; Ofir et al., 2014; Hadden & Lithwick, 2014; Weiss & Marcy, 2014; Jontof-Hutter et al., 2014, 2015, 2016). Examples for 'puffy' planets are Kepler-51b, Kepler-79d, and Kepler-87c; examples for massive low-density planets are Kepler-18d, K2-24c, and Kepler-177c. Both methods, TTV and RV, have been combined only for a very small sample of planets, and the mass values lie at the border between the two regimes (Fig. 3.5).[4] For some planets, masses derived by both methods agree with each other.[5] The disagreement between the masses calculated by RVs and TTVs leads to the suspicion that the TTV estimates are biased. Weiss & Marcy (2014) and Steffen (2016) suggest that undetected planets may damp the TTV, which may result in a systematically underestimated planetary mass. An unseen planet would in-

[4] Kepler-18bcd, K2-19bc, K2-24bc, Kepler-9bc, Kepler-25bcd, Kepler-56bc, Kepler-419bc, WASP-47bde, Kepler-19bc, Kepler-117bc.

[5] Kepler-18bcd, Kepler-89 cde, K2-19bc, Kepler-9bc, Kepler-419bc, WASP-47bde , Kepler-88c, Kepler-10.

fluence the RVs significantly, and multi-body resonances affect both methods. Another reason could be that compact systems, which are favorably detected by TTVs, have lower planetary bulk densities than non-compact systems because of their strong dynamical interaction (e.g. Lissauer et al., 2013). Additionally, general relativity and tides could affect the dynamics of some close-in planets. Steffen (2016) and Mills & Mazeh (2017) suggest that the differences in their densities do not originate from incorrect results, but from the physical and orbital sensitivities of the two methods. Both methods cover different ranges in the mass-radius plane and are applied to different populations of exoplanets (orbital periods). The RV method favors massive and close-in (short period) planets while the strength of the TTV method depends on the orbital configuration. In general, the ability to measure TTVs is limited by the noise level of the light curves, and the radius of the planet relative to its host star $R_{\mathrm{p}}/R_{\star}$ which is related to the transit depth as $R_{\mathrm{p}}^2/R_{\star}^2$.

Cubillos et al. (2017) found an overabundance of low-density Neptune-like planets when they were analyzing atmospheric escape rates of Neptune-like planets. Their data set consist to 70% of the planets that have masses estimated by TTVs and are in systems with multiple planets. Besides other reasons, they claimed that the planetary masses could be underestimated by the TTV method, and the planetary radii could be overestimated in the optical wavelengths due to high-altitude clouds.

Unresolved companion (or background) stars could be another cause for a misestimated bulk density (Furlan & Howell, 2017). If the observed flux from the host star is contaminated by an unresolved star, the true planetary radius will be larger than the value estimated from the transit light curve (e.g. 1.5 times as pointed out in Furlan & Howell (2017)). Therefore, the planet's bulk density will be underestimated.

Sampling rate The orbits are recorded at the times of transits which leaves room for aliasing. However, the stroboscopic effect (Szabó et al., 2013) is more relevant. This effect arises from the regular sampling of data, in particular when the data has a low time resolution like with the long cadence sampling rate of *Kepler*. In this case, the transit is sampled only at a few points. This effect can lead to an apparent TTV. Nevertheless, this effect can be prevented if the transit model is super-sampled as suggested by Kipping (2010).

Stellar activity can induce apparent TTVs by the Applegate effect in exoplanets (Watson & Marsh, 2010): The rotational bulge of the star changes because of the magnetic cycle, producing variations in the orbital period of the planet. Watson & Marsh (2010) calculated TTV amplitudes of less than one minute for solar-type stars on a time span of several years. Furthermore, stellar spots can produce apparent TTVs. However, spot activity can be resolved by observing the transits in different wavelengths, since stellar spots are darker in the optical wavelengths than in the near-infrared. In general, limb-darkening and gravity-darkening complicate the estimation of accurate transit parameters, and need to be taken into account.

The proper motion of the system with respect to the solar system can cause apparent TTVs (Scharf, 2007; Rafikov, 2009).

The light time delay caused by the reflex motion of the system by an additional third body can produce apparent TTVs.

The signal-to-noise of the light curve determines the ability to detect planets. Normally, small planets are detected by phase folding the light curve to enhance the shallow signal. Therefore, fitting individual transits of small planets is challenging and most studies focused on planets larger than Earth. In general, TTVs produce a smeared phase folded transit because of the changing orbital period if the TTVs are not fitted. This can result in miscalculated transit parameters.

4

PyTTV: Detection of Transit Variations

Several groups have searched for variations in transit times, durations, and depths in the light curves from the *Kepler* mission and made their work public in the form of a data base (Holczer et al., 2016; Kane et al., 2019) or in publications (Yang et al., 2013; Xie, 2013, 2014; Xie et al., 2014; Rowe et al., 2014, 2015; Ofir et al., 2018; Gajdoš et al., 2019). The Kepler team published a series called "Transit timing observations from Kepler" from I to IX (Ford et al., 2011, 2012a; Steffen et al., 2012a; Fabrycky et al., 2012; Ford et al., 2012b; Steffen et al., 2012b, 2013; Mazeh et al., 2013; Holczer et al., 2016), where they reported a number of TTV systems, and also confirmed some of them. In a second series "Validation of Kepler's multiple planet candidates" covering I-III, they validated candidate multi-planet systems statistically and via TTVs, consequently reporting TTVs for the candidates. The two papers by the Kepler team reporting the largest number of TTV systems are by Mazeh et al. (2013) and Holczer et al. (2016). Furthermore, Xie et al. (2014) searched the long cadence light curves of the Kepler Object of Interest (KOI) from Quarters 0-12 (Q0–Q12) for TTVs. Yang et al. (2013), Xie (2013), and Xie (2014) focused their TTV search to planet pairs close to first-order mean motion

resonances based on the long cadence light curves of the KOIs from Q0-Q15, Q0-Q14, and Q0-Q16, respectively. Holczer et al. (2016) searched for transit time, depth, and duration variations in the KOIs listed in the NASA Exoplanet Archive as of November 23 2013[1]. They analyzed the long cadence light curves and updated their data base with short cadence lists later.[2] Kane et al. (2019) took the candidates from the *Kepler* Data Release 25 catalog[3] from Thompson et al. (2018), and used the TTV lists from Holczer et al. (2016), Rowe et al. (2015), and Rowe et al. (2014), and visually inspected the TTVs. Their results are accessible via a data base.[4] They also made a statistical analysis of the transit depth and transit duration measurements from the long cadence lists from Holczer et al 2016.[5] Gajdoš et al. (2019) took also the *Kepler* Data Release 25 catalog from Thompson et al. (2018) and searched the long cadence light curves for TTVs of known planets. In addition to the approach of fitting individual transits used in the previously listed papers, Ofir et al. (2018) developed a method called spectral approach to search for transit timing variations. This method is sensitive to shallower transits and transits from planets with short periods that have only a few in-transit points because it does not require a transit fit. This method helps to detect TTVs, but for a characterization, when the exact transit times are needed, a more conventional transit fitting method is required.

[1] At this time, candidates were listed found in Q0-16 but the light curves for all objects were already public until Q17.

[2] `ftp://wise-ftp.tau.ac.il/pub/tauttv/TTV/ver_117/`. The only description of their work is found in the README.txt.

[3] `https://exoplanetarchive.ipac.caltech.edu/docs/Kepler_KOI_docs.html`.

[4] `https://haumea.byu.edu/kanettv/#DR25.pdf` or `https://haumea.byu.edu/kanettv/#.pdf` where # denotes the KOI number.

[5] `https://haumea.byu.edu/kanettv/CheckTDVTPV.pdf`.

Regardless of all the published results from searches for variations in transit times, depths, and durations, there is no publicly available code to automatically search for those variations. The development of such a code is necessary because the increasing amount of light curves basically impedes the manual search.

Another reason for the development of such a code is that so far no code exists that can automatically search for light curve variations using the photometry of different transit surveys (space-based and ground-based). The need for a code that can search for variations in systems observed with different telescopes (with different exposure times and with different noise properties) is increasing since the start from *TESS*. *TESS* is re-observing fields with known transiting planets observed by *Kepler* and ground-based facilities. The upcoming missions *CHEOPS* and *PLATO* will also observe known transiting planets and increase the observational time span. Combining light curves from different missions enables the search for longer period disturbances in the light curves. Effects described in Sec. 3.1.1 and Sec. 3.1.2 could be observable in a few systems when they are observed over long time (e.g. orbital decay in WASP-12). Monitoring the TTVs for a longer time span is also helpful for constraining the interior structure via the love number (Ragozzine & Wolf, 2009; Patra et al., 2017; Csizmadia et al., 2019).

This section describes a code, `PyTTV`, that has been developed to satisfy the needs mentioned above. The different steps required for the identification of transit variations will be explained exemplarily using the well-studied Kepler-9 system.

4.1. Estimation of Transit Center Times, Durations, and Depths

The estimation of transit center times consists of three steps: a) fast transit center estimation, b) simultaneous modeling of transits from all planets in the system, and c) modeling of individual transits. In all these steps, circular planetary orbits are assumed because the eccentricity is not sufficiently constrained by the transit shape.[6] This approach is valid as long as a correct estimation of the mean stellar density from the transit fit is not required.

The transits are modeled with the quadratic transit model from Mandel & Agol (2002) implemented in `PyTransit` (Parviainen, 2015). For long cadence data, the transit model is super-sampled as suggested by (Kipping, 2010) to ensure a robust transit fit. This approach also rules out the probability to detect an apparent TTV by the stroboscopic effect. The parameter estimation is carried out using a Bayesian approach (e.g. Parviainen, 2018; Gelman et al., 2013). The estimation of the model parameter posterior distribution is carried out in two steps. First, the global posterior mode is found using a global optimization method (Differential Evolution, as implemented in Parviainen, 2015), after which a posterior estimate is obtained using Markov Chain Monte Carlo (MCMC) sampling. The MCMC sampling is carried out with the affine invariant MCMC sampler implemented in the `emcee` package (Foreman-Mackey et al., 2013).

[6] The eccentricity is constrained either by fitting the secondary eclipse or by RV measurements.

4.1.1. Data download

The light curves are either automatically downloaded from the Mikulski Archive for Space Telescopes[7] or added manually. The code uses the Pre-Search Data Conditioning Simple Aperture Photometry (PDCSAP)[8] for *Kepler*, *K2*, and *TESS* data by default, which can be changed on request. Data points with quality flags indicating corrupt data or data of low quality are excluded from the analysis.[9] When two different types of cadences are available for a system, the shorter cadences are favored because they allow a more precise parameter estimation (Fig. 4.1)

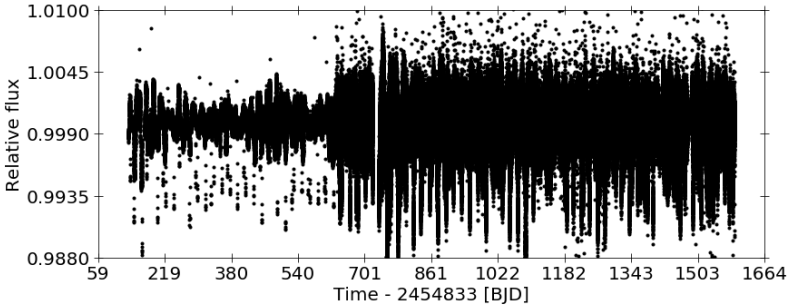

Figure 4.1.: Kepler-9 light curve as observed by *Kepler* in long cadence (until 631.5+2454833 [BJD]) and short cadence mode (starting from 631.5+2454833 [BJD]).

[7] `https://archive.stsci.edu`.

[8] The light curves are corrected for discontinuities and for crowding.

[9] Not taken into account are points with quality flags 1 (Attitude tweak), 2 (Safe mode), 4 (Coarse point), 8 (Earth point), 32 (Desaturation event), 256 (Manual exclude), 8192 (Cosmic ray), 32768 (No fine point), 65536 (No data), and 1048576 (Thruster firing) for *Kepler/K2* light curves. For *TESS* light curves the flags 16 (Argabrightening), 128 (Manuel exclude), 512 (Impulsive outlier), 1024 (Cosmic ray in collateral data), and 2048 (Straylight) are in addition excluded. For the *K2* light curves processed by the `EVEREST` pipeline, flag 16384 (Detector anomaly), 4194304 (Data point is a NaN), and 8388608 (Data point was determined to be an outlier) are also removed.

4.1.2. Initial transit estimation

The analysis starts with a fast estimation of the individual transit center times. The search is carried out by fitting a transit model with a constant orbital period to small overlapping light curve subsets of a given window width. The model is parameterized by the orbital period $P_{\rm orb}$, stellar density $\rho_\star$, and the transit center t_0. Transit centers are estimated by fitting the parameters ($P_{\rm orb}$, $\rho_\star$, and t_0) and averaging the centers from overlapping segments.

A careful treatment of stellar activity needs to be included when searching for small variations. Therefore, the stellar activity is modeled as a Gaussian Process (GP) with hyperparameters learned from the out-of-transit data. The code uses the `celerite` package (Foreman-Mackey et al., 2017) for the GP computations with a Matern 3/2 kernel. The advantage of using `celerite` is that it allows the analysis to be scaled to large data sets.

The window width is set automatically depending on the orbital periods, the number of planets in the light curve, and accounting for the possibility that the orbital periods are close to a period commensurability.

The results of the initial estimation are transit centers for each planet in the system as shown in Fig. 4.2. The different vertical dashed lines mark the transits for Kepler-9b and Kepler-9c in light gray and dark gray, respectively.

4.1.3. Simultaneous transit modeling

As a second step, all transits from all the planets in the system are fitted together simultaneously. The model is parameterized by the transit centers t_c for all planets, impact parameter b for all planets, planet-to-star radius

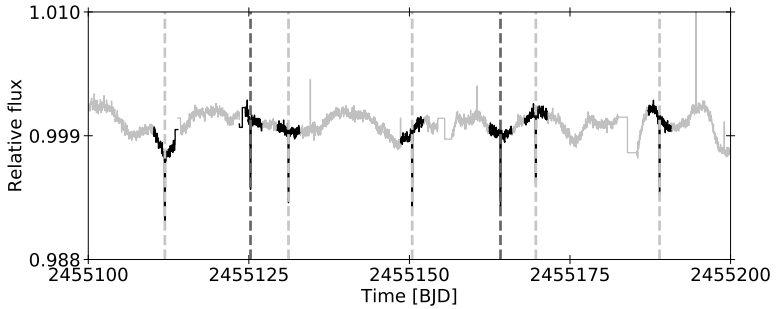

Figure 4.2.: Initial transit center estimates for Kepler-9b and Kepler-9c for a subset of the light curve. The black segments mark the transit window. The transits of Kepler-9b and Kepler-9c are marked with the light and dark gray dashed lines, respectively.

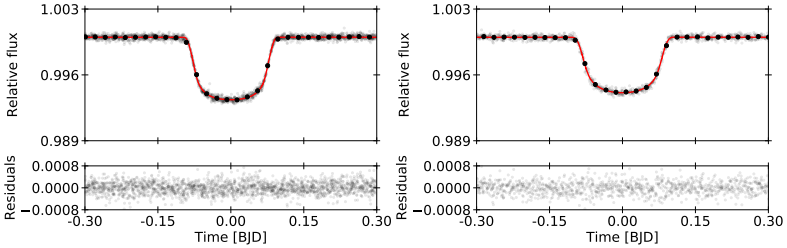

Figure 4.3.: Top panels: phase-folded transits of Kepler-9b (left) and Kepler-9c (right) with their orbital period of 19.24 days and 38.94 days. Each transit is shifted by their mid-transit time estimated by `PyTTV`. The black points are the binned data point with a binning of 30 minutes. The red line is the transit model. Lower panels: fit residuals. Note that in-transit and out-of-transit show the same noise properties indicating that the data are well fitted.

ratio $R_{\mathrm{p}}/R_{\star}$ for all planets, stellar limb darkening coefficients (u, v), and mean stellar density $\rho_{\star}$. The advantage of this approach is that the model

parameters that are constant over time (b and $R_\mathrm{p}/R_\star$) or are independent of the planet (u, v, and $\rho_\star$) are shared. This means that those parameters are fitted only once and thus, the number of parameters is reduced, and the parameters are better constrained. Therefore, the approach gives more accurate parameter posteriors, and the model reproduces simultaneous transits correctly. The priors for the transit centers are based on the initial estimation. The stellar variability is modeled again as a GP where the hyperparameters are taken from the initial estimation.

The results of the simultaneous transit modeling are transit models for each planet in the system (Fig. 4.3) and more accurately modeled transit centers. Overlapping or very close transits are also modeled correctly (Fig. 4.4).

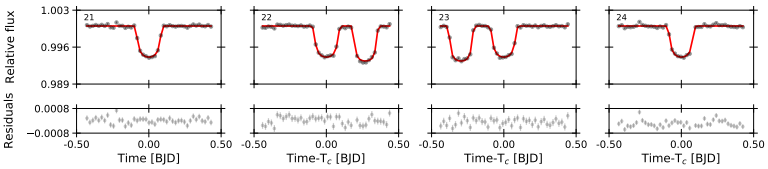

Figure 4.4.: Transits for Kepler-9b and Kepler-9c simultaneously fitted. Note that even very close transits are modeled correctly. The transits for Kepler-9b are the deeper transits. Each transit of Kepler-9c is shifted by their mid-transit time estimated by `PyTTV`. The transits were observed in the long cadence mode (black points). The red line is the transit model. Lower panels: fit residuals.

4.1.4. Individual transit modeling

As a third step, each transit of every planet is fitted separately by setting priors taken either from the simultaneous fit or from the initial estimation. This step enables to estimate the transit duration and the transit depth sep-

arately for each transit. The transit duration is calculated from the fitted impact parameter b, stellar density $\rho_\star$, orbital period P, and radius ratio $R_\mathrm{p}/R_\star$. The same priors and model parameterization as for the simultaneous transit modeling are used.

The results of the individual transit modeling are individual transit depth and duration estimates for every individual transit of every planet in the system.

The reason for separate simultaneous and individual modeling is that the simultaneous modeling assumes constant transit duration and depth and obtains accurate posterior estimates for these parameters if the assumption holds, while the individual modeling allows for the search for variations in these parameters and a robust estimate of their uncertainties. This approach has been already used in some other publications (e.g. Holman et al., 2010; Xie, 2013; Nesvorný et al., 2013).

The run time for the transit modeling depends on the number of planets in the system, the orbital periods (number of transits), and cadence rates. On a standard i7-8550U CPU with 1.8 GHz x 8, `PyTTV` takes for the Kepler-9 system around three hours for fitting the long cadence light curves and around six times longer for the short cadence light curves. The second step (simultaneous transit modeling) is the most time-consuming. The difference between the transit times calculated by the individual and simultaneous transit modeling is shown in Fig 4.5. The difference between both modeling steps is usually smaller than 1 minute (shaded area) and thus smaller than the uncertainty and can, therefore, be neglected, except for some transit times where the difference is larger. These outliers are mostly due to bad ingress/egress sampling and very close transits of both planets (see Fig. 4.4). These outliers are removed in the simultane-

ous modeling but appear in the individual modeling. One drawback of the individual transit modeling is thus, that overlapping or very nearby transits are not modeled correctly, especially when the transits have the same depth as it is the case for Kepler-9b and Kepler-9c. The outliers are removed in a later step. Since the simultaneous modeling needs notably more time, it is recommended to use the simultaneous modeling of the short cadence light curves only if overlapping and close transits occur frequently as in the case of a compact planet system.

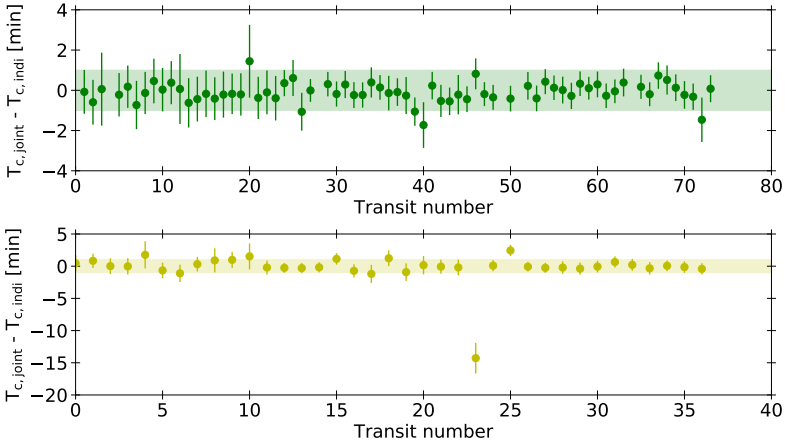

Figure 4.5.: Difference in the transit center estimates from the simultaneous $T_{c,joint}$ and individual $T_{c,indi}$ transit modeling for Kepler-9b (top panel) and Kepler-9c (lower panel). The shaded areas mark 1 minute. Some outliers are visible in both panels mostly due to bad ingress/egress sampling and very close transits of both planets.

The transit times estimated from the individual transit modeling are compared to other publicly available transit center estimates in the literature (Fig. 4.6). The difference between the transit center times derived by

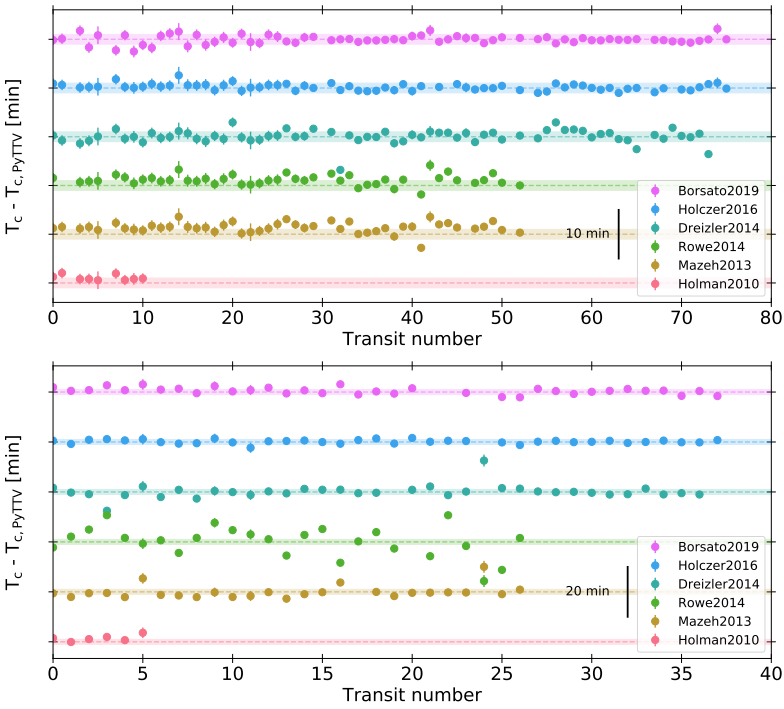

Figure 4.6.: Difference in the transit centers from the individual transit modeling with `PyTTV` and transit centers from the literature for Kepler-9b (top panel) and Kepler-9c (lower panel). The shaded area marks 1 minute. The difference between the estimates increases from the top (newer studies) to the bottom (older studies) for each planet.

`PyTTV` and the literature values increases from the top line (pink; Borsato et al., 2019) to the lower line (red; Holman et al., 2010). The newer estimates (Borsato et al., 2019; Holczer et al., 2016; Dreizler & Ofir, 2014) used long and short cadence *Kepler* data like `PyTTV`, while the earlier

studies used only the long cadence *Kepler* light curves. The earlier studies show also more scatter in the transit center times, especially the transit center times for Kepler-9c from Rowe et al. (2014). The times from Mazeh et al. (2013) and Holman et al. (2010) are systematically lower or higher than the transit times derived by `PyTTV`. Overall, it can be concluded that the individual transit modeling estimates robustly the transit times and reaches or exceeds the same accuracy as existing codes.

4.2. Identification of Variations

After the transit times, durations, and depths are extracted, they are further analyzed for variations. First, the outliers with anomalously large transit center uncertainties are removed. These can be caused by missing data or uncorrected systematics. In detail, transits with $\sigma_c > 10 \times$ Median Absolute Deviation are removed.

For the search for variations and periodicities in TTVs, a linear or quadratic model is fitted and subtracted from the transit centers to obtain the TTVs (Fig. 4.7). The transit durations and depths are used without subtracting a model (Fig. 4.8).

The generalized Lomb-Scargle periodogram from Zechmeister & Kürster (2009) (`GLS`) is used to search for periodicities in the TTVs as well as in the transit durations and depths (Fig. 4.9). The difference to traditional Lomb-Scargle (Lomb, 1976; Scargle, 1982) periodograms is that the GLS allows for an offset and weights, making the frequency determination more reliable. The GLS is also less prone to aliasing, and gives a more accurate determination of the spectral power (Zechmeister & Kürster, 2009). The `GLS` as implemented here, searches for periodicities in the range between twice the orbital period until twice the observation time span. The

lower limit was chosen because of the Nyquist frequency. The higher limit was chosen since the frequency analysis carried out by GLS cannot identify periods much longer than the observation time span, but at the same time, however, it should be searched for long-term slopes.

A feature of the GLS package is that it automatically calculates the best-fitting parameters and their uncertainties, especially the amplitude, phase, offset, and period of the detected periodicity. Those parameters can be used for an analytical derivation of physical quantities (e.g. Lithwick et al., 2012). In the case of the Kepler-9 system, the anti-correlated TTVs are almost reproduced by detected periodicities and phases (see Fig. 4.9 and Table 4.1).

To test the significance of a signal, several statistical calculations are considered within the GLS package. The first diagnostic is the probability that the detected power of the signal is obtained purely from noise. The second diagnostic, the false alarm probability (FAP), gives the significance of the detected peak compared to peaks at other frequencies. Variations

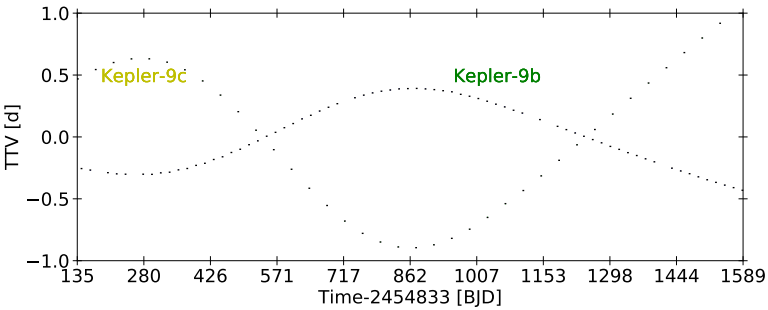

Figure 4.7.: TTVs of Kepler-9b (green) and Kepler-9c (yellow) obtained with PyTTV. The anti-correlation is clearly visible.

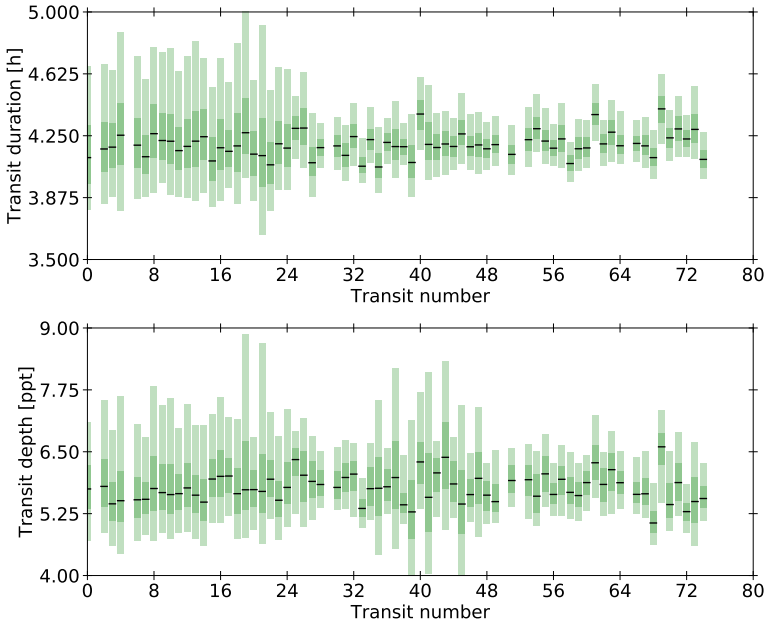

Figure 4.8.: TDVs (top panel) and TPVs (lower panel) of Kepler-9b obtained with `PyTTV`. Note the effect of the different cadences on the estimated uncertainties; short cadences lead to smaller uncertainties and therefore are preferred when searching for small scale variations as in the transit depths and durations. The dark and light green bars mark the 1σ and 3σ uncertainties, respectively.

with a FAP lower than 10^{-3} are considered as significant. The TTVs in the Kepler-9 system are well below this limit and therefore automatically detected as significant (Table 4.1). Since the TTV period is longer than the upper limit of the search interval, the "correct" TTV period is not detected.

To find out which of the models (linear trend, quadratic trend or sinusoidal model) is best-suited, the Bayesian Information Criterion (BIC) is

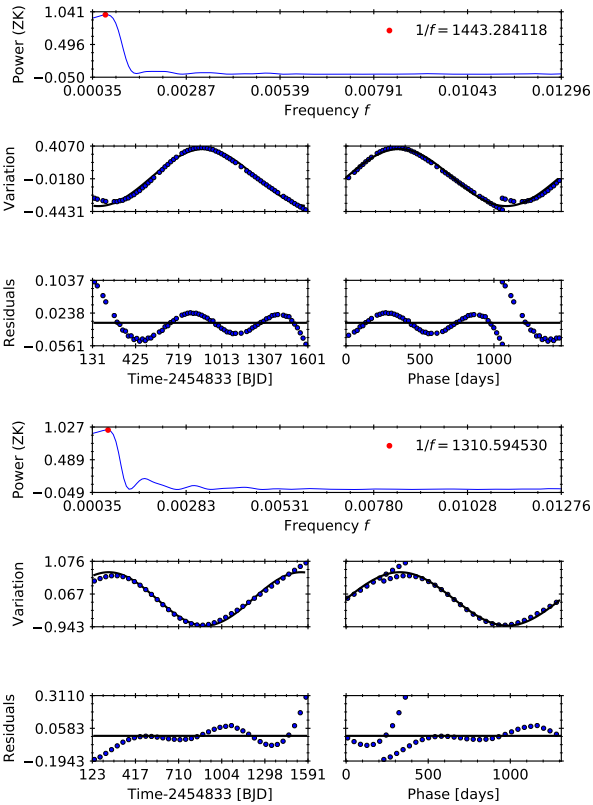

Figure 4.9.: GLS periodogram of Kepler-9b (top three panels) and Kepler-9c (lower three panels). The top individual panel shows the power spectrum of the signal with the highest peak marked with the red point. The period of the highest peak is reported in the top right of the power spectrum panel. The middle panels show the variation in time (left) and in phase (right). The lower panels show the residuals; on the left side for the time and on the right side for the phase. Note that anti-correlated TTVs are well reproduced by the detected periodicity. However, the correct TTV period is not detected noticeable in the high scatter in the residuals since the TTV period is longer than the observation time.

calculated:

$$\mathrm{BIC} = d \cdot ln(n) - 2ln(L), \tag{4.1}$$

where L is the maximized likelihood for the model M according to $L = p(\vec{x} \mid \vec{\theta}, M)$. The parameter vector $\vec{\theta}$ corresponds to parameters maximizing the likelihood function, $\vec{x}$ are the observed data, n is the number of data points (e.g number of transits) and d is the number of free parameters of the model. The model with the lowest BIC is chosen as the best model and the significance of the other models with respect to the best model is calculated via the $\Delta\mathrm{BIC}$. A linear model detected for the TTVs means that the transit times follow a linear period and that there is no TTV. Since the transit depths and durations are used directly for variations without subtracting linear trend, a linear model for the transit durations and depths indicate a variation while a constant model implies no variation. The sinusoidal model has the lowest BIC for the TTVs for Kepler-9b and Kepler-9c. The variations in the transit durations reported in Borsato et al. (2019) are not detected but instead modeled with a constant. The transit depths are found to be constant (Table 4.1).

The Pearson correlation coefficient is calculated to test if the variations are correlated. The Pearson correlation coefficient estimates if two signals are correlated (1), anti-correlated (-1) or not correlated (0) assuming Gaussian noise. Here, correlations between either the linear and quadratic terms are considered, as well as correlation between TTVs and variations in transit duration and depth. Strong correlation can be an indicator for systematic effects or stellar variability[10].

When observations with different cadences are available, it is checked if

[10]The influence of stellar variability is taken into account by the GP, but strong stellar variability can still affect on the estimated quantities.

Table 4.1.: Diagnostics of the Kepler-9 system. The values for ϕ are reported as normalized phase with values [0,1], allowing for negative values. The models representing the TTVs, TDVs, and TPVs with the lowest BIC are reported. The TTVs for both planets are found to be significant.

Kepler-9b: 19.246 ± 0.002 days			
	TTV	TDV	TPV
Model	sin	con	con
Period [days]	1443.3 ± 34.7	-	-
Amplitude [min]	534.5 ± 6.0	-	-
Phase	-0.268 ± 0.002	-	-
FAP	7.5e-26	-	-
Kepler-9c: 38.948 ± 0.009 days			
	TTV	TDV	TPV
Model	sin	con	con
Period [days]	1310.6 ± 41.4	-	-
Amplitude [min]	1187.0 ± 28.8	-	-
Phase	175 ± 0.004	-	-
FAP	7.4e-11	-	-

a long-cadence signal is detected in short cadence data. A positive match reveals that the detected variation is not spurious but instead existing in the data. Of course, this will not work the other way because some variations might be only detectable using the higher cadence rates.

4.3. Validation of PyTTV

`PyTTV` is tested with known systems. A typical TTV system with a planet pair near a first-order mean motion resonance was already presented via the example case of the Kepler-9 system (Fig. 4.7). Further systems are

carefully chosen to cover a wide range of different orbital architectures and to show the code's abilities:

Kepler-117 a two-planet system with period ratios far from a period commensurability with an atypical periodicity.

Kepler-693 an eccentric two-planet system with an inclined perturbing planet showing a "bump" in the TTVs.

Kepler-88 a three-planet system where only one planet is transiting and exhibiting one of the strongest TTVs so far detected.

TOI-193 and WASP-18 two single-transiting systems where no TTVs have been detected.

The plots in the next subsections are the automatically created plots without beautifying them afterwards and without manual post-processing. This decision was made to show the code's ability to work automatically.

Kepler-117 is a system with two transiting planets orbiting an F9 type star. It was identified by Borucki et al. (2011a) as a multi-planet system, and Steffen et al. (2010) marked it as a system expected to show TTVs. Rowe et al. (2014) validated the planet candidates in the system, and their TTVs were later analyzed by Bruno et al. (2015). Kepler-117 is an unusual TTV system because the planetary orbital periods are 18.8 days and 50.8 days, and thus far away from period commensurability. Almenara et al. (2015) studied the system via a photodynamical model and detected small variations in the transit durations of Kepler-117b with an amplitude of ~ 15 minutes. Wu et al. (2018) recently re-analyzed this system using the transit times from Holczer et al. (2016) using `TTVFast` (Deck et al.,

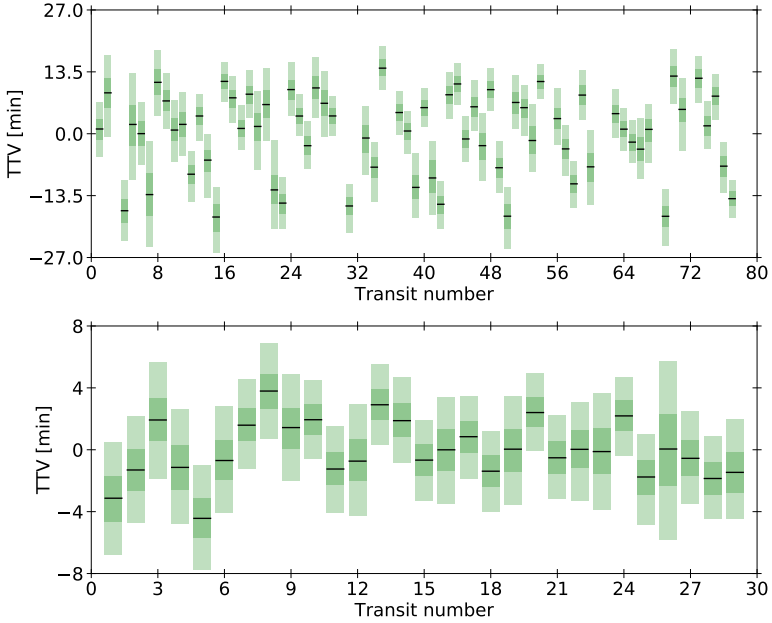

Figure 4.10.: TTVs of Kepler-117b (top panel) and Kepler-117c (lower panel). The dark and light green bars mark the 1σ and 3σ uncertainties, respectively. Both TTVs look more like noise than a significant signal.

2014) for the parameter estimation. Their results agree within 1σ with the results from Bruno et al. (2015), but are not described in detail.

The Kepler-117 system is included in the data base from Holczer et al. (2016), but without significant transit variations. It can be easily missed if no further search for periodicities is carried out because of the shape of the TTVs. Thus, Gajdoš et al. (2019) called the TTVs for Kepler-117b "abnormal" with a chaotic behavior. The data base from Kane et al. (2019) includes the TTVs, but the detected periodicities differ.

The TTVs of Kepler-117b and Kepler-117c with their 3σ uncertainties estimated from the long cadence and short cadence light curves by `PyTTV` are shown in Fig. 4.10. They agree with the TTVs in Fig. 6 from Almenara et al. (2015).[11] The TTVs do not show a sinusoidal periodicity, but look rather like uncorrelated noise. However, the periodograms uncover the periodicity in the transit time variations (see Fig. 4.11). The peaks detected by the `GLS` periodogram correspond to the modulation periods of different resonances (3:1 resonance) as mentioned by Almenara et al. (2015) and also found by Ofir et al. (2018). The transit durations for Kepler-117b show a linear trend of $(7.09 \pm 0.03) + (0.0044 \pm 0.0008) \times$ x hours, where x is in epochs. The transit duration variations detected by Almenara et al. (2015) are not reproduced with the same strength but show qualitatively the same trend. This is also confirmed by Kane et al. (2019) who also did not detect the strong transit duration variation as presented in Almenara et al. (2015). One explanation for this could be that Almenara et al. (2015) used the Simple Aperture Photometry light curve[12], which they corrected for the flux contamination using the 'CROWDSAP' value in the fits file header and `PyTTV` and Kane et al. (2019) used the PDCSAP light curve. Therefore, it more probable that the variations in the transit duration are produced by the different detrending approaches used in the analyses. No other variations have been detected as significant by the BIC.

Although the "correct" periodicity (TTV-period) is not revealed until more transit observations are available,[13] `PyTTV` detected this system automatically as a system that is worthy of further investigation, and the

[11] Note that they show only the 1σ uncertainties.

[12] The Simple Aperture Photometry light curves are not corrected for systematics, in contrast to the PDCSAP light curves.

[13] *TESS* observations of this star are available in the Full Frame Image (FFI) but the star is at the edge of a Charge-Coupled Device, so no light curve could be extracted from the FFI.

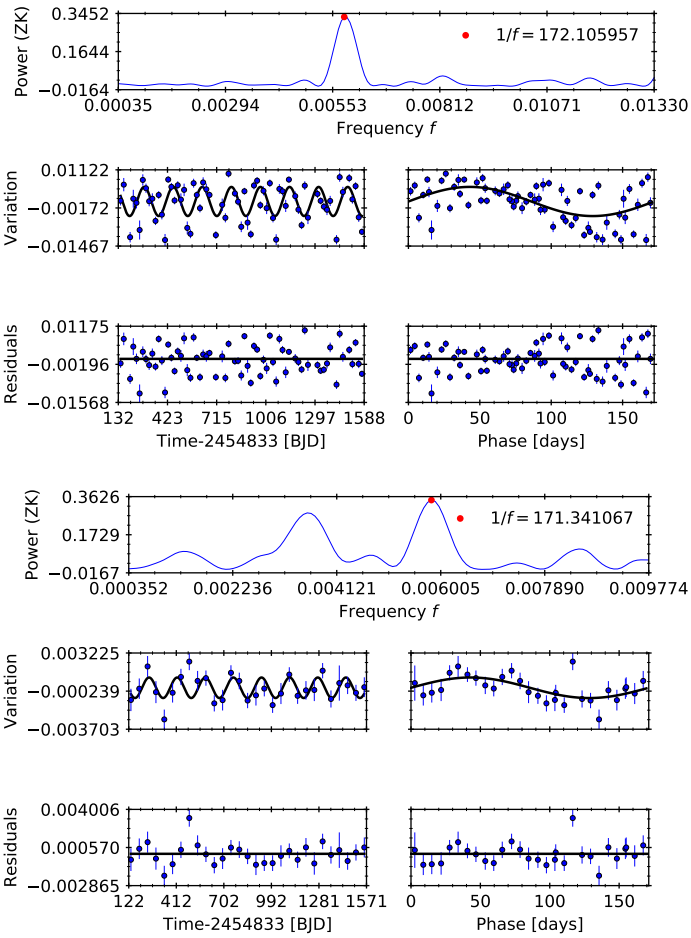

Figure 4.11.: GLS periodogram of Kepler-117b (top panel) and Kepler-117c (lower panel). The description is the same as in Fig. 4.9. The detected peak corresponds to the modulation periods of different resonances as mentioned by Almenara et al. (2015) and Ofir et al. (2018).

Table 4.2.: Diagnostics of the Kepler-117 system. The values for ϕ are the normalized phase with values [0,1], allowing for negative values. TTVs for Kepler-117b are detected as significant, but the periodicities are modulation periods of different resonances as mentioned by Almenara et al. (2015) and Ofir et al. (2018). The transit durations for Kepler-117b follow a linear trend.

Kepler-117b: 18.79592 ± 0.00003 days			
	TTV	TDV	TPV
Model	sin	lin	con
Period [days]	172.1 ± 2.8	-	-
Amplitude [min]	7.1 ± 1.2	-	-
Phase	10.44 ± 0.03	-	-
FAP	4.7e-05	-	-
Kepler-117c: 50.791 ± 0.001 days			
	TTV	TDV	TPV
Model	sin	con	con
Period [days]	171.3 ± 4.5	-	-
Amplitude [min]	1.3 ± 0.4	-	-
Phase	-0.39 ± 0.04	-	-
FAP	0.05	-	-

system passes all the diagnostics (see Table 4.2).

Kepler-693b is a warm Jupiter in an eccentric orbit that has a non-transiting eccentric sub-stellar companion. It was first identified as a candidate by Batalha et al. (2013), and the TTVs were estimated by Rowe et al. (2014). The companion was detected and characterized by Masuda (2017) through dynamical modeling of the TTVs and TDVs.[14] The TTVs show a non-sinusoidal shape with a special "bump" (see Fig. 4.12). This

[14] Masuda (2017) analyzed a second system that is presented in Sec. 4.12.

feature in the TTVs is very likely related to the periastron passage by an outer eccentric companion as suggested by Masuda (2017) and previously mentioned in (Borkovits et al., 2003; Agol et al., 2005; Borkovits et al., 2011) and helps to uniquely determine the physical quantities. Here, the main features are summarized, see Borkovits et al. (2011) for a detailed explanation of the hierarchical triple scenario. The companion exerts tidal forces on the transiting planet leading to an increase in its orbital period. Since the tidal forces depend on the distance between the planets, they are strongest when the perturbing object is at periapsis, which leads to a delayed transit, producing a "bump". Therefore, the detection of this feature helps to determine the orbital period of the perturber. The TTV period coincides with the orbital period of the perturbing object. The edges of "bump" depend on the eccentricity; the more eccentric the perturber's orbit, the more pronounced the "bump".

The variations in the parameters estimated by `PyTTV` are shown in Fig. 4.12. The transit times, durations, and depths show the same trend as in Masuda (2017). A sinusoidal variation was detected for the TTVs, while for the TDVs and TPVs, long term trends have been detected that might be verified or refuted in the future. The TDVs are best represented by a linear trend: $(3.30 \pm 0.05) + (-0.0032 \pm 0.0009) \times$ x hours, where x is given in epochs. The transit depths follow also a linear trend $((0.0140 \pm 0.0003) + (-18.3 \pm 4.8) \times 10^{-6} \times$ x ppt, where x is given in epochs). The detected periodicity (Table 4.3) for the TTVs is dominated by the "bumb".

The comparison of the TDVs estimated with `PyTTV` with the results from Masuda (2017) exhibit some differences. The transit durations derived by `PyTTV` are always longer than the transit durations estimated by Masuda (2017). Masuda (2017) calculated the transit durations as an

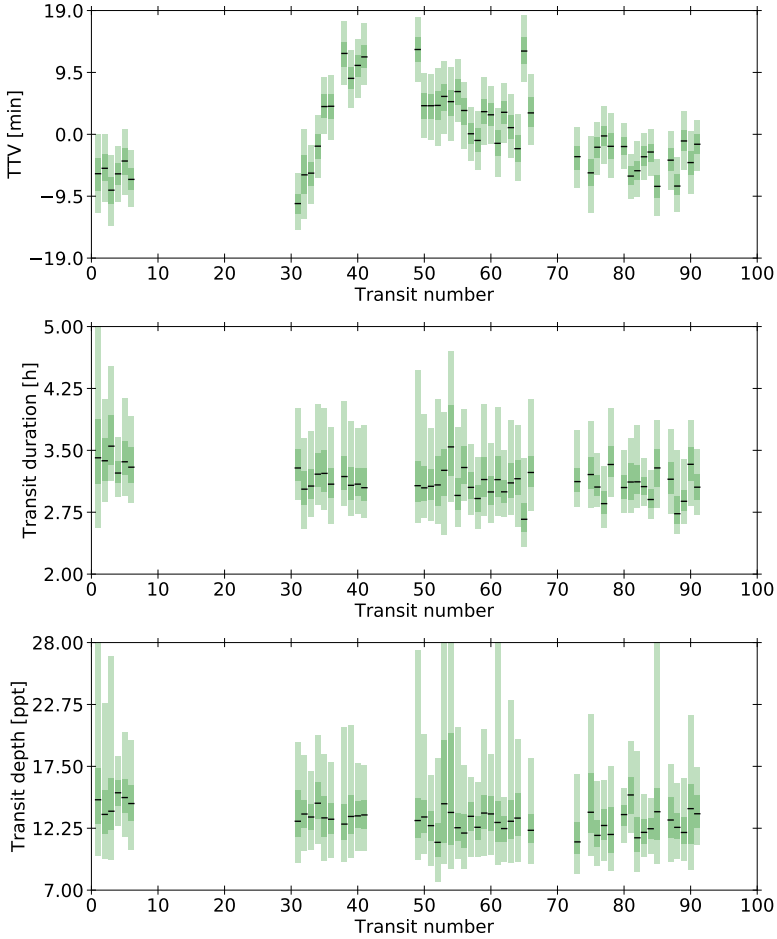

Figure 4.12.: TTVs (top panel), transit durations (middle panel), and transit depths (lower panel) of Kepler-693b. Note the "bump" in the TTVs.

Table 4.3.: Diagnostics of Kepler-693b. The value for ϕ is reported as normalized phase with values [0,1], allowing for negative values. While the BIC prefers a sinusoidal model for the TTVs, the transit durations and depths follow a linear trend.

Kepler-693b: 15.37599 ± 0.00006 days			
	TTV	TDV	TPV
Model	sin	lin	lin
Period [days]	384.4 ± 17.0	-	-
Amplitude [min]	4.4 ± 0.7	-	-
Phase	-0.38 ± 0.02	-	-
FAP	1.3e-06	-	-

average between the total and full duration (see Eqs. 2.3 and 2.5), while `PyTTV` is using the total duration. Another difference in the analysis is the treatment of the short cadence and long cadence data. Masuda (2017) fitted the short cadence and long cadence data independently and averaged the resulting transit center times and durations, while here a more reliable approach was used by fitting long and short cadence data simultaneously. Holczer et al. (2016) and Kane et al. (2019) detected variations in the TTVs in the system as well as variations in depths and durations, whereas Gajdoš et al. (2019) have not analyzed this system. In summary, the Kepler-693 example shows that `PyTTV` can automatically identify variations even with an unusual shape and a sudden change in the variations as significant.

Kepler-88b's TTVs were first identified by Ford et al. (2011) using the initial *Kepler* Quarters, and Mazeh et al. (2013) reported a large amplitude of ~ 12 hours. The Kepler-88b TTVs are among the largest detected.

Nesvorný et al. (2013) analyzed the transits of Kepler-88b and discovered a periodic variation in the transit durations almost in phase with the TTVs. In addition to the TTVs and TDVs, Nesvorný et al. (2013) detected also a "chopping" signal that can help to find a unique solution for the physical quantities. Combining the TTVs, TDVs, and the "chopping", Nesvorný et al. (2013) found a unique solution for the perturbing planet (Kepler-88c) being just wide of the 2:1 resonance with a mass of 0.626 ± 0.03 $\mathrm{M_{Jup}}$. Their results were later confirmed by Barros et al. (2014) using RV observations with the SOPHIE spectrograph ($0.76^{+0.32}_{-0.16}$ $\mathrm{M_{Jup}}$). This was the first confirmation of a non-transiting planet that was previously detected only via TTVs, proving the validity of both methods. Denham et al. (2019) searched for hidden companions in the Kepler-88 system and found that an inclined planet could exist for many configurations. Recently, Weiss et al. (2019) discovered a third distant companion (Kepler-88d) in the system via RV observations spanning six years with an orbital period of 1414^{+27}_{-23} days and a minimum mass of $M_{\mathrm{p}} \sin i = 959 \pm 57$ $\mathrm{M_{\oplus}}$ in an eccentric orbit ($e = 0.432 \pm 0.048$). Because of its strong TTV, all the other studies have detected the TTVs and/or TDVs of Kepler-88b (Holczer et al., 2016; Kane et al., 2019; Gajdoš et al., 2019).

`PyTTV` identified the TTVs and TDVs of Kepler-88b as significant (Fig. 4.13 and Fig. 4.14). TTVs and TDVs reveal the same shape as in Nesvorný et al. (2013); being almost in phase with each other ($\mathrm{P_{TTV}} = 611.2 \pm 3.8$ days and $\mathrm{P_{TDV}} = 663.0 \pm 40.6$ days with $\phi_{\mathrm{TTV}} = 0.295 \pm 0.003$ and $\phi_{\mathrm{TDV}} = 0.37 \pm 0.03$; see Table 4.4). Note that the `GLS` periodogram did not automatically find the correct sinusoidal. Therefore, the residuals show some variations including the "chopping" signal. But again, these are the diagnostic plots for visualizing the automated pipeline, and the system was automatically identified as showing significant variations in TTVs and

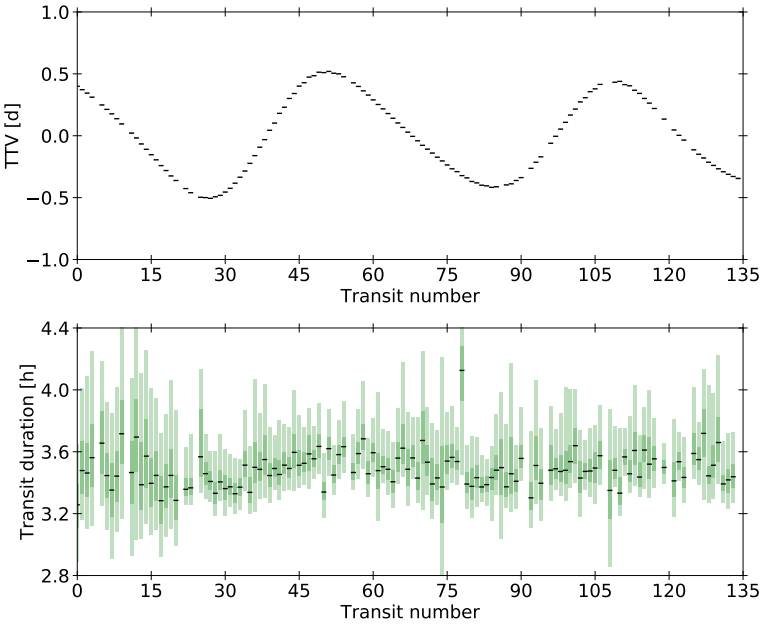

Figure 4.13.: TTVs (top panel) and TDVs (lower panel) of Kepler-88b. Note that the uncertainties for the TTVs of Kepler-88b are not visible because of the scale in the top panel. It is clearly visible that TTVs and TDVs are almost in phase with each other ($P_{\mathrm{TTV}} = 628.7 \pm 4.2$ and $P_{\mathrm{TDV}} = 652.7 \pm 39.1$ with $\phi_{\mathrm{TTV}} = 0.329 \pm 0.003$ and $\phi_{\mathrm{TDV}} = 0.36 \pm 0.02$).

TDVs even though the analysis requires some manual post-processing to improve and correct some of the automatically generated plots. The example of Kepler-88b shows that `PyTTV` can identify strong TTVs robustly.

TOI-193 and WASP-18 are two systems recently analyzed by Pearson (2019) using the first three Sectors of *TESS* light curves to search for non-

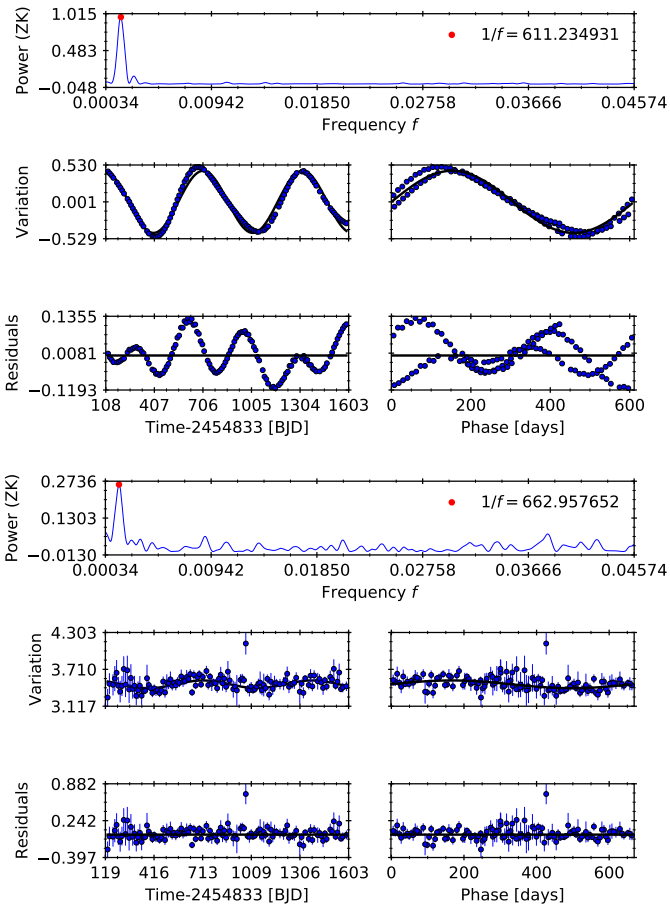

Figure 4.14.: GLS of TTVs (top panel) and TDVs (lower panel) of Kepler-88b. The description is the same as in Fig. 4.9. Note that the periodogram did not find the correct sinusoidal TTV period for Kepler-88b and the residuals still contain some variations including the "chopping" signal. It is clearly visible that TTVs and TDVs are almost in phase with each other.

Table 4.4.: Diagnostics of Kepler-88b. The value for ϕ is reported as normalized phase with values [0,1], allowing for negative values. Variations in transit times and durations are found by best modeled via a sinusoidal with almost the same period and phase. No variations in the transit depths were detected.

Kepler-88b: 10.9530 ± 0.0007 days			
	TTV	TDV	TPV
Model	sin	sin	con
Period [days]	611.2 ± 3.8	663.0 ± 40.6	-
Amplitude [min]	642.2 ± 10.9	3.7 ± 0.6	-
Phase	0.292 ± 0.003	0.37 ± 0.03	-
FAP	9.3e-87	9.0e-07	-

transiting planets using an artificial intelligence vetting algorithm. They reported three new planets that exhibit TTVs and form three new multi-planet systems: WASP-18, WASP-126, and TOI-193. While WASP-126b (Maxted et al., 2016) and WASP-18b (Hellier et al., 2009) are known planets, TOI-193 is a new system observed by *TESS*. Pearson (2019) estimated the parameters of the three new non-transiting planets using a neural network.

The analyses for WASP-18 and TOI-193 are discussed in the following. The analysis for WASP-126b follows later in Sect. 4.4.1, because the WASP-126b analysis includes four times more data than in the analysis by Pearson (2019) and can be considered as a much more extensive and new work.

TOI-193.01 is a USP planet candidate from *TESS* orbiting its G-type host star on a 0.79 day orbit. The TTVs for Tess Object of Interest (TOI), TOI-193.01, are shown in Fig. 4.15 using two Sectors of *TESS* light curves.

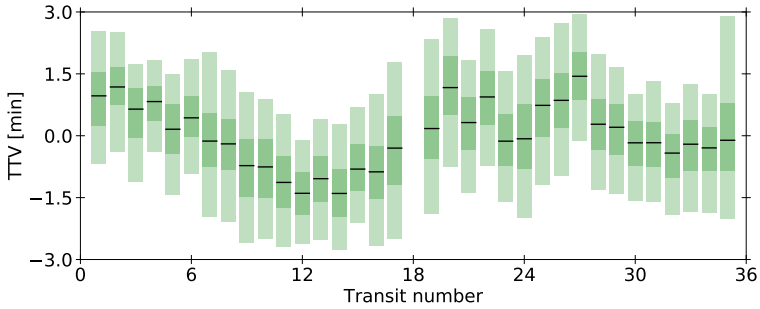

Figure 4.15.: TTVs of the TOI-193.01 observed in two Sectors by *TESS*. The shape indicates some variations, but these are not considered significant by the ΔBIC because of the small number of transits.

The linear model is preferred by BIC, but the BIC is not a reliable diagnostic in this case because of a small number of transits (see Table 4.5). The shape of the TTVs looks more like a sinusoidal variation as in Pearson (2019). Therefore, additional observations for this system are recommended.

WASP-18b is a massive hot Jupiter orbiting its F-type host star with an orbital period of 0.94 days (Hellier et al., 2009), making it an ideal system for star-planet interaction studies (Arras et al., 2012; Albrecht et al., 2012). WASP-18b is a USP planet in a well-studied system revealing the existence of interesting dynamical behavior. Its secondary eclipses have been measured by Nymeyer et al. (2011) and Kedziora-Chudczer et al. (2019), and its phase curve has been studied by Maxted et al. (2013) and Shporer et al. (2019). Because of its short period, it has been suggested that the planet spirals inward on a timescale much shorter than the lifetime of the star under the assumption of $Q'_\star = 10^6$ (Hellier et al., 2009). Otherwise,

$Q'_\star$ is expected to be much higher than 10^6. Hellier et al. (2009) estimated that if the value for $Q'_\star = 10^6$ is correct, this accumulates in TTVs of 28 seconds after ten years, leading to rapid orbital decay. Southworth et al. (2009) presented new transits and found an eccentric orbit for WASP-18b whereby the tidal effects are weaker as suggested by Hellier et al. (2009). Watson & Marsh (2010) mentioned that in systems like WASP-18, the Applegate mechanism could be misinterpreted as orbital decay. Birkby et al. (2014) calculated the transit shift because of tidal dissipation of 356 seconds after ten years (their Fig. 14) assuming $Q'_\star = 10^6$ that is several times stronger than the transit shift estimated by Hellier et al. (2009). Wilkins et al. (2017) searched for variations in the transits and eclipses covering a time span of almost ten years, and found no evidence for rapid orbital decay. They concluded that $Q'_\star$ must be significantly larger supporting the results form Barker & Ogilvie (2009) for F-type stars. In another study, McDonald & Kerins (2018) detected transits of WASP-18b in the Hipparcos data, and used this to derive the orbital decay even for a longer time span. They found tentative orbital decay, but because of the large uncertainties, it is not very likely to be real. Therefore, they recommended measuring new transit times to decrease the uncertainties. Csizmadia et al. (2019) estimated the fluid Love number using RV, transit, and secondary eclipses data resulting in an apsidal motion with a rate of $0.0087 \pm 0.0033^\circ$ corresponding to 31.3 ± 11.8 arcseconds day^{-1}. They converted this rate into a TTV amplitude of 3.7 minutes and a sinusoidal TTV curve with a period of 266 years indicating an annual change of 0.01 seconds per year. This is in agreement with the non-detection of TTVs by Wilkins et al. (2017). Csizmadia et al. (2019) identified the relativistic effect and the tidal interaction as the main contributors to the apsidal motion. Furthermore, they detected a stellar companion to WASP-18 and found its

contribution to the precession to be negligible. However, pointed out by the authors, this companion could excite the eccentricity of WASP-18 and impede its orbital circularization. An unseen additional planet is not likely due to the lack of TTVs, and the lack of an RV trend (Csizmadia et al., 2019). Shporer et al. (2019) analyzed also the transit times from the *TESS* mission and found no evidence for TTVs. They combined the *TESS* light curves with all available transit times (~ 10 years) and found also no long-term trend in the TTVs.

The contradicting results in the previous studies motivated the underlying re-analysis of the *TESS* light curves. The light curves form *TESS* Sectors 2 and 3 are analyzed by `PyTTV` and the TTVs are shown in Fig. 4.16. No evidence for short-term TTVs was detected, but the TTVs show a marginal sinusoidal behavior with a period of ~ 10 days. This periodicity was not significant over the linear ephemeris (Table 4.5). The best model to the transit durations is a linear model $(2.19 \pm 0.002) +$ $(-0.00041 \pm 0.00007) \times$ x hours, where x is in epochs. The transit depths are best fit by a sinusoidal model (FAP = 4.4e-10) with a period of 19.1 ± 0.5 days and an amplitude of 153.0 ± 15 ppm. It can be seen from Fig. 4.16 that the variations show a jump and are not continuous after each gap in the *TESS* light curve. More data are needed to rule out a systematic effect producing apparent variations in all three parameters. The previously published transit time measurements are also searched for variations in the transit centers (Fig. 4.17). No long-term TTVs has been detected in agreement with the results from Shporer et al. (2019). The suggested transit shift of around 4 minutes caused by orbital decay assuming $Q'_\star = 10^6$ in Fig. 3.4 is not detected after ten years. Therefore, tidal dissipation factors $Q'_\star \leq 10^6$ are ruled out by the TTVs. A tidal dissipation factor of $Q'_\star = 10^7$ causes a shift of around 1 minute. This shift is within the uncertainties

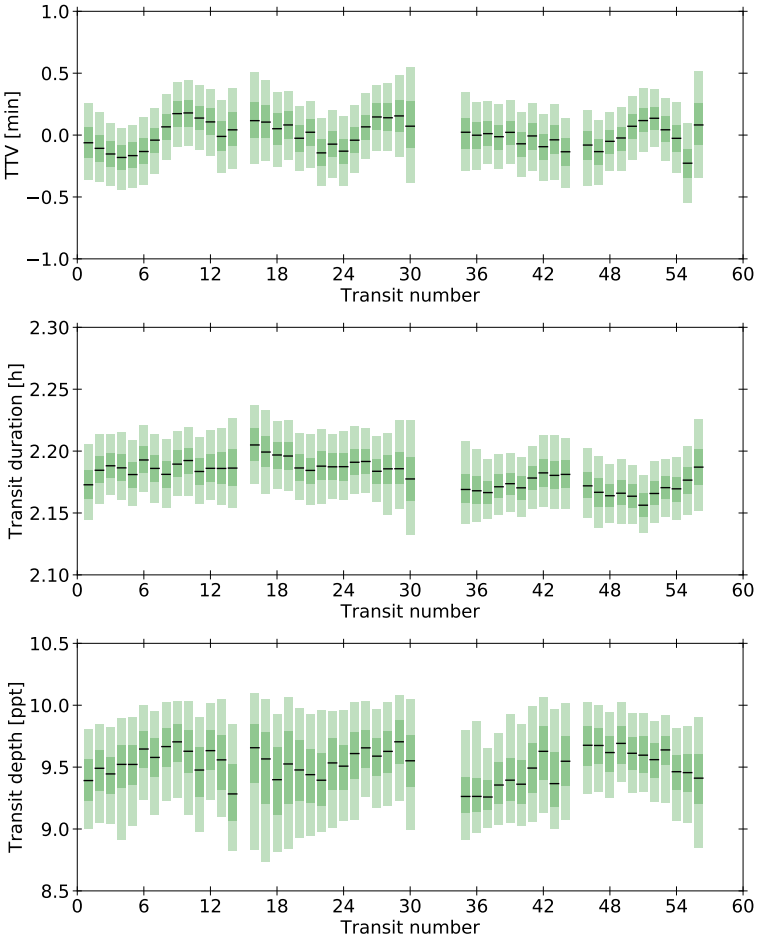

Figure 4.16.: TTVs (top panel), transit durations (middle panel), and transit depths (lower panel) of WASP-18b. TTVs of the WASP-18b show no significant TTVs but a marginal sinusoidal model with a period of $\sim$ 10 days can be seen. The transit durations show a linear trend and a sinusoidal model fits the transit depths the best.

Table 4.5.: Diagnostics of TOI-193.01 and WASP-18b. The values for ϕ are reported as normalized phases with values [0,1], allowing for negative values. The TTVs show no variations for TOI-193.01 and WASP-18b. While the transit durations for WASP-18b follow a linear trend, the transit depths are found to follow a sinusoidal model.

TOI-193.01: 0.79208 ± 0.00002 days			
	TTV	TDV	TPV
Model	lin	con	con
WASP-18b: 0.941453 ± 0.000001 days			
	TTV	TDV	TPV
Model	lin	lin	sin
Period [days]	-	-	19.1 ± 0.5
Amplitude [ppt]	-	-	0.15 ± 0.02
Phase	-	-	-0.08 ± 0.02
FAP	-	-	4.4e-10

and thus, a dissipation factor of $Q'_\star = 10^7$ is in agreement with the (current) observation. The non-detection supports again the results found by Csizmadia et al. (2019).

In summary, all the available light curves are re-analyzed for TOI-193.01 and WASP-18b. The main result is that in contrast to Pearson (2019), no evidence for TTVs in those systems could be found due to the small number of transits. The overall estimation of transit times and the shape of the TTVs agree with the results from Pearson (2019), but the automated conclusion made by the code is the opposite. To further characterize the long-term evolution of the systems, and to constrain the internal structure, more observations are needed, in particular with smaller uncertainties than obtained from the *TESS* observations.

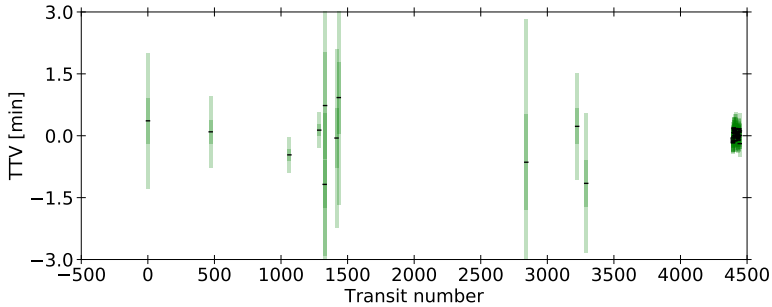

Figure 4.17.: Long-term TTVs of WASP-18b using the published transit times reported in Shporer et al. (2019) and the *TESS* transit estimates from `PyTTV`. No trend is found by `PyTTV` combining the available transit observations, in agreement with the results from Shporer et al. (2019).

Conclusions The analyses presented in this section verifies that `PyTTV` functions efficiently and accurately. This places it between the leading codes for TTV estimation. It is furthermore capable to search for variations in transit durations and transit depths. The transit modeling and search for variations is carried out entirely automatically. `PyTTV` can search for variations in light curves observed in different cadences, and from different telescopes putting it in an excellent position for the search of transit variations using upcoming and current facilities with its high flexibility.

4.4. New TTV systems with PyTTV

The following subsections present novel work where `PyTTV` was used to analyze systems using very recent data. The results from these analyses have been reported in publications either explicitly mentioning the results

or just for checking, e.g., if the assumptions for non-interacting planets are valid. Some results are presented here for the first time.

More precisely, the results for the systems TOI-1130, TOI-1136 and WASP-126 using all the available *TESS* light curves are reported for the first time, and Kepler-448b, HAT-P-7b, and Kepler-13Ab are searched for variations using *Kepler* and *TESS* light curves combined for the first time.

4.4.1. Non Detection of TTVs

K2-180b is a sub-Neptune-sized planet transiting its K2V host star every 8.9 days. It was observed in Campaign 5 by *K2*, first reported by Pope et al. (2016) as a candidate, and validated by Mayo et al. (2018) without mass determination. It was characterized by Korth et al. (2019) combining the *K2* photometry from Campaign 5 and high-precision imaging and RV measurements suggesting a rocky composition ($5.6 \pm 1.9\,\mathrm{g\,cm^{-3}}$). They estimated a planetary radius of $R_\mathrm{p} = 2.2 \pm 0.1\,\mathrm{R_\oplus}$, which puts K2-180b slightly above the so-called "planetary radius gap" (Fulton et al., 2017; Van Eylen et al., 2018; Fulton & Petigura, 2018). It has been suggested that the radius-period distribution is sculpted by photoevaporation (Owen & Wu, 2013; Lopez & Fortney, 2013; Owen & Wu, 2017; Jin & Mordasini, 2018). Thus, the planets are divided into two groups: the ones that have lost their primordial atmosphere (with a peak at $1.3\,\mathrm{R_\oplus}$) and the ones with inflated radii due to existing of a hydrogen-rich atmosphere (peak at $2.5\,\mathrm{R_\oplus}$). According to this, Korth et al. (2019) concluded that K2-180b is likely to have a gaseous envelope.

The results from the TTV search in K2-180b using `PyTTV` were presented in Korth et al. (2019); no evidence for TTVs was found in the data from Campaign 5. *K2* re-observed K2-180b in its Campaign 18. There-

Table 4.6.: Diagnostics of K2-180b. The value ϕ is reported as normalized phase with values [0,1], allowing for negative values. No variations were detected.

K2-180b: 8.86566 ± 0.00002 days			
	TTV	TDV	TPV
Model	lin	con	con

fore, the system was re-analyzed to take the additional transits into account. The conclusion stays the same, no signs of TTVs are detected neither periodic nor a trend. This agrees also with the RV measurements that show no evidence for an additional planet in the system. The diagnostics are summarized in Table 4.6 and the TTVs are shown in Fig. 4.18. The transit with the number 129 was discarded from the analysis because it was affected by an outlier point not detected by the *Kepler* or the `EVEREST` pipeline. The ΔBIC cannot distinguish between the linear and the sinusoidal model, and the simpler model is chosen by default. A detailed look at the `GLS` reveals that the linear model is favored because the detected periodicity is a harmonic of the orbital period and the FAP (0.04) for the sinusoidal model is too high. Because of the long data gap between Campaign 5 and Campaign 18, there are not enough points to make a robust estimate for a sinusoidal model. This highlights the importance of combining different statistical diagnostics as implemented in `PyTTV`, and that long data gaps prevent a periodic TTV estimation. However, a long-term trend caused by an additional companion or by orbit precession can still be revealed in the transit times.

K2-140b is a hot Jupiter orbiting its G6V host star in a 6.6 day orbit. It was observed in *K2* Campaign 10, validated independently by Livingston

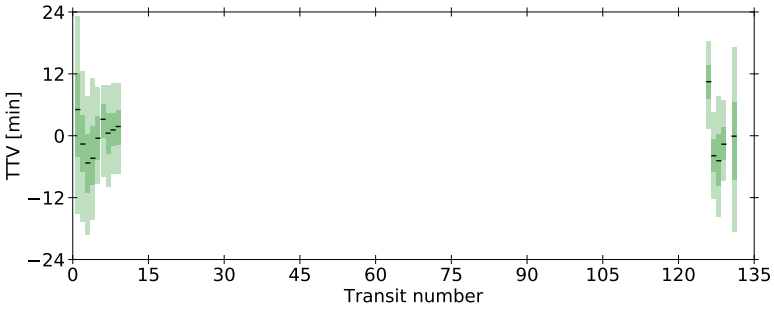

Figure 4.18.: TTVs of K2-180b. No significant TTVs were detected combining the transits from Campaign 5 and 18. The long data gap between both Campaigns prevents a reliable search for variations.

et al. (2018) and Mayo et al. (2018), and characterized independently by Giles et al. (2018) and Korth et al. (2019). Both Giles et al. (2018) and Korth et al. (2019) included high-precision RV measurements and photometry from *K2*, but concluded in disagreeing orbital eccentricity estimates. The discrepancy in the orbital eccentricity was recently studied by Espinoza et al. (2019); concluding that both models are statistically indistinguishable. Their deduction that the circular model seems to be more likely the best model based on the current data is in agreement with the results from Korth et al. (2019). The non-detection of TTVs was presented in Korth et al. (2019), and supports the circular solution; there are no additional planets that might excite the eccentricity of K2-140b. The diagnostics are listed in Table 4.7.

K2-100b is a young transiting planet orbiting its G0V host star on a 1.7 days circular orbit. RV measurements with HARPS-N were carried out, leading to the first mass measurement of a transiting planet in a young

Table 4.7.: Diagnostics for K2-140b. The value for ϕ is reported as normalized phase with values [0,1], allowing for negative values. No variations were detected.

K2-140b: 6.56917 ± 0.00005 days			
	TTV	TDV	TPV
Model	lin	con	con

Table 4.8.: Diagnostics for K2-100b. The value for ϕ is reported as normalized phase with values [0,1], allowing for negative values. No variations were detected.

K2-100b: 1.6739056 ± 0.0000008 days			
	TTV	TDV	TPV
Model	lin	con	con

open cluster (Barragán et al., 2019). They estimated a planetary density of $2.04^{+0.66}_{-0.61}$ g cm^{-3}, indicating that K2-100b has a significant volatile envelope that is evaporating due to the high irradiation received by the planet. The non-detection of TTVs in the transits from Campaigns 5 and 18 of the *K2* mission combined with a ground-based transit observation (see Table 4.8) were presented in Barragán et al. (2019). The non-detection of TTVs and thus a constant orbital period simplifies further follow-up observations.

The multi-planet system K2-106 consists of a USP planet, Kepler-106b, with an orbital period of 0.57 days, and an outer planet K2-106c, with an orbital period of 13.3 days (Guenther et al., 2017). The conclusion by Guenther et al. (2017) that the USP planet has an iron core containing 80^{+20}_{-30} % of its mass was recently disproven by Dai et al. (2019), who estimated a fraction of 40 ± 23 % that agrees within 1σ with the es-

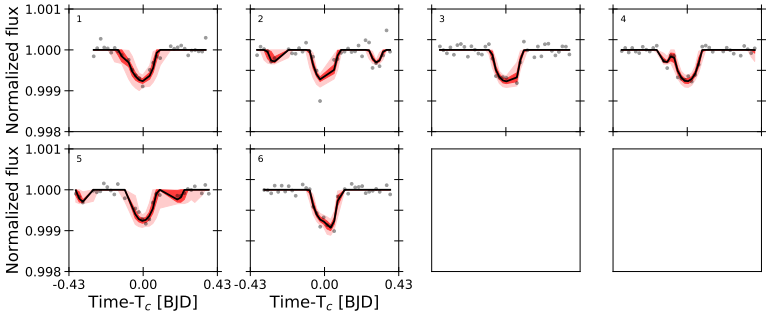

Figure 4.19.: Simultaneous transit modeling of Kepler-106. The deeper transits belong to K2-106c. Note the close and overlapping transits with the USP K2-106b. These overlapping transits complicated a reliable estimation of the variations.

timated fraction of 35 % from Sinukoff et al. (2017a). The non-detection of TTVs in the multi-system K2-106 was included in the analysis from Guenther et al. (2017) and verified by Dai et al. (2019). TTVs were also not likely because the two planets are quite distant for showing detectable TTVs. Nevertheless, there could have been TTVs induced by a (grazing) additional planet forming a typical *Kepler* multi-planet system. `PyTTV` detected a sinusoidal model for the TTVs according to the ΔBIC but the FAP was too high for a significant detection of TTVs. However, `PyTTV` detects TDVs for Kepler-106b as significant (Table 4.9). This is not a real signal, but instead produced by the combination of low S/N and long observing cadence. The individual transits do not have a high-enough S/N ratio for a robust detection of TTVs, TDVs or TPVs. In addition, the UPS planet Kepler-106b transits its host every 0.57 days, and, together with the co-planarity of both planets, often occurring overlapping transits lead to outliers (Fig. 4.19).

Table 4.9.: Diagnostics of the K2-106 system. The values for ϕ are reported as normalized phase with values [0,1], allowing for negative values. Only TDVs for K2-106b are found to be significant by FAP.

K2-106b: 0.57129 ± 0.00003 days			
	TTV	TDV	TPV
Model	sin	sin	con
Period [days]	1.160 ± 0.004	28.0 ± 1.1	-
Amplitude [min]	8.1 ± 1.9	17.7 ± 2.5	-
Phase	-0.47 ± 0.04	-0.18 ± 0.02	-
FAP	0.02	2.3e-06	-
K2-106c: 13.347 ± 0.003 days			
	TTV	TDV	TPV
Model	quad	sin	sin
Period [days]	-	44.5 ± 0.9	60.7 ± 10.7
Amplitude [min, ppt]	-	57.1 ± 2.5	0.19 ± 0.06
Phase	-	-0.449 ± 0.007	-0.01 ± 0.05
FAP	-	0.006	0.5

TOI-263 is a transiting sub-stellar object orbiting its M3.5 V host star on a 0.56 day orbit validated by multi color photometry (Parviainen et al., 2020). The nature of the object could not be clearly resolved because of the faintness of the host star; it can be either a giant planet or a brown dwarf. No TTVs were detected in the system. The ΔBIC favors indeed a sinusoidal model but the high FAP of the signal negated the detection (Table 4.10). The non-detection of TTVs found by `PyTTV` was presented in Parviainen et al. (2020). In addition, TTVs were not expected because the low S/N of the individual transits complicated accurate estimation of the transit centers. This neglects also the TPVs detected by `PyTTV` (see Table 4.10). Therefore, further follow-up observations are needed to clarify

its status.

Table 4.10.: Diagnostics of TOI-263.01. The value for ϕ is reported as normalized phase with values [0,1], allowing for negative values. Variations in the transit depths were detected but because of the low S/N ratio, further observations are needed to verify these variations.

TOI-263.01: 0.5572 ± 0.0003 days			
	TTV	TDV	TPV
Model	sin	con	sin
Period [days]	2.5 ± 0.1	-	8.0 ± 0.4
Amplitude [min, ppt]	14.7 ± 8.8	-	8.8 ± 1.4
Phase	-0.49 ± 0.06	-	0.47 ± 0.03
FAP	0.4	-	6.3e-05

TOI-1130 is a candidate multi-planet system discovered by *TESS* in Sector 13 containing a Neptune-sized and a Jupiter-sized planet. The planet candidates are expected to have strong TTVs because their orbital periods of 4.07 days and 8.35 days are close to a 2:1 period commensurability. Unfortunately, one Sector of *TESS* observations is not sufficient to detect TTVs and a constant period is favored (see Table 4.11). Nevertheless, this system is highly interesting because of its architecture; a smaller inner planet and an outer giant planet, and deserves more follow-up.

TOI-1136 is a candidate compact multi-planet system discovered by *TESS* in Sectors 14 and 15. The planet candidates have orbital periods of 6.3, 12.5, 18.8, and 26.3 days. Unfortunately, the *TESS* observations do not cover enough transits to detect significant variations (Table 4.12).[15]

[15] `PyTTV` calculates the GLS periodogram only for planets with more than two transits. Therefore no values are values reported in Table 4.12 for TOI-1136.03 and TOI-1136.04.

Table 4.11.: Diagnostics of the TOI-1130 system. No variations were detected.

TOI-1130.01: 4.067 ± 0.001 days			
	TTV	TDV	TPV
Model	lin	con	con
TOI-1130.02: 8.3510 ± 0.0007 days			
	TTV	TDV	TPV
Model	lin	con	con

Table 4.12.: Diagnostics of the TOI-1136 system. The two outermost candidates show only two transits in the light curve and are therefore not searched for periodicities. No variations were detected.

TOI-1136.01: 6.2573 ± 0.0006 days			
	TTV	TDV	TPV
Model	lin	con	con
TOI-1136.02: 12.5183 ± 0.0001 days			
	TTV	TDV	TPV
Model	lin	con	con

Small variations are visible in the TTVs (Fig. 4.20) but more observations are needed to make robust estimates. Fortunately, the system will be re-observed by *TESS* in Sectors 21 and 22.

WASP-126b is a very-low density hot Jupiter transiting its G2 host star every 3.28 days (Maxted et al., 2016). Pearson (2019) reported significant TTVs produced by a non-transiting planet (see Sect. 4.3) using two Sectors from *TESS*. Here, 13 Sectors of *TESS* light curves are used to search for variations. The TTVs for WASP-126b are shown in Fig. 4.21. No sig-

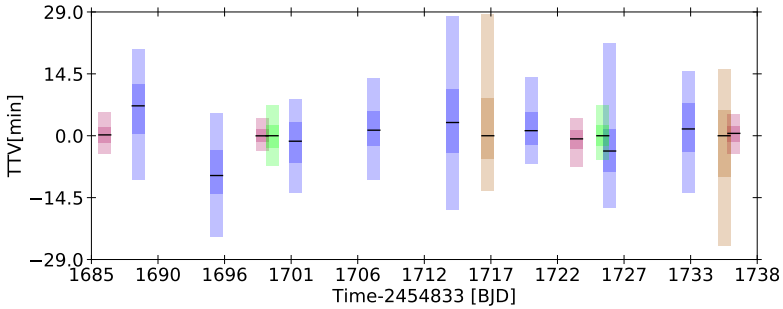

Figure 4.20.: TTVs of the four-planet candidates in the TOI-1136 system. The individual planets are color-coded as TOI-1136.01 in blue, TOI-1136.02 in red, TOI-1136.03 in green, and TOI-1136.04 in brown. Unfortunately, the TESS observations do not cover enough transits to detect significant variations, but a tentative trend is visible. The system will be re-observed by TESS in Sectors 21 and 22.

nificant variations were detected (Table 4.13) and therefore there is no hint for an additional planet. These results contradict the reported additional planet by Pearson (2019).

4.4.2. Detection of TTVs

K2-146 is an M-dwarf hosting two planets with periods close to a 2:1 period commensurability ($P_b = 2.67$ days and $P_c = 3.97$ days). The inner

Table 4.13.: Diagnostics of WASP-126b. No variations were detected.

WASP-126b: 3.288786 ± 0.000002 days			
	TTV	TDV	TPV
Model	lin	con	con

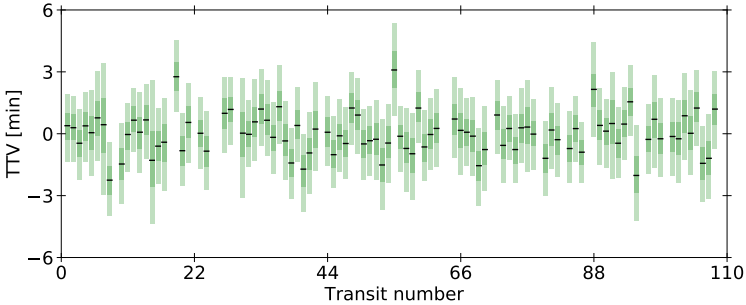

Figure 4.21.: TTVs of the WASP-126b using 13 Sectors of *TESS* light curves. No variations were detected.

planet, K2-146b, was first reported in Pope et al. (2016) as a planet candidate in the *K2* Campaign 5. The TTVs of K2-146b were detected by Hirano et al. (2018) exhibiting an amplitude of around 30 minutes indicating the presence of a perturbing object. At this time no other planet was detected in the light curve of Campaign 5. Lam et al. (2020) detected K2-146c in the system using the additional Campaigns 16 and 18 from *K2*. K2-146c has an extremely grazing transit whereby it was not transiting in the previous Campaign 5, indicating a strong dynamical interaction between K2-146b ad K2-146c. Strong anti-correlated TTVs were detected by `PyTTV` and presented in Lam et al. (2020)[16]. The TTVs are shown in Fig. 4.22, indicating that the planets are gravitationally interacting and orbiting the same star. The transit times estimated by `PyTTV` were used for the analysis with `TTVFast` to estimate the physical quantities. The analysis revealed masses and eccentricities of $M_{\rm p} = 5.6 \pm 0.7\,{\rm M}_{\oplus}$ and $e = 0.14 \pm 0.07$ and $M_{\rm p} = 7.1 \pm 0.9\,{\rm M}_{\oplus}$ and $e = 0.16 \pm 0.07$ for K2-146b

[16] A previous version of `PyTTV` was used.

and K2-146c, respectively. The detected TTV periodicities for each planet reported in Table 4.14 by `PyTTV` agree within 3σ with each other, as expected for anti-correlated TTVs. The anti-correlation is also notable in the phase values that differ by around 0.5. Lam et al. (2020) also found that this system is likely trapped in the 3:2 mean motion resonance. The grazing transit configuration of K2-146c during the observation time span from *K2* goes along with a changing impact parameter indicating precession of the orbital plane. As mentioned in Miralda-Escude (2002), the orbital precession leads to changes in the transit durations. The transit durations and transit depths are constant for both planets (Table 4.14). For K2-146c the light curves from Campaign 5 were not considered in the analysis because of the grazing configuration and a poor S/N. Further observations of this system and a detailed study using both TTVs and TDVs is therefore highly recommended. In an independent study, Hamann et al. (2019) analyzed also K2-146 via a dynamical fit and came to the same conclusion as presented in Lam et al. (2020).

Kepler-448 Kepler-448b is another warm Jupiter in an eccentric orbit that has a non-transiting eccentric sub-stellar companion detected and characterized through dynamical modeling of the TTVs and TDVs (Masuda, 2017). Like the TTVs for Kepler-693, the TTVs for Kepler-448 show a "bump" (see Masuda (2017) and Fig. 4.23).

Kepler-448b was first identified as a planetary candidate by Borucki et al. (2011b). Rowe et al. (2015) detected the TTVs, and Bourrier et al. (2015) characterized the system using the *Kepler* photometry, Doppler spectroscopy, and line-profile tomography obtained with the SOPHIE spectrograph. Kane et al. (2019) and Gajdoš et al. (2019) detected significant variations neither in the transit centers nor in the durations or depths. Hol-

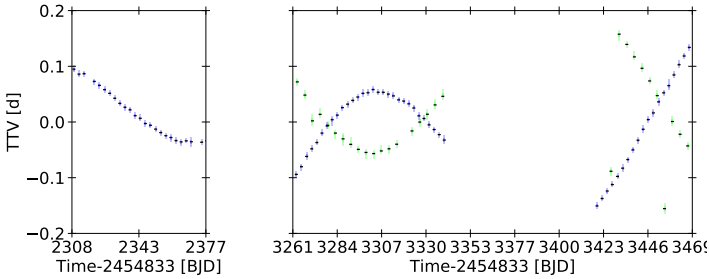

Figure 4.22.: TTVs of K2-146b in Campaign 5 (left panel); K2-146c has a grazing transit in this Campaign preventing a secure detection. TTVs of K2-146b in blue and K2-146c in green in Campaign 16 and 18 (right panel). The bars mark the 3σ uncertainties. The anti-correlated TTVs in the Campaigns 16 and 18 are clearly visible.

czer et al. (2016) detected a significant long-term trend in the TTVs but detected no significant TDVs and TPVs. In contrast to the TTVs derived with `PyTTV` and by Masuda (2017), the TTVs from Holczer et al. (2016) do not show a strong "bump" in the TTVs (Fig. 4.4.2).

The system was observed by *TESS* in Sectors 14 and 15. The TTV analysis combining the *Kepler* and *TESS* light curves are presented here using `PyTTV` for the first time. Unfortunately, *TESS* observed only one and a half transits of Kepler-448b because most transits were falling into the observation gaps occurring during the on-board data download (every 13.7 days, once per orbit).[17]

The variations in the parameters are shown in Fig. 4.23. They show the same trend as in Masuda (2017), in particular for the TTVs and TDVs. The detected periodicities are summarized in Table 4.15; the variations in the

[17] The partial transit was not considered by `PyTTV`.

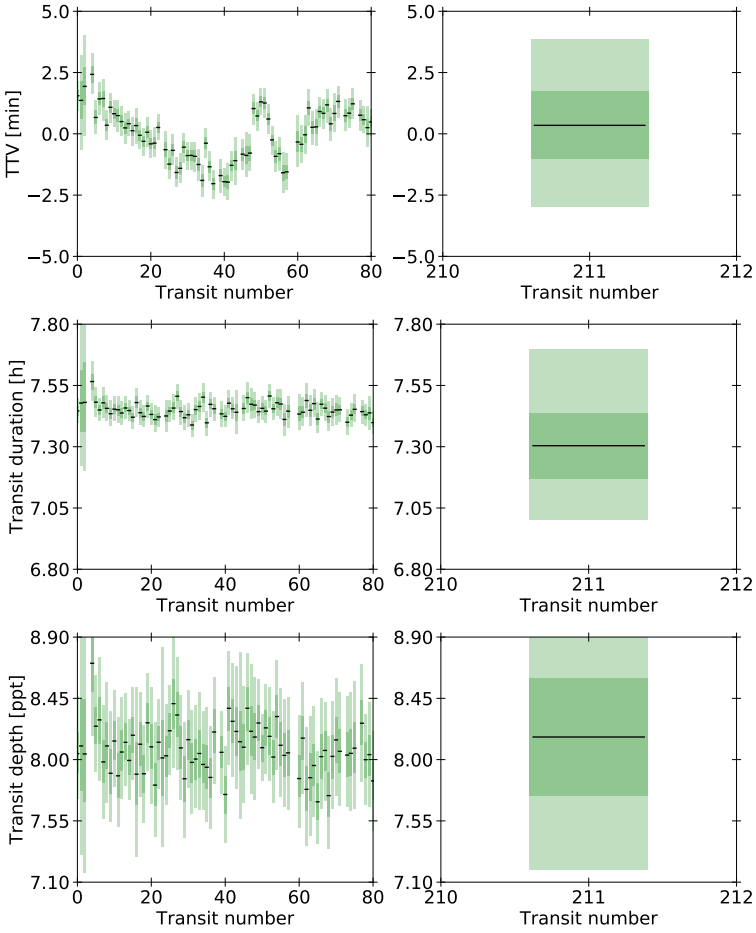

Figure 4.23.: TTVs (top panel), transit durations (middle panel), and transit depths (lower panel) of Kepler-448b. The panels on the left show the variations estimated from the *Kepler* photometry. The panels on the right display the one estimate from the *TESS* light curve. Note that the "bump" in the TTVs from the *Kepler* light curves is reproduced.

Table 4.14.: Diagnostics of the K2-146 system. The values for ϕ are reported as normalized phase with values [0,1], allowing for negative values.

K2-146b: 2.65044 ± 0.00006 days			
	TTV	TDV	TPV
Model	sin	con	con
Period [days]	157.4 ± 1.7	-	-
Amplitude [min]	222.4 ± 4.8	-	-
Phase	-0.049 ± 0.003	-	-
FAP	8.5e-27	-	-
K2-146c: 3.9889 ± 0.0007 days			
	TTV	TDV	TPV
Model	sin	con	con
Period [days]	169.4 ± 2.5	-	-
Amplitude [min]	233.7 ± 6.2	-	-
Phase	-0.494 ± 0.004	-	-
FAP	2.2e-12	-	-

transit centers are estimated as significant, while no variations in the transit durations were found. The shorter transit duration derived from the *TESS* light curves is not detected as significant and needs more data to be verified. The uncertainties of all the parameters estimated for the *TESS* light curve are comparable to the uncertainties estimated for the long cadence *Kepler* photometry or are even larger. The *TESS* telescope is smaller compared to the *Kepler* telescope, which explains the increased uncertainties, leading to lower photometric quality for the same target.

HAT-P-7b/Kepler-2b is a hot Jupiter that orbits its F6 host star with an orbital period of 2.2 days (Pál et al., 2008). The planet has been studied extensively focusing on different topics, such as the gravity-darkening effect

Table 4.15.: Diagnostics of Kepler-448b. The value for ϕ is reported as normalized phase with values [0,1], allowing for negative values. The variations in the transit times are found to be significant.

Kepler-448b: 17.855229 ± 0.000003 days			
	TTV	TDV	TPV
Model	sin	sin	con
Period [days]	1255.8 ± 95.1	941.9 ± 136.6	-
Amplitude [min]	1.1 ± 0.1	0.9 ± 0.2	-
Phase	0.266 ± 0.01	0.27 ± 0.04	-
FAP	5.7e-17	0.1	-

(Masuda, 2015), obliquity measurements via the Rossiter-McLaughlin effect (Winn et al., 2009; Narita et al., 2009; Albrecht et al., 2012) or the transit chord correlation (Dai et al., 2018), secondary eclipse measurements (Angerhausen et al., 2015), and ellipsoidal variations (Borucki et al., 2009; Welsh et al., 2010; Esteves et al., 2013; Faigler et al., 2013). HAT-P-7b shows an anomaly in its transit shape that was first attributed to spots by Morris et al. (2013), but with more data it became clear that the anomaly is constant in time as shown in Fig. 8 of Masuda (2015),[18] negated the spot scenario. Winn et al. (2009) found evidence for an additional companion with an orbital period longer than two years. Narita et al. (2012) verified this companion and found an additional stellar companion. They derived from the trend attributed to the second companion its mass constraints as $M_{\rm c} \sin i_{\rm c}/a_{\rm c}^2 \sim 0.12 \pm 0.01\,{\rm M_{Jup}\,AU^{-2}}$. Assuming that the orbital period of the second companion is longer than ten years, they predict that it is more massive than Jupiter.

[18] Previous detections are reported in Van Eylen et al. (2013) and Benomar et al. (2014).

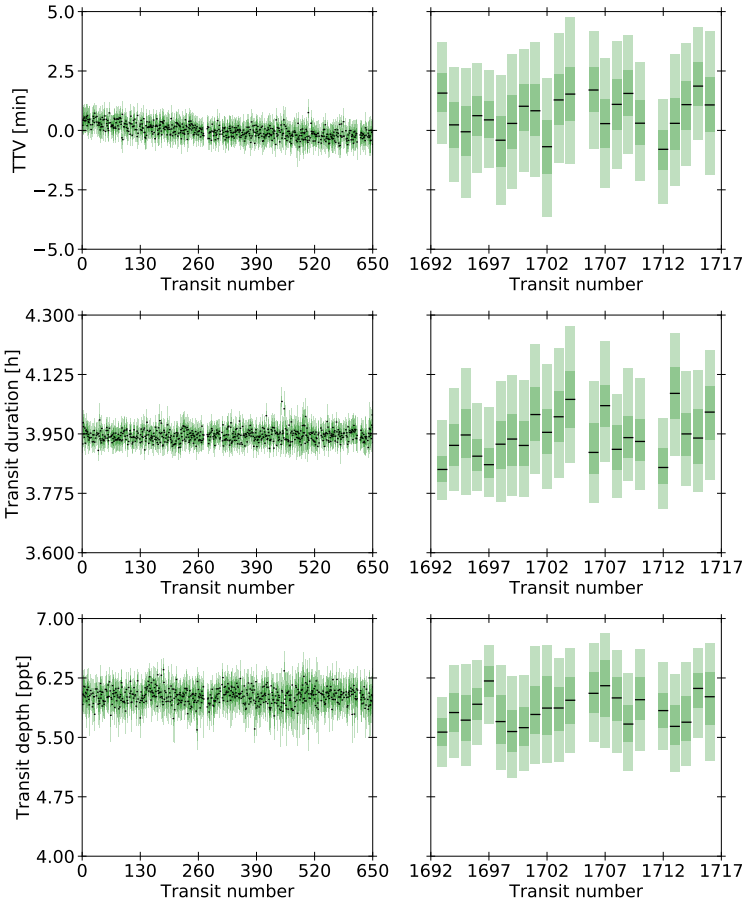

Figure 4.24.: TTVs (top panel), transit durations (middle panel), and transit depths (lower panel) of HAT-P-7b. The panels on the left show the variations estimated from the *Kepler* photometry. The panels on the right display the variations estimated from the *TESS* light curve. The tentative quadratic trend in the TTVs determined from the *Kepler* data is detectable. Note that the uncertainties for the *TESS* data are several times larger than the uncertainties derived for the short cadence *Kepler* light curves.

Zhu et al. (2014) studied the oblateness of Kepler planets and estimated HAT-P-b's oblateness to be lower than 0.067, supporting that this planet is tidally locked. They also estimated that the signatures for spin-orbit synchronization and rotational oblateness will not be detectable using Q' values from Jupiter and Saturn.

Szabó et al. (2013) detected TTVs in HAT-P-7b and attributed them to the stroboscopic effect. In contrast, Benomar et al. (2014) found no evidence for TTVs. Van Eylen et al. (2013) analyzed the transit depth of 16 Quarters from the *Kepler* mission and found systematic variations (1%) from quarter to quarter with an annual periodicity. They suggested erroneously estimated field crowding or instrumental artifacts as possible explanations. They highlighted the importance of taking these effects into account when transits observed in different quarters are combined. They mention that ignoring these effects would lead to underestimated errors and measurements of the radius ratio with a precision better than 1% would be unrealistic.

Because of the detected TPVs in Van Eylen et al. (2013), reported TTVs by Szabó et al. (2013), and a companion (Winn et al., 2009; Narita et al., 2012), the system is studied here in more detail. The HAT-P-7 system gives not only a chance to compare `PyTTV` with other approaches for the search for TTVs and TPVs, but also to combine the light curves of different space-based missions. HAT-P-7b was observed by the *Kepler* mission and the *TESS* mission in Sectors 14 and 15. Combining the *TESS* light curves with the *Kepler* light curves increases the observational time span to almost 4000 days of space-based observations, which enables the search for the orbital decay rate of 10 seconds after ten years, as suggested by Birkby et al. (2014) assuming $Q'_\star = 10^6$.

The TTVs, TDVs, and TPVs for HAT-P-7b are visualized in Fig. 4.24.

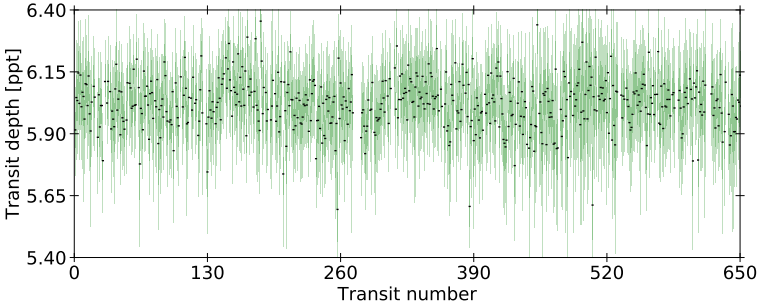

Figure 4.25.: TPVs of HAT-P-7b estimated from the *Kepler* light curve. The detected periodicity of $\sim$400 days $\approx$ 180 orbits (transit number) is slightly visible.

For a better comparison with the TPVs detected by Van Eylen et al. (2013), the TPVs are visualized in Fig. 4.25 only for the *Kepler* observations. The `GLS` periodogram detected a period of the depth variations of $\sim$400 days (Table 4.16), in agreement with the variations detected by Van Eylen et al. (2013). The depth variation is not considered as significant. The best model representing the TTVs is the quadratic trend indicating a long-term trend. This trend is not detected if only the *Kepler* photometry was searched for TTVs, which is in agreement with the previous studies by Benomar et al. (2014). The combination of the *Kepler* light curves with the *TESS* light curves revealed the variation in the transit center times. The fitted polynomial function is $(2454954.36000 \pm 0.00002) + (2.20473493 \pm 0.00000006) \times x + (7.7 \pm 0.4) \times 10^{-10} \times x^2$ epochs. The reason for the long-term trend cannot be determined until more data are acquired. A possible orbital decay as suggested by Birkby et al. (2014) and shown in Fig. 3.4 is ruled out by the sign of the quadratic term. Dynamical forward modeling with `PyTTV` of the system with an outer companion (HAT-P-7c;

Table 4.16.: Diagnostics of HAT-P-7b. The value for ϕ is reported as normalized phase with values [0,1], allowing for negative values. No significant variations are detected besides a long term trend in the transit centers.

HAT-P-7b: $2.20473612 \pm 0.00000003$ days			
	TTV	TDV	TPV
Model	quad	sin	sin
Period [days]	-	6.37 ± 0.01	406.6 ± 17.1
Amplitude [min, ppt]	-	0.5 ± 0.3	0.04 ± 0.01
Phase	-	-0.5 ± 0.1	0.40 ± 0.05
FAP	-	1.0	0.9

Knutson et al., 2014; Winn et al., 2009; Narita et al., 2012) offers solutions that can explain the trend, but the parameter space is not well-constrained by the current TTV data. Since the orbit is most likely tidally locked, the eccentricity is zero, and changes in the transit times caused by periastron precession can be excluded. More observations are required to determine the true physical cause for the TTVs.

Kepler-13Ab is a massive planet orbiting an optical A-type binary with a period of 1.76 days that was detected by Borucki et al. (2011b). It is the first transiting system where light curve distortions caused by gravity-darkening produced by rapid stellar rotation were detected (e.g. Szabó et al., 2011; Barnes et al., 2011). In addition, it was the first system for which stellar obliquity was measured via the gravity darkened transit light curve without measuring the Rossiter-McLaughlin effect spectroscopically (Szabó et al., 2011). The light curve shows out-of-transit modulations by the ellipsoidal and beaming effect that lead to the first mass estimates via photometry (e.g. Shporer et al., 2011; Mazeh et al., 2012;

Mislis & Hodgkin, 2012). Szabó et al. (2012) derived a stellar rotation period of 25.42 ± 0.05 hours that is probably in 5:3 resonance with the orbital period and was the first measurement of a spin-orbit resonance. Johnson et al. (2014) carried out Doppler tomography to independently validate the hot Jupiter as a planet and to measure the spin-orbit alignment that contradicts with previously reported values by Barnes et al. (2011) using the gravity-darkening method. Masuda (2015) used also the gravity-darkening method from Barnes et al. (2011) to measure both components of the spin-orbit angle. They solved the discrepancy between the values derived by Barnes et al. (2011) and Johnson et al. (2014) by fitting quadratic limb-darkening law.

Long-term variations in the transit duration were detected to be most likely caused by spin-orbit precession induced by stellar quadrupole moment of the host star (Szabó et al., 2012, 2014). Szabó et al. (2012) detected in the short cadence light curves from Q2 ad Q3 variations in the transit duration of $1.14 \pm 0.30 \times 10^{-6}$ days cycle^{-1} and proposed a changing impact parameter with a rate of -0.016 ± 0.004 year^{-1} as a reason for the variation. They noted that this change is one order of magnitude smaller than the precision determined from fitting the transit shape and therefore the stellar oblateness is negligible when converting transit duration to impact parameter. Furthermore, they showed that the change in the impact parameter is most likely caused by secular perturbation due to the stellar oblateness of a fast rotator. They determined from this variation a stellar quadrupole moment of $J_2 = (2.1 \pm 0.6) \times 10^{-4}$ that is in agreement with the theoretical estimate of $J_2 = 1.7 \times 10^{-5}$. Szabó et al. (2012) did not detect TTVs and ruled out short-term secular variations in the semi-major axis. They mention a drawback of their fitting; they were fitting a symmetrical model to the transits that are known to be asymmetric. Nev-

ertheless, they conclude that the variations are an artifact because: the asymmetry has no time-depend variation, the uncertainties reflect the ambiguities, and it is unrealistic that only the transit durations are affected by the asymmetry. Szabó et al. (2014) took the *Kepler* light curves up to Quarter 14 and repeated the analysis from Szabó et al. (2012) to look for variations in transit depths, durations, and shapes. They found that these parameters change slowly as the transit moves across the stellar disc, leading to the mapping of the stellar surface within several decades. They found a variation in the peak transit depth that is reported to be caused by the orbital precession. Their fitted polynomial function[19] to the transit durations is $2.889 + 2.21 \times 10^{-5}$ x.

Masuda (2015) also measured the variations in the orbital inclination ($(7.0 \pm 0.4) \times 10^{-6}$ days^{-1}) and constrained $J_2 = (6.1 \pm 0.3) \times 10^{-5}$ with their gravity darkening model. They also estimated a rate for J_2 form the light curve ($J_2 = (1.66 \pm 0.08) \times 10^{-4}$) that is in agreement with the solution from Szabó et al. (2012). Their results predict detectable variations in λ after ten years estimated from the light curve, while λ should stay constant for the gravity-darkening model. Future observations might help to distinguish between both models and might constrain J_2 better. Herman et al. (2018) used also a gravity-darkening model to analyze Kepler-13Ab. They verify the changing impact parameter with a rate of $(4.1 \pm 0.2) \times 10^{-5}$ days^{-1} from the light curve and $(3.2 \pm 1.3) \times 10^{-5}$ days^{-1} from the secondary eclipse. In addition, they found that 1% of light dilution is enough to explain the seasonal variation in the depth as already mentioned in Van Eylen et al. (2013). They also detected a tentative change in the transit center times of $(1.7 \pm 0.1) \times 10^{-2}$ days^{-1} that they related to their fixed orbital period.

[19] The equation is corrected here to 10^{-5} instead of 10^{5} written in the paper.

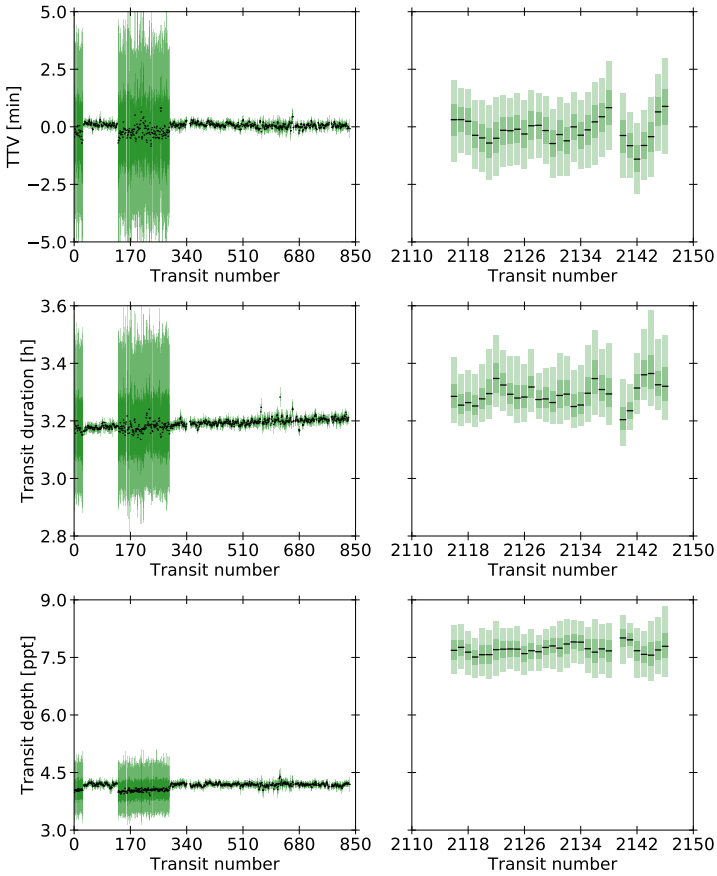

Figure 4.26.: TTVs (top panel), transit durations (middle panel), and transit depths (lower panel) of Kepler-13Ab. The panels on the left show the variations estimated from the *Kepler* photometry. The panels on the right display the variations estimated from the *TESS* light curve. A trend in the TDVs and TPVs is detectable. The large difference in the TPVs is because of different crowding correction. Note that the uncertainties for the *TESS* data are several times larger than the uncertainties derived for the short cadence *Kepler* light curves.

Here, the *Kepler* light curves up to Quarter 17 are analyzed together with the *TESS* light curves from Sector 14 and 15 (Fig. 4.26). The large differences in the transit depths are caused by different contamination estimates removed by the PDC pipeline. While in the *Kepler* Input Catalog one source was listed and corrected, the *TESS* Input Catalog lists and corrects contamination from three sources. Therefore, the detected quadratic trend (see Table 4.17) in the transit depths is produced by this different contamination.

The crowding correction could be adjusted if its true value would be known. This correction involves modeling the individual Point Spread Functions from *Kepler* and *TESS* in addition to the correct combination of contaminating sources. This detailed treatment is beyond the scope of the thesis. Nevertheless, the current analysis includes a study of the contamination effect on the derived transit center times and durations. Contamination was shown not to affect transit center times, and even strong contamination was shown to change the transit durations by only 10-15 seconds. The accuracies with which the transit durations are measured are around 20 seconds and 380 seconds for short and long cadence data, respectively. Therefore, the effect on the transit durations from contamination is within the uncertainties. The change in the transit duration from *Kepler* and *TESS* is in addition in order of minutes (Fig. 4.24 lower panel).

The best model representing the variations in the transit durations is a quadratic polynomial ($(3.172 \pm 0.001) + (4.0 \pm 0.3) \times 10^{-5}$ x + $(7.3 \pm 1.4) \times 10^{-9}$ x^2) hours, where x is given in epochs. The quadratic term is significant over the time span of ten years. The average change in transit duration over ten years is 0.0113 ± 0.0009 hours year^{-1} which leads to a change in the impact parameter of -0.020 ± 0.002. This value is about twice the change reported by Szabó et al. (2020). The difference can be

attributed to the simplified transit model that does not take into account stellar oblateness and gravity-darkening, which both have a major effect in the case of Kepler-13Ab. Even though here a symmetric transit model with limb-darkening is fitted and therefore the gravity-darkening effects are neglected, variations are detected in the transit durations and transit depths. The detected sinusoidal variation in the transit times is also attributed to the gravity darkening and the changes in the transit shape since Szabó et al. (2020) accounted for this in their analysis and no TTVs were detected. No constant parabolic variations in the transit times produced by orbital decay have been detected. A transit shift of around 40 seconds has been suggested assuming a $Q'_\star = 10^6$ (Fig. 3.4). The non-detection of a transit shift with this magnitude indicates that the stellar quadrupole moment is more likely to be larger ($Q'_\star = 10^7$). The transit shift assuming $Q'_\star = 10^7$ is under the detection limit of 5 seconds. Therefore, more observations are needed to clearly determine the stellar quadrupole moment.

Table 4.17.: Diagnostics of Kepler-13Ab. The value for ϕ is reported as normalized phase with values [0,1], allowing for negative values. Significant TTVs are detected as well as quadratic trends in the transit durations and depths.

Kepler-13Ab: $1.76358768 \pm 0.00000001$ days			
	TTV	TDV	TPV
Model	sin	quad	quad
Period [days]	1513.2 ± 127.1	-	-
Amplitude [min]	0.049 ± 0.004	-	-
Phase	-0.05 ± 0.01	-	-
FAP	6.9e-19	-	-

4.4.3. Conclusions

A publicly available open-source tool[20] `PyTTV` has been developed to automatically search for variations in transit times, durations, and depths. The development of `PyTTV` was necessary because the increasing amount of light curves impedes manual search. `PyTTV` can search for variations in light curves observed in different cadences, with different noise properties, and from different telescopes, putting it in an excellent position for the search of transit variations using current and upcoming facilities.

The analyses presented in this section verify that `PyTTV` functions efficiently and accurately. It can detect TTVs, TDVs, and TPVs in various kinds of systems. Multi-planet systems close to a first-order MMR (Kepler-9, and K2-146), with period ratios far from a period commensurability with an atypical periodicity (Kepler-117), with eccentric and inclined planets (Kepler-693, Kepler-448, and Kepler-88). But also the non-detection of variations helps to characterize the planetary systems, e.g., for K2-180, K2-140, K2-100, K2-106, TOI-263, TOI-1130, TOI-1136, WASP-126 and WASP-18. The combination of various transit observations enables the search for long-term disturbances in the light curves caused by orbital precession or orbital decay, as presented for WASP-18b, HAT-P-7b, and Kepler-13Ab.

The presented `PyTTV` analyses have either been reported in publications or contain novel work where `PyTTV` was used to analyze systems using very recent data for the first time. More precisely, the results for the systems TOI-1130, TOI-1136 and WASP-126 using all the available *TESS* light curves are reported for the first time, and Kepler-448b, HAT-P-7b, and Kepler-13Ab are searched for variations using *Kepler* and *TESS* light

[20] `https://github.com/JudithKorth/PyTTV`

curves combined for the first time.

The accuracy of transit times estimated by this method is comparable to other literature values and methods. Overall, the individual transit modeling estimates the transit times robustly, and reaches or exceeds the same accuracy as existing codes. This places it between the leading codes for TTV estimation.

5

PyTTV: Estimation of physical quantities

The physical quantities of the planets in a multi-planet system (transiting or not) can be inferred through the inversion of the TTV signal. The TTV signal depends on the physical quantities of the perturbing planets and the orbital architecture of the system, and is enhanced when the planets are in or near mean-motion resonances (e.g. Holman & Murray, 2005; Agol et al., 2005; Agol & Steffen, 2007; Veras et al., 2011; Lithwick et al., 2012; Nesvorný & Vokrouhlický, 2016; Hadden & Lithwick, 2016). This makes the TTV method ideal for the estimation of the physical quantities of low-mass planets that can not easily be determined by other methods.

The inversion can be solved analytically or numerically via the perturbation theory (Nesvorný & Morbidelli, 2008; Nesvorný, 2009; Nesvorný & Beaugé, 2010; Agol & Deck, 2016; Deck & Agol, 2015, 2016). These approaches simplify the problem and reduce it typically to first-or second-order in the orbital elements. Some analytical expressions have been derived for the case of two transiting perturbing planets (Agol et al., 2005; Linial et al., 2018), close to first-order resonances (Agol et al., 2005; Lithwick et al., 2012; Hadden & Lithwick, 2014; Nesvorný et al., 2014; Nesvorný & Vokrouhlický, 2016; Hadden & Lithwick, 2016; Deck & Agol,

2016), or second-order resonances (Hadden & Lithwick, 2016; Deck & Agol, 2016). Some numerical approaches based on n-body integration are found by Borsato et al. (2014), Deck et al. (2014), and Hadden & Lithwick (2016, 2017). Pearson (2019) combined n-body integration with machine learning for the parameter extraction. Since mutual inclinations are not influencing the TTV amplitudes strongly, most studies assume co-planarity (e.g. Lithwick et al., 2012; Nesvorný & Vokrouhlický, 2014; Jontof-Hutter et al., 2016; Hadden & Lithwick, 2016; Agol & Deck, 2016). Other studies use a photodynamical approach for the determination of the physical quantities (e.g. Cochran et al., 2011; Carter et al., 2012; Huber et al., 2013; Mills et al., 2016; Mills & Fabrycky, 2017b,a; Barros et al., 2015; Almenara et al., 2015, 2016, 2018a,b; Freudenthal et al., 2018, 2019). The advantage of a photodynamical model is that all the transits from all the planets in the system are modeled simultaneously. However, a photodynamical model is a very computationally expensive method for parameter estimation.

The currently publicly available codes have different capabilities. `TTVFast` (Deck et al., 2014) models TTVs and RVs using n-body integration, `TTVFaster` (Agol & Deck, 2016) is a purely analytical method for modeling TTVs, `Phodymm` (Mills et al., 2016) is a photodynamical model that models both photometry and RVs, `Trades` (Borsato et al., 2014) models TTVs and RVs, and `Nbody-AI` (Pearson, 2019) models TTVs. `TTVFast` and `TTVFaster` implement only the model, and the parameter estimation framework needs to be built around them. `Trades`, `Nbody-AI`, and `Phodymm` can be directly used for parameter estimation.

Since the TTVs are caused mainly by gravitational interactions between the objects in a system, all the codes take only the gravitational forces into account when inverting the TTV signal. A tool for fitting transit times,

transit durations, radial velocities together considering all the forces described in Sec. 3 was still lacking and is now implemented in `PyTTV`.

The estimation of the physical quantities using `PyTTV` is explained in the following. The parameter estimation is carried out afterwards for three systems that are modeled simultaneously with all available observations for the first time: Kepler-9, Kepler-289, and K2-146.

5.1. Parameter estimation

Estimation of the physical quantities from TTV observations requires a precise n-body analysis to model the planetary positions and velocities accurately. For this, a tool was developed to extract the physical quantities from TTVs, TDVs, and RVs. The code is written in Python and is hosted in a GitHub repository. The code uses the standard scientific Python libraries, `NumPy` (Van Der Walt et al., 2011), `SciPy` (Virtanen et al., 2020), `Matplotlib` (Hunter, 2007), `AstroPy` (Robitaille et al., 2013; Price-Whelan et al., 2018), `pandas` (McKinney, 2010), `seaborn` (Waskom et al., 2018), `xarray` (Hoyer & Hamman, 2017), and `IPython` (Pérez & Granger, 2007), and the open-source libraries `Forecaster` (Chen & Kipping, 2017), `TTVFaster` (Agol & Deck, 2016), `Rebound` (with IAS15 integrator; Rein & Liu, 2012; Rein & Spiegel, 2015), `Reboundx` (Tamayo et al., 2019), `emcee` (Foreman-Mackey et al., 2013), and `PyTransit` (Parviainen, 2015).

The physical quantities are estimated iteratively. First, the planet to star radius ratio $R_p/R_\star$ from the transit modeling is used together with the stellar radius estimate to derive the planet radius. The planet radius is then used to derive a prior on the planet mass using a probabilistic mass-radius relation offered by `Forecaster`. In an optional step, a

fast parameter estimation run is carried out with a TTV model calculated by `TTVFaster`. The final parameter estimation is carried out using `Rebound` and `Reboundx` to model all the observables without approximations. This final parameter estimation run is initialized either using uninformative priors or the posteriors from the optional fast parameter estimation.

5.1.1. Formalism

The N-body integration is carried out using `Rebound` that integrates the equation of motion considering the gravitational forces between the star and the planets. `PyTTV` is built in a modular way so that different configurations of forces can be turned on and off. General relativity, tidal interaction, and spherical harmonics can be added to the integration via `Reboundx`.

A common coordinate system was chosen where the x-y plane is the plane of sky (Fig. 5.1). The x-axis points to the East, the y-axis points to the North, and the z-axis points to the observer. Ω is measured from East to North, and ω is measured from the plane of sky. The simulation is carried out in barycentric coordinates.

The code models the TTVs, TDVs, and RVs together. The simulation starts from a given reference epoch (in which all the angles are defined) and integrates the system to the time of the first observation (either a transit or RV measurement). If the observation is a transit, a root-finding approach described in Fabrycky (2010) is used to find the time when the transiting planet is nearest to the star in the plane of sky (the transit center), the transit time is corrected for the light travel time (Fabrycky, 2010), and the projected velocity of the planet is used to estimate the transit du-

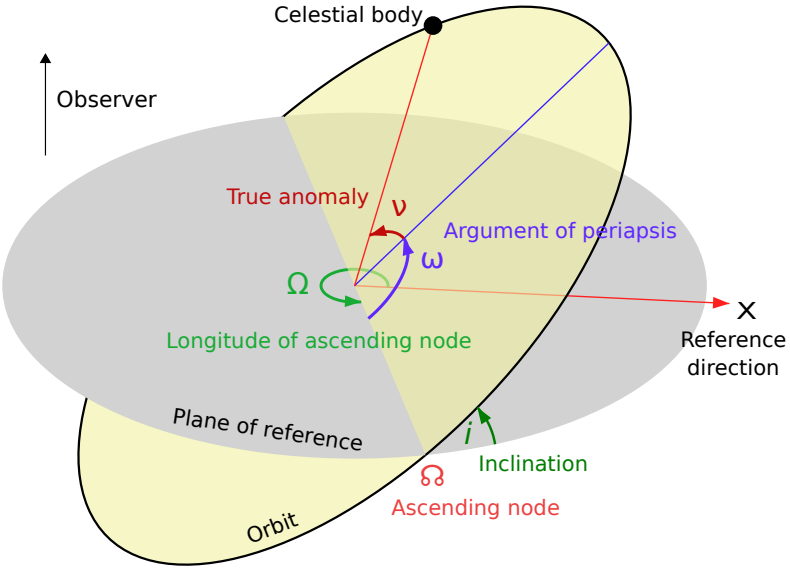

Figure 5.1.: Coordinate system of the simulation. The origin is the center of mass, and x-y is the reference plane. The x-axis is the reference direction and points to the East. The observer is located at positive z-axis. Modified after a figure by Lasunncty at the English Wikipedia, released under Attribution-Share Alike 3.0 Unported license.

ration. If the observation is an RV measurement, the system is integrated directly to the measurement time, and the stellar -z velocity is recorded as the RV value. The simulation is continued over all the measurements, and finishes with model values for all the measurements.

The estimation of physical quantities from the TTV signal is computationally challenging. First, the posterior mode is found using the Differential Evolution algorithm implemented in `PyTransit`. The optimization is carried out varying the planetary masses, orbital periods, eccentrici-

ties and arguments of periastron implemented via the parameters $\sqrt{e}\cos\omega$ and $\sqrt{e}\sin\omega$, inclination, and longitude of the ascending node. After the posterior mode is found, the posterior is sampled using MCMC sampler `emcee`.

5.1.2. Priors

The parameter posterior space of the TTV model can be ambiguous, that is, different orbital configurations can reproduce the observed TTVs within the uncertainties. Furthermore, some parameters are strongly correlated, e.g., planetary mass and orbital eccentricity (Lithwick et al., 2012; Deck & Agol, 2015). For a robust parameter determination, a priori information on the eccentricity is recommended if a "chopping" signal is not present in the TTVs. This a priori information can originate from RV measurements or from statistics (Xie et al., 2016; Van Eylen & Albrecht, 2015; Van Eylen et al., 2019; Kipping, 2013; Hadden & Lithwick, 2014).

Another ambiguity occurs when the perturbing planet is not transiting and no further harmonics are detected in the TTVs. In that case the different orbital periods and planetary mass combinations can lead to the same TTV signal.

Eccentricities use by default the β-distribution from Kipping (2013) as a prior. The distribution is informative but not overly constraining, and thus well-suited if there is a reason to believe that the eccentricities can be high (see Fig. 5.2). For compact multi-planet systems, where the eccentricities are usually low, a Rayleigh distribution presented by Van Eylen et al. (2019) can be used.

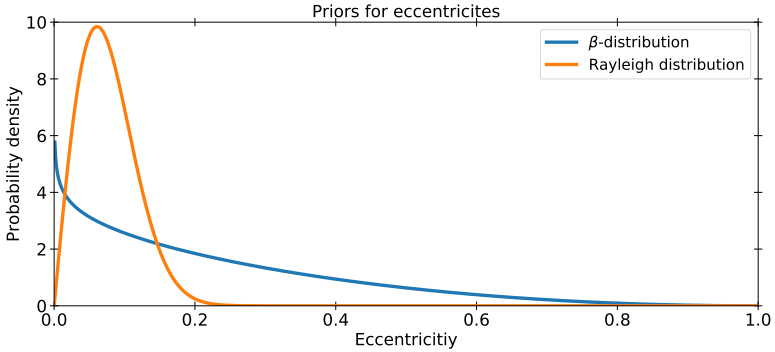

Figure 5.2.: Priors on eccentricities: β-distribution in blue, and Rayleigh distribution in orange.

Planetary masses have uniform priors in log-space by default, with minimum and maximum masses estimated via `Forecaster`. `Forecaster` uses a probabilistic mass–radius relation to predict the masses from radii. If some a priori information about the mass in known, the planetary mass prior can be set manually.

Longitude of the ascending node can only be determined via astrometry, or direct imaging. Since this information is usually not available, it is a common practice to set Ω of the innermost planet to zero and fit the Ω for all the other planets (e.g. Ragozzine & Holman, 2010) because only the differences between the angles affect the TTVs.

As a first guess, the parameters can be extracted by the analytical code `TTVFaster` that is combined with `emcee` in `PyTTV`.

5.2. Characterization of the Kepler-9 system

The Kepler-9 system was used to test the code and the influence of the choice of priors on the parameter estimation. The analysis includes the *Kepler* photometry and all available RV measurements, modeled simultaneously for the first time.

The system was modeled taking the gravitational interaction between Kepler-9b and Kepler-9c into account but ignoring the close-in planet Kepler-9d. This decision was made because Kepler-9d was found not to affect the orbits of Kepler-9b and Kepler-9c based on forward modeling with `PyTTV`, in agreement with the results from Holman et al. (2010).

First, the influence of different priors on the eccentricity was studied because of the known mass-eccentricity ambiguity. In addition, different priors on Ω of the Kepler-9c have been tested since the difference between the angles can be estimated. Second, the influence of GR and tidal interactions of the bodies were studied. Third, the influence of the different observations (TTVs, TDVs, and RVs) on the estimated parameters and their uncertainties was studied.

Influence of priors The derived masses for different priors on the eccentricities and Ω_{9c} using only the TTVs estimated in Sec. 4.1 are shown in Fig. 5.3. The different scenarios are:

1a: a uniform prior on Ω from 0 to $\pi/2$ and uniform priors on eccentricities.

1b: a uniform prior on Ω from 0 to 2π and uniform priors on eccentricities.

1c: a uniform prior on Ω from 0 to $\pi/2$ and β-priors on eccentricities.

1d: a uniform prior on Ω from 0 to π/2 and exponential-priors on eccentricities.

1e: a uniform prior on Ω from 0 to π/2 and Rayleigh priors on eccentricities.

The uniform priors on eccentricities (1a and 1b) lead to high-mass solutions with polar (1a) and retrograde (1b) orbits. This is due to the complexity of the unconstrained parameter space where even a global optimizer can converge to a wrong posterior mode. The scatter in the residuals of the fit using uniform priors on the eccentricities is higher and with systematic structures compared to the other scenarios with strongly constraining priors on the eccentricity (Fig. 5.4). Furthermore, since Wang et al. (2018) studied the Rossiter-McLaughlin effect in the Kepler-9 system and measured an angle of λ = -13° $\pm$ 16°, highly misaligned, polar, and retrograde orbits can be excluded. Therefore, scenarios with uniform priors on the eccentricities and $\Omega > \pi/2$ are no longer considered but instead informative priors on the eccentricities and $\Omega \leq \pi$/2 are used (scenarios 1c, 1d, and 1e).

If an informative but not restrictive prior is set on the eccentricity (β-prior), as in scenario 1c, the masses are significantly lower compared to scenarios 1a and 1b, and the orbits are aligned. Since the compact *Kepler* multi-planet systems usually have low eccentricities, the influence of a restrictive prior (exponential prior and the Rayleigh prior) is tested in scenarios 1d and 1e. Both distributions lead to solutions that are in good agreement with scenario 1c. The advantage of the latter two priors is that the parameter space is more constrained, whereby the optimization is faster. Therefore, these two priors are good choices if low eccentricities can be assumed, as it is the case for compact multi-planet systems.

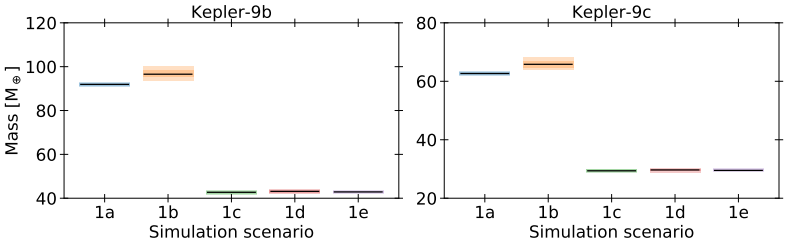

Figure 5.3.: Masses derived from TTVs assuming different priors for Kepler-9b and Kepler-9c on the left and on the right, respectively. In blue, scenario 1a with Ω from 0 to $\pi/2$ and uniform priors on eccentricities. In orange, scenario 1b with Ω from 0 to 2π and uniform priors on eccentricities. In green, scenario 1c with Ω from 0 to $\pi/2$ and β-priors on eccentricities. In red, scenario 1d with Ω from 0 to $\pi/2$ and exponential-priors on eccentricities. In violet, scenario 1e with Ω from 0 to $\pi/2$ and Rayleigh priors on eccentricities.

Since the Rayleigh prior is more appropriate for the modeling of *Kepler* multi-planet systems (Sec. 5.1.2), it is chosen as the default prior for eccentricities for Kepler-9b and Kepler-9c.

Influence of additional forces Forward modeling of the system was carried out with `PyTTV` to test if the transit times or planetary orbits are influenced by additional forces. Theoretical calculations (Sec. 3.1.3) predict that GR has the strongest influence on Kepler-9b and Kepler-9c. The orbital periods of the planets are too long for the tidal interactions to have a significant effect, as tested via forward modeling with `PyTTV`. `PyTTV` forward modeling shows that transit center times change due to GR in the time span of ten years around 2.5 minutes for Kepler-9b and 1.4 minutes for Kepler-9c, respectively. These changes are within the uncertainties of the TTVs. The parameter estimates do not differ significantly if GR is included, but since it represents the more physically correct model, the effect

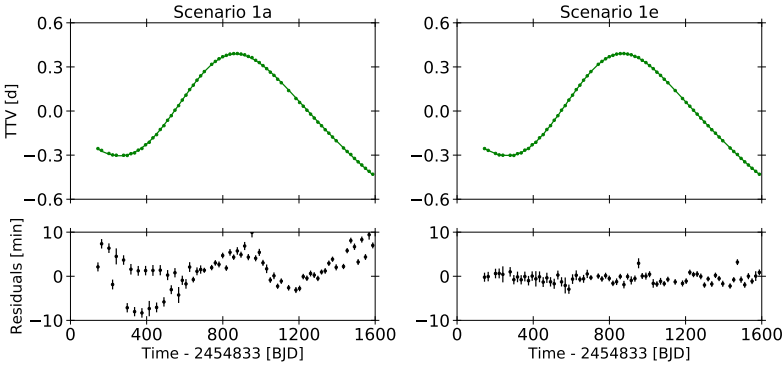

Figure 5.4.: Kepler-9b's TTVs (top panels) with residuals (lower panels) for the posterior median solution for scenario 1a (left; uniform priors on eccentricities) and 1e (right; Rayleigh priors on the eccentricities).

of GR was included in the following analyses.

Influence of observations Since the Kepler-9 system is well-studied (Holman et al., 2010; Borsato et al., 2014; Dreizler & Ofir, 2014; Wang et al., 2018; Freudenthal et al., 2018; Borsato et al., 2019), and RVs, as well as additional transits have been observed from the ground, the influence of the different measurements on the derived parameters is also studied. For the first time, in this work, the *Kepler* photometry observed in short cadence and long cadence mode, and all the available RV measurements from Holman et al. (2010) and Borsato et al. (2019), are modeled simultaneously to extract the physical quantities. Borsato et al. (2019) carried out RV follow-up and modeled the TTVs and TDVs, but they compared only the parameters estimated from the TTV and TDV fit with the RV measurements and found an agreement between both methods. However, they did not model the observations simultaneously. The results of

different combinations of observations are studied. The parameters for the different scenarios are shown in Fig. 5.5. The scenarios are:

1e: TTVs.

2e: TTVs and RVs from Borsato et al. (2019).

3e: TTVs and TDVs.

4e: TTVs, TDVs, and RVs from Borsato et al. (2019).

5e: TTVs and RVs from Borsato et al. (2019) and Holman et al. (2010).

6e: TTVs, TDVs, and RVs from Borsato et al. (2019) and Holman et al. (2010).

The TTVs and TDVs are estimated by `PyTTV`. In all the scenarios, a Rayleigh prior with parameters derived by Van Eylen et al. (2019) for multi-planet systems was set on the eccentricities.

TTVs The estimated planetary and orbital parameters from scenario 1e using only the TTVs are shown in blue in Fig. 5.5. Since the parameters were previously extracted using TTVs by Borsato et al. (2014), and Dreizler & Ofir (2014), the results from `PyTTV` are compared with their findings. The values agree within $3\,\sigma$ and within $1\,\sigma$ with the values reported by Dreizler & Ofir (2014) and Borsato et al. (2014), respectively.

This comparison shows that the parameter extraction by `PyTTV` functions in agreement with the results of Dreizler & Ofir (2014), and Borsato et al. (2014), if only TTVs are fitted.

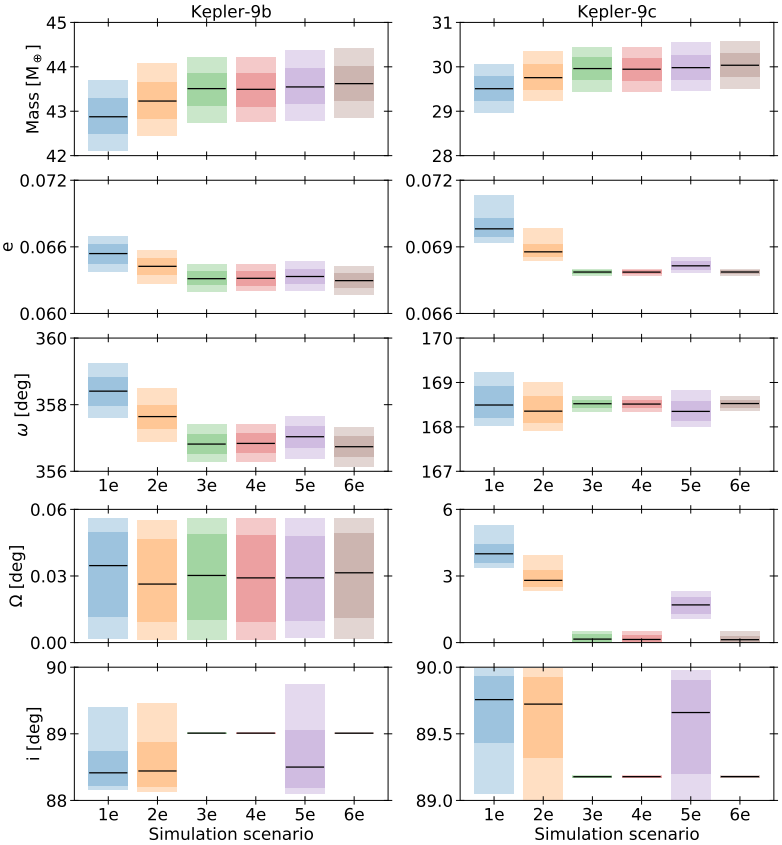

Figure 5.5.: Mass, eccentricity, argument of periastron, longitude of ascending node, and inclination (from top to bottom) for Kepler-9b and Kepler-9c on the left and on the right, respectively. The color code indicates the different scenarios. The 64% percentiles (99% percentiles) are indicated by the dark (light) shaded area, respectively.

TTVs and RVs Holman et al. (2010) fitted TTVs derived from the transits of light curves of the first three Quarters and six RVs measurements together, leading to planetary masses of $M_{\rm p} = 0.252 \pm 0.013\,{\rm M_{Jup}}$ and $M_{\rm p} = 0.171 \pm 0.013\,{\rm M_{Jup}}$ for Kepler-9b and Kepler-9c respectively. These values were corrected by Dreizler & Ofir (2014) and Borsato et al. (2014) who studied the influence on the estimated parameters if TTVs for 17 and 12 Quarters, respectively, and the RVs from Holman et al. (2010) are modeled simultaneously. Since they found that the TTVs are better fitted without the RVs, this case is not considered here. It should be noted that these RV observations have unrealistically low uncertainties and were one of the first RV measurements carried out for such a faint star as Kepler-9 (V=13.0 mag). Therefore, these observations need to be treated with caution.

Borsato et al. (2019) carried out a follow-up study to derive the planetary masses independent from the TTVs, but did not fit the observations simultaneously. Here, the TTVs and the RVs from Borsato et al. (2019) are modeled simultaneously with `PyTTV` (scenario 2e). The estimated planetary and orbital parameters from this scenario are shown in yellow in Fig. 5.5. Since this has not been analyzed before, the results are compared to scenario 1e where only the TTVs are modeled. The values agree within $1\,\sigma$, except for the eccentricity and Ω of Kepler-9c. The values for the planet masses increase if the RVs are included in the fit, while all other values decrease slightly. Since the orbital eccentricity is usually better constrained from RVs than from TTVs, the results from scenario 2e are favored.

The inclusion of the RVs from Holman et al. (2010) to the scenario 2e, leads to scenario 5e which is shown in violet in Fig. 5.5. The values for the planetary parameters agree within $1\,\sigma$ with the results from scenario 2e, except for the orbital eccentricity and Ω for Kepler-9c which agree within

$3\,\sigma$. Adding the RVs from Holman et al. (2010) to scenario 2e, leads to values that are more comparable to the results from scenarios 3e, 4e, and 6e, except for the inclination which is not constrained if only TTVs and RVs are modeled. This means that the combination of RV measurements from Holman et al. (2010) and Borsato et al. (2019) cover a time span that is long enough to constrain the orbital angles. Therefore, the results from scenario 5e are favored over the results from scenario 2e.

TTVs and TDVs The estimated planetary and orbital parameters from scenario 3e using the TTVs and TDVs are shown in green in Fig. 5.5. Since Borsato et al. (2019) fitted TTVs and TDVs and Freudenthal et al. (2018) used a photodynamical model that fits the complete transit shape, the results from `PyTTV` are compared with their findings. The values agree within $3\,\sigma$ with the values reported in Borsato et al. (2019) and Freudenthal et al. (2018). Compared to scenario 1e (TTVs) and 2e (TTVs + RVs), the planet masses for both planets are slightly higher, but still within 1σ; the orbital eccentricities are smaller, in particular for Kepler-9c ($3 > \sigma$); The values for ω for Kepler-9b differ more than $1\,\sigma$ and $3\,\sigma$ to scenario 2e and 1e, respectively. For Kepler-9c, the values for ω are the same, but have smaller uncertainties. Since Ω was not fitted for Kepler-9b, the value does not change, while for Kepler-9c they differ more than $3\,\sigma$. The values for the orbital inclinations have significantly smaller uncertainties if the durations are modeled simultaneously with the TTVs. In summary, including the TDVs in the fitting leads to significantly smaller uncertainties for Kepler-9b and Kepler-9c parameters (if they are fitted), except for the planetary mass. Since the orbital inclination is usually constrained from transit durations, the inclusion of TDVs in the parameter extraction significantly improve the values for the inclinations. Therefore, the results from

scenario 3e are favored.

TTVs, TDVs, and RVs The simultaneous analysis using TTVs, TDVs and the RVs from Borsato et al. (2019) is shown in red Fig. 5.5 and in addition with the RVs from Holman et al. (2010) in maroon, respectively. Both analyses lead to nearly the same values for every parameter and agree with the results from scenario 3e, where TTVs and TDVs are modeled simultaneous. The results from these three scenarios are indistinguishable. The results for scenario 6e obtained with `PyTTV` agree within 1σ and 3σ with the results from Borsato et al. (2019) and Freudenthal et al. (2018), respectively, but with smaller uncertainties. Since the values are indistinguishable, it is difficult to decide which scenario fits the TTV best. As a final result for the parameters, the posterior median solution from scenario 6e is chosen because this scenario includes all available information (Table 5.1). Figures 5.6 and 5.7 show the final TTVs and RVs for the scenario 6e. The TTV residuals are centered around zero for both planets, and the scatter is within the observational uncertainties without any systematic trends. The RV model of the best-fitting solution shows the same behavior as already mentioned: the RV measurements from Holman et al. (2010) have underestimated uncertainties. Since these measurements have less weight compared to the other measurements during the optimizing process, their underestimated uncertainties are compensated.

Conclusions The system was modeled considering the gravitational interaction between Kepler-9b and Kepler-9c, but ignoring the close-in planet Kepler-9d. In addition to the gravitational forces, the effect of GR was included in the parameter estimation, since its influence is of the order of the uncertainties in the TTVs. The results from the scenarios 3e,

Table 5.1.: Parameter posteriors for Kepler-9b and Kepler-9c modeling all observations (TTVs, TDVs, and RVs from Holman et al. (2010) and Borsato et al. (2019)) simultaneously (scenario 6e). The reported values are valid for the reference time reported in $t_0 = 2454969.202824$ BJD. Stellar mass and radius are fixed on the values of $M_\star = 1.022\,M_\odot$ and $R_\star = 0.958\,R_\odot$ derived in Borsato et al. (2019). The values for $R_p/R_\star$ are fitted from the light curve by `PyTTV`.

Parameter	Kepler-9b	Kepler-9c
	Values	
Fitted parameters		
$P_{\rm orb}$ [days]	19.22879 ± 0.00005	39.0374 ± 0.0003
T_0 [days]	8.0428 ± 0.0003	0.1004 ± 0.0005
$\log_{10} M_p/M_\star$	-3.883 ± 0.004	-4.045 ± 0.004
$R_p/R_\star$	0.0733 ± 0.0002	0.0716 ± 0.0002
$\sqrt{e}\cos\omega$	-0.014 ± 0.001	0.0518 ± 0.0004
$\sqrt{e}\sin\omega$	0.251 ± 0.001	-0.2553 ± 0.0002
i [°]	89.009 ± 0.006	89.179 ± 0.005
Ω [°]	0.03 ± 0.02	0.1 ± 0.1
Derived parameters		
M_p [$M_\oplus$]	43.6 ± 0.4	30.0 ± 0.3
R_p [$R_\oplus$]	7.66 ± 0.02	7.49 ± 0.02
ρ_p [g cm^{-3}]	0.533 ± 0.006	0.393 ± 0.005
e	0.0630 ± 0.0006	0.06787 ± 0.00007
ω [°]	356.7 ± 0.3	168.53 ± 0.09
Parameter	Kepler-9b	Kepler-9c
	Priors	
Fitted parameters		
$P_{\rm orb}$	$\mathcal{N}$(19.238,0.05)	$\mathcal{N}$(38.985,0.05)
$\log_{10} M_p/M_\star$	$\mathcal{U}$(-5,-2)	$\mathcal{U}$(-5,-2)
$\sqrt{e}\cos\omega$	$\mathcal{U}$(-1,1)	$\mathcal{U}$(-1,1)
$\sqrt{e}\sin\omega$	$\mathcal{U}$(-1,1)	$\mathcal{U}$(-1,1)
i [°]	$\mathcal{U}(0.489\pi, \pi/2)$	$\mathcal{U}(0.493\pi, \pi/2)$
Ω [°]	$\mathcal{U}$(0, 0.001)	$\mathcal{U}(0, \pi/2)$
Derived parameters		
e	Rayleigh(0, 0.061)	Rayleigh(0, 0.061)
ω [°]	$\mathcal{U}(0, 2\pi)$	$\mathcal{U}(0, 2\pi)$

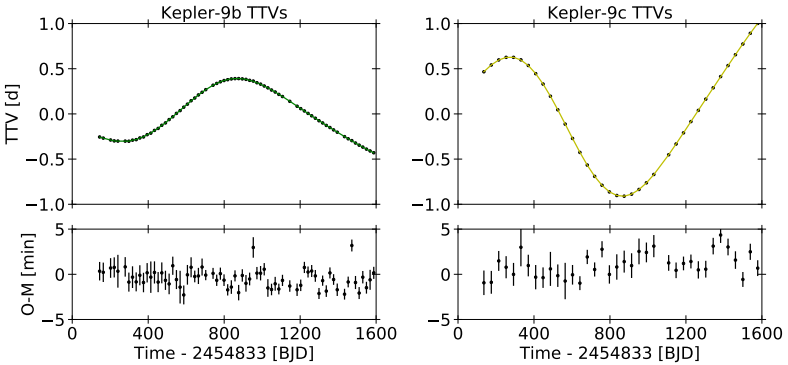

Figure 5.6.: TTVs for Kepler-9b (left panel) and Kepler-9c (right panel) with residuals denotes as observed-modeled (O-M) (lower panels) for the posterior median solution of scenario 6e. The observed TTVs are marked in black, while the lines mark the best TTV-fit.

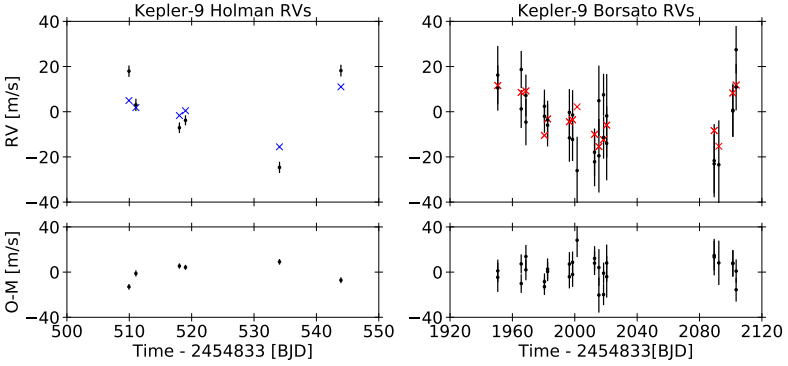

Figure 5.7.: RVs for Kepler-9 from Holman et al. (2010) (left panel) and Kepler-9c from Borsato et al. (2019) (right panel) in black with residuals denotes as observed-modeled (O-M) (lower panels) for the posterior median solution for scenario 6e marked with blue and red x, for the Holman et al. (2010) and Borsato et al. (2019) RVs, respectively.

4e, and 6e are indistinguishable. This means that the planetary parameters for Kepler-9b and Kepler-9c are already well-fitted by TTVs and TDVs, without adding RV measurements. As a final result for the parameters, the posterior median solution from scenario 6e is chosen because this scenario includes all available information. The results obtained with `PyTTV` agree well with the results from Borsato et al. (2019) and Freudenthal et al. (2018), respectively, but with smaller uncertainties.

The example of the Kepler-9 system has proven the ability of `PyTTV` to extract the physical quantities from measured TTVs, TDVs, and RVs. The analysis presented here with `PyTTV` includes the *Kepler* photometry and all available RV measurements modeled simultaneously for the first time. The parameters estimated by `PyTTV` agree with the published values in Borsato et al. (2019) and Freudenthal et al. (2019)

5.3. Characterization of the Kepler-289 system

The Kepler-289 system, also known as PH3, hosts three planets of different compositions from rocky to Jovian. The inner and outer planets, Kepler-289b (PH3b) and Kepler-289c (PH3d) with periods of 34.53 days and 125.87 days, were discovered by Borucki et al. (2011b) and Batalha et al. (2013), and validated as planets by Rowe et al. (2014). Schmitt et al. (2014) detected an additional planet within the Planet Hunter (PH) search, Kepler-289d (PH3c), with a period of 66.02 days. The planets are close to a period commensurability with their neighbor, but they were found not to be in a 1:2:4 Laplace resonance by Schmitt et al. (2014). These authors were also the first to detect the sinusoidal TTVs for the middle and

the outer planet. Mazeh et al. (2013) detected only parabolic TTVs of the outer planet, while Holczer et al. (2016) confirmed the sinusoidal TTVs of Kepler-289c with a TTV period of 1277 ± 40 days and a TTV amplitude of 8.9 ± 0.7 minutes. The TTVs for the middle planet were not detected, since both studies focused only on KOIs and the middle planet was not in the KOI list. Furthermore, Kane et al. (2019) reported also the sinusoidal TTVs of the outer planet with an amplitude of 5.3 minutes and a period of 1235 days.

A chopping signal in the TTVs of the middle planet allowed Schmitt et al. (2014) to uniquely determine the planetary masses of all three planets via their TTVs assuming circular orbits to $M_{\rm p} = 7.3 \pm 6.8\ {\rm M}_{\oplus}$, $M_{\rm p} = 4.0 \pm 0.9\ {\rm M}_{\oplus}$, and $M_{\rm p} = 132 \pm 17\ {\rm M}_{\oplus}$ for Kepler-289b, Kepler-289d, and Kepler-289c, respectively. They noted that the masses determined via TTVs are more constrained for the outer planet than for the middle planet, because of the strong TTVs of the middle planet. They estimated a planetary density for Kepler-289d of $\rho_{\star} = 1.2 \pm 0.3\ {\rm g\,cm^{-3}}$ that places the planet into the range of the low-mass, low-density, "puffy planets". This class of planets requires a significant H/He envelope.

The system is one of the few multi-planet systems that resemble the Solar system with smaller planets on inner orbits (Kepler-289b and Kepler-289d) and outer massive planets (Kepler-289c). In addition, the planets are close to a period commensurability, but not trapped in a Laplace resonance. Therefore, it is an excellent target to test the formation theories for multi-planet systems consisting of planets near a resonant chain (e.g. Pichierri et al., 2019).

Santerne et al. (2016) observed this system with SOPHIE and estimated the planetary masses. They found upper limits of $M_{\rm p} < 0.52\ {\rm M}_{\rm Jup}$ for the inner planet, and $M_{\rm p} < 1.42\ {\rm M}_{\rm Jup}$ for the middle planet using only

their RV observations. For Kepler-289c, they reported a planet mass of $M_{\rm p} = 1.55 \pm 0.34$ $M_{\rm Jup}$. The values for the inner and middle planet agree with the values found by Schmitt et al. (2014) via TTVs, but for the outer planet the values disagree ($> 3\,\sigma$). They noted that the discrepancy could be caused by the photometric variability of more than 1.5%.

The discrepancy in the planet mass for the outer planet, Kepler-289c, and the low-density for the middle planet, Kepler-289d, motivated the re-analysis of this system with `PyTTV`. Moreover, the *Kepler* photometry and the RV measurements from Santerne et al. (2016) are modeled simultaneously for the first time.

Transit Timing variations The transit center times, durations, and depths have been extracted with `PyTTV` using the PDCSAP flux in long cadence and short cadence mode. Significant TTVs were detected by `PyTTV` for Kepler-289c and Kepler-289d, but not for the inner planet (Fig. 5.8), in agreement with the findings from Schmitt et al. (2014). The TTVs of the outer planets are anti-correlated confirming their mutual gravitational interactions. The chopping signal is clearly visible in the TTVs for the middle planet, but suppressed by the outliers (transit number 6, 7, 11, and 14). The diagnostics of the TTVs are summarized in Table 5.2. The anti-correlation of the TTVs of Kepler-289d and Kepler-289c is reflected in their phase values. The TTV periods of 1066.8 ± 22.3 days and 1048.9 ± 49.0 days derived by `PyTTV` for Kepler-289d and Kepler-289c, respectively, agree with each other, indicating that the TTVs for each planet is dominated by the perturbations of the other planet. Therefore, the estimated TTV periods and the anti-correlated phase confirm the mutual gravitational interaction between both planets. The TTV periods for Kepler-289c agree within 3σ and 4σ with the TTV period found by

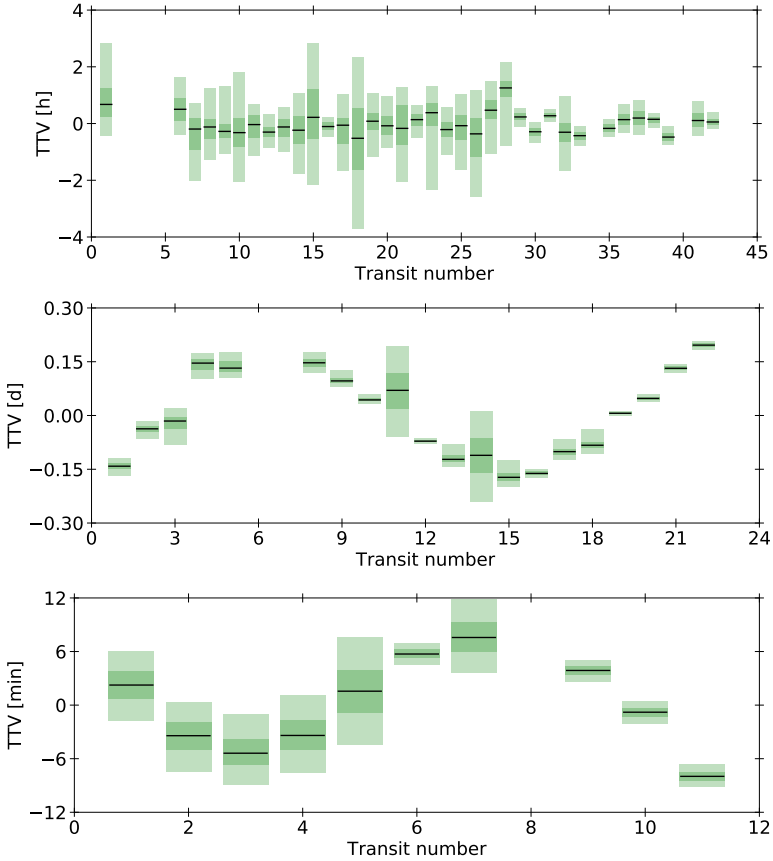

Figure 5.8.: TTVs for Kepler-289b (top panel), Kepler-289d (middle panel), and Kepler-289c (lower panel). Some transits were removed because of bad data quality (transit number 2, 3, 4, 5 for Kepler-289b, transit number 6 and 7 for Kepler-289d, and transit number 8 for Kepler-289c). The anti-correlated TTVs of Kepler-289c and Kepler-289d is clearly visible.

Table 5.2.: Diagnostics for the Kepler-289 system. The values for ϕ are reported as normalized phase with values [0,1], allowing for negative values. The TTVs for Kepler-289c and Kepler-289d are found to be significant.

Kepler-289b: 34.5440 ± 0.0002 days			
	TTV	TDV	TPV
Model	sin	con	con
Period [days]	101.2 ± 1.8	-	-
Amplitude [min]	16.4 ± 3.4	-	-
Phase	-0.11 ± 0.03	-	-
FAP	0.007	-	-
Kepler-289d: 66.023 ± 0.004 days			
	TTV	TDV	TPV
Model	sin	con	con
Period [days]	1066.8 ± 22.3	-	-
Amplitude [min]	252.8 ± 6.9	-	-
Phase	-0.135 ± 0.005	-	-
FAP	4.8e-13	-	-
Kepler-289c: 125.867 ± 0.001 days			
	TTV	TDV	TPV
Model	sin	con	sin
Period [days]	1048.9 ± 49.0	-	314.7 ± 16.3
Amplitude [min, ppt]	5.8 ± 0.3	-	0.6 ± 0.1
Phase	0.45 ± 0.01	-	$-0.02, \pm 0.03$
FAP	0.0002	-	0.07

Holczer et al. (2016) and Kane et al. (2019),[1] respectively. The TTV amplitudes estimated by `PyTTV` of 5.8 ± 0.3 minutes for Kepler-289c agree within 2σ with the one derived by Kane et al. (2019) and within 4σ with

[1] Since Kane et al. (2019) do not provide uncertainties, a quantitative comparison is not possible.

the value estimated by Holczer et al. (2016). The large difference in the TTV periods and amplitudes results from the fact that no complete cycle of the TTV period was observed, and the frequency search implemented in `GLS` prevents the detection of periodicities which are longer than the observation time span.

However, the strong TTV of Kepler-289d and the weaker TTV of Kepler-289c could be clearly identified. Transit durations and transit depths do not show significant variations. Indeed, TPVs have been detected for Kepler-289c by the ΔBIC but the FAP was too high. The detection is probably caused by noise.

Parameter estimation The estimated transit center times and transit durations from `PyTTV`, and the RVs from Santerne et al. (2016) were used to determine the planetary system parameters. For the parameter estimation with `PyTTV`, only the gravitational forces between the planets were considered. The planets are too far away from the star to be influenced by GR as tested by `PyTTV` forward modeling. The tidal influence of the outer planet on the middle planet was excluded through forward modeling with `PyTTV`. Different combinations of the observations (TTVs, TDVs, and RVs) were carried out to study their individual influence on the parameter extraction because the system was so far only analyzed via TTVs or RVs alone. The scenarios are:

1: TTVs.

2: TTVs and circular orbits.

3 TTVs and TDVs,

4 TTVs and RVs.

5 TTVs, TDVs, and RVs.

Rayleigh priors on the eccentricities were assumed for all the scenarios (see Fig. 5.2), except for scenario 2 where circular orbits are assumed as in the studies by Schmitt et al. (2014) and Santerne et al. (2016).

TTVs The estimated parameters using only the TTVs and Rayleigh priors on the eccentricity are shown in blue and assuming circular orbits in yellow in Fig. 5.9, respectively. Since the planet parameters assuming circular orbits were previously estimated by Schmitt et al. (2014), the results from `PyTTV` for scenario 2 are compared to their findings. The values for the planet masses of $M_{\rm p} = 0.2 \pm 0.3$ $\mathrm{M}_{\oplus}$, $M_{\rm p} = 5.6 \pm 0.3$ $\mathrm{M}_{\oplus}$, and $M_{\rm p} = 166 \pm 2$ $\mathrm{M}_{\oplus}$ for Kepler-289b, Kepler-289d, and Kepler-289c, respectively (upper panels in Fig. 5.9), agree within 2σ with the values in Schmitt et al. (2014). The lower limit of the inner planet's mass is not constrained by the observation. The values for the inclination (lower panels in Fig. 5.9) agree within 3σ, while all the other parameters are not defined for circular orbits and therefore not constrained. If instead a Rayleigh prior on the eccentricity is chosen, the values for the planet masses differ more than 3σ. While the planet mass for the inner planet is not well-constrained and becomes larger, the planet masses for the outer planets become smaller. It is noticeable that allowing for eccentric orbits during the fitting leads to higher orbital eccentricities for all three planets (second row in upper panels in Fig. 5.9). This means that, if the eccentricities are not fixed to zero as in scenario 2 and by Schmitt et al. (2014), there is evidence in the data for eccentric orbits. Since it is usually not recommended to fix the eccentricity (or any other parameter), it is better to set a prior on it that allows for small and larger eccentricities as it is the case for the Rayleigh prior. Therefore, the results from scenario 1 estimated by `PyTTV` are fa-

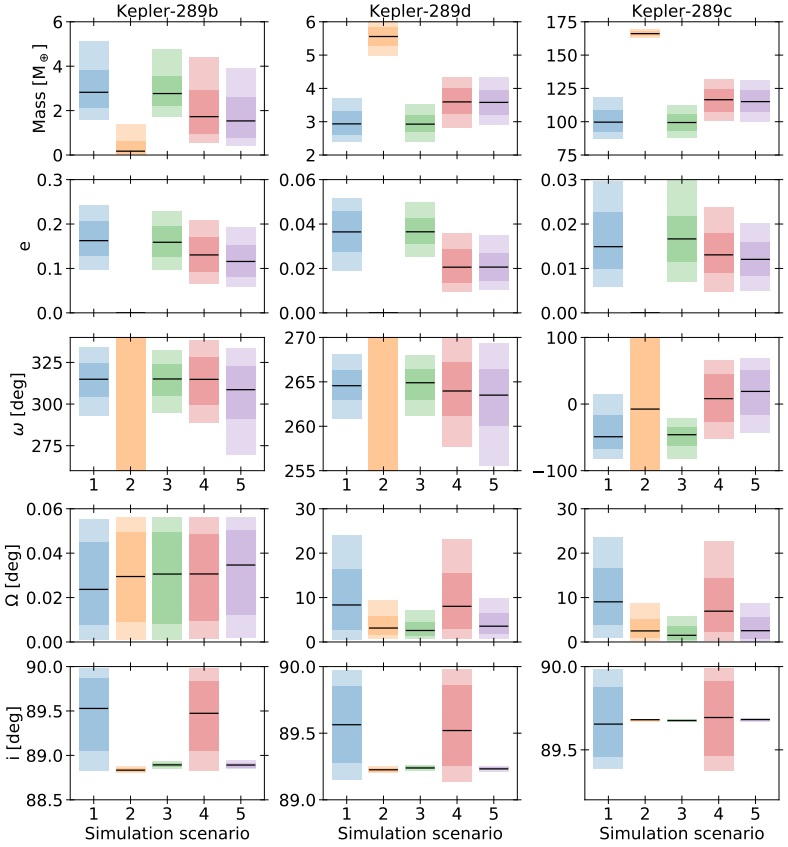

Figure 5.9.: Mass, eccentricity, argument of periastron, longitude of ascending node, and inclination (from top to bottom) for Kepler-289b (left panels), Kepler-289d (middle panels), and Kepler-289c (right panels). The color code indicates the different scenarios. The black lines mark the 50% percentiles of the posterior estimate. The 64% percentiles (99% percentiles) are indicated by the dark (light) shaded area, respectively.

vored over the results assuming circular orbits, and the Rayleigh prior is taken as the default prior for all the scenarios.

TTVs and TDVs The estimated planetary and orbital parameters from scenario 3 using the TTVs and TDVs are shown in green in Fig. 5.9. Fitting TTVs and TDVs together does not change the values compared to the case if only TTVs are fitted (blue) apart from the inclinations and Ω for all planets[2]. Since the inclusion of the TDVs in the parameter estimation constrains the inclination and Ω, scenario 3 is favored over scenario 1.

TTVs and RVs The estimated planetary and orbital parameters from scenario 4 using the TTVs and RVs from Santerne et al. (2016) are shown in red in Fig. 5.9. Apart from the planet mass and orbital eccentricity for all three planets and Ω for the outer planet, the inclusion of RVs does not change the other parameters significantly compared to scenario 1 (in blue). The planet mass for the inner planet becomes smaller, while the planet masses for the outer planets become larger. The eccentricities are all lower compared to scenario 1, but still within the uncertainties. The inclusion of the RVs adds information and affects the parameter estimation. Therefore, scenario 4 can be favored over scenario 1 and 3.

TTVs, TDVs, and RVs The estimated planetary and orbital parameters from scenario 5 using the TTVs, TDVs, and RVs from Santerne et al. (2016) are shown in violet in Fig. 5.9. The comparison with previous scenarios shows that the addition of RV observations changes mainly the planet mass and eccentricity, while the TDVs affect mainly the inclina-

[2] Ω for the inner planet is set to zero, since only the difference can be fitted

tion. Since the scenario 5 uses all the available information, its results are considered as the final results.

Conclusions The simultaneous modeling of the TTVs, TDVs, and RVs for Kepler-289 shows that the inclusion of the RV measurements from Santerne et al. (2016) improves the parameter estimation for the Kepler-289 system, in particular for planet mass and eccentricity. Also, the transit duration measurements help to constrain the orbital inclination. Allowing for eccentric orbits favors non zero eccentricity for the innermost planet and moderate eccentricities for the outer planets. In addition, allowing for eccentric orbits significantly improved the mass estimate for the inner planet, which had no lower constraints when forcing circular orbits. Therefore, the posterior estimate from scenario 5 is considered as the best-modeled solution. The analysis of the system using TTVs, TDVs, and RVs leads to more constrained values for the planetary masses for all the planets with significantly smaller uncertainties.

Although Schmitt et al. (2014) assumed circular orbits in their TTV analysis, they mentioned that due to the chopping signal the mass-eccentricity ambiguity is broken allowing for a unique mass determination. This sounds more like a contradiction. How can the ambiguity be broken if circular orbits are assumed? This fact strengthens the eccentric solution found by `PyTTV`.

The discrepancy for the outer planet's mass found by Santerne et al. (2016) vanishes. The solution for the planet mass found by `PyTTV` assuming circular orbits agrees within 3σ with the value derived from the RVs by Santerne et al. (2016). This points up the importance of individual analysis and re-analysis for systems where TTVs and RVs lead to disagreeing values. The TTV and RV discrepancy could be solved, simply

Table 5.3.: Parameter posteriors for the Kepler-289 system modeling TTVs and TDVs estimated from `PyTTV` simultaneously (scenario 5). The reported values are valid for the reference time reported in $t_0 = 2454965.612193818$. Stellar mass and radius are fixed on the values of $M_\star = 1.1 M_\odot$ and $R_\star = 1.1\,R_\odot$ derived in Morton et al. (2016). The values for $R_p/R_\star$ are fitted from the light curve by `PyTTV`.

Parameter	Kepler-289b	Kepler-289d	Kepler-289c
		Values	
Fitted parameters			
$P_{\rm orb}$ [days]	34.5410 ± 0.0007	66.045 ± 0.005	125.8635 ± 0.0004
T_0 [days]	0.078 ± 0.005	10.034 ± 0.005	104.0526 ± 0.0005
$\log_{10} M_p/M_\star$	-5.3 ± 0.3	-4.97 ± 0.05	-3.46 ± 0.03
$R_p/R_\star$	0.0214 ± 0.0008	0.026 ± 0.001	0.1040 ± 0.0006
$\sqrt{e}\cos\omega$	-0.26 ± 0.06	-0.14 ± 0.02	0.03 ± 0.06
$\sqrt{e}\sin\omega$	0.21 ± 0.09	-0.017 ± 0.007	0.09 ± 0.03
i [°]	88.89 ± 0.03	89.23 ± 0.01	89.676 ± 0.003
Ω [°]	0.03 ± 0.02	3.6 ± 2.3	2.5 ± 2.4
Derived parameters			
M_p [$M_\oplus$]	1.5 ± 0.9	3.6 ± 0.4	115 ± 8
R_p [$R_\oplus$]	2.6 ± 0.1	3.2 ± 0.1	12.48 ± 0.07
ρ_p	0.4 ± 0.3	0.6 ± 0.1	0.33 ± 0.02
e	0.12 ± 0.04	0.021 ± 0.006	0.012 ± 0.004
ω [°]	315 ± 16	264 ± 3	19 ± 33
Parameter	Kepler-289b	Kepler-289d	Kepler-289c
		Priors	
Fitted parameters			
$P_{\rm orb}$ [days]	$\mathcal{N}(34.5450, 0.05)$	$\mathcal{N}(66.06, 0.05)$	$\mathcal{N}(125.85, 0.05)$
$\log_{10} M_p/M_\star$	$\mathcal{U}$(-6.-3)	$\mathcal{U}$(-5,5.-2.8)	$\mathcal{U}$(-4.0.-2.5)
$\sqrt{e}\cos\omega$	$\mathcal{U}$(-1,1)	$\mathcal{U}$(-1,1)	$\mathcal{U}$(-1,1)
$\sqrt{e}\sin\omega$	$\mathcal{U}$(-1,1)	$\mathcal{U}$(-1,1)	$\mathcal{U}$(-1,1)
i [°]	$\mathcal{U}(0.472\pi,\pi/2)$	$\mathcal{U}(0.472\pi,\pi/2)$	$\mathcal{U}(0.472\pi,\pi/2)$
Ω [°]	$\mathcal{U}$(0,0.001)	$\mathcal{U}(0,\pi/2)$	$\mathcal{U}(0,\pi/2)$
Derived parameters			
e	Rayleigh(0, 0.061)	Rayleigh(0, 0.061)	Rayleigh(0, 0.061)
ω [°]	$\mathcal{U}(0,2\pi)$	$\mathcal{U}(0,2\pi)$	$\mathcal{U}(0,2\pi)$

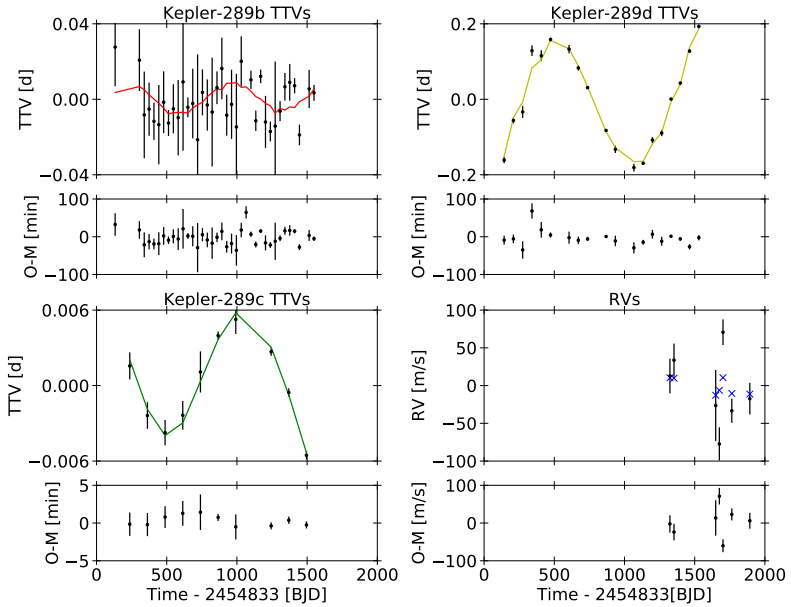

Figure 5.10.: TTVs for Kepler-289b (upper left panel), Kepler-289d (upper right panel), and Kepler-289d (lower left panel) and RVs (lower right panel) with residuals denotes as observed-modeled (O-M) for the posterior median solution of scenario 5. The observed TTVs and RVs are marked in black, while the lines mark the best TTV-fit and the blue x mark the modeled RV points.

through a re-analysis.

In summary, the analysis with `PyTTV` using all available observations (TTVs, TDVs, and RVs) leads to more accurate values for the planetary parameters with significantly smaller uncertainties.

5.4. Characterization of the K2-146 system

The TTV search for this system was presented in Sec. 4.4.2. The planetary parameters were already determined by Lam et al. (2020) fitting the TTVs and by Hamann et al. (2019) fitting TTVs and impact parameter values averaged over each Campaign. Here, the simultaneous modeling using the TTVs and TDVs is carried out for the first time. No RV observations were performed since the star is too faint with $m_v = 16.18$ mag.

The estimated transit center times and transit durations from `PyTTV` were used to determine the planetary system parameters. For the parameter estimation with `PyTTV`, only the gravitational forces between the planets were considered. Forward modeling with `PyTTV` ruled out the influence of GR and tidal interactions. Since no chopping signal which would break the mass-eccentricity ambiguity was detected in the TTVs, the influence on the planetary masses by different priors on the eccentricity has been studied for TTVs and for the combination of TTVs and TDVs. The scenarios are:

1a: TTVs and TDVs and uniform priors on eccentricities.

1b: TTVs and TDVs and β-priors on eccentricities.

1c: TTVs and TDVs and Rayleigh-priors on eccentricities.

2a: TTVs and uniform priors on eccentricities.

2b: TTVs and β-priors on eccentricities.

2c: TTVs and Rayleigh-priors on eccentricities.

The system was modeled backward in time. If the system is modeled forward in time, the grazing configuration of K2-146c at the beginning of

the *K2* observations complicates accurate parameter estimation: the global optimizer has problems finding good starting values and gets stuck in a local minimum. In contrast, if the simulation is carried out backward in time, starting from the end of the observing window of *K2* where both planets have measured transit times, the global optimizer finds good starting values and the optimization converges.

TTVs The estimated parameters using only the TTVs and uniform priors, β-priors, and Rayleigh priors on the eccentricity are shown in red, violet and maroon in Fig. 5.11, respectively. While the planetary masses increase for both planets, the eccentricity decreases for K2-146b and increases for K2-146c, if more constraining priors are used for the fit. In all the cases moderate eccentricities are favored. The values for ω for K2-146c are constant for all three scenarios, while the values for ω for the inner planet go close to an anti-aligned configuration (red, scenario 2a). The other parameters are not affected by the choice of the eccentricity prior. Planetary mass, orbital eccentricity for both planets, and ω for the inner planet differ around 3σ for the priors. This suggests that the parameter estimation is sensitive to the choice of priors preventing a robust determination of the planetary masses and orbital eccentricity.

Since the planetary parameters were previously estimated fitting only the TTVs by Lam et al. (2020), and Hamann et al. (2019), the results from `PyTTV` are compared to their findings. Lam et al. (2020) used backward modeling of the TTVs comparable with the modeling of `PyTTV` as described above. Their results for the planetary masses and eccentricities are marked with gray lines in Fig. 5.11. The solid lines denote the median values and the dashed lines mark the uncertainties. The simulation in Hamann et al. (2019) is performed backward and forward, leading to a dif-

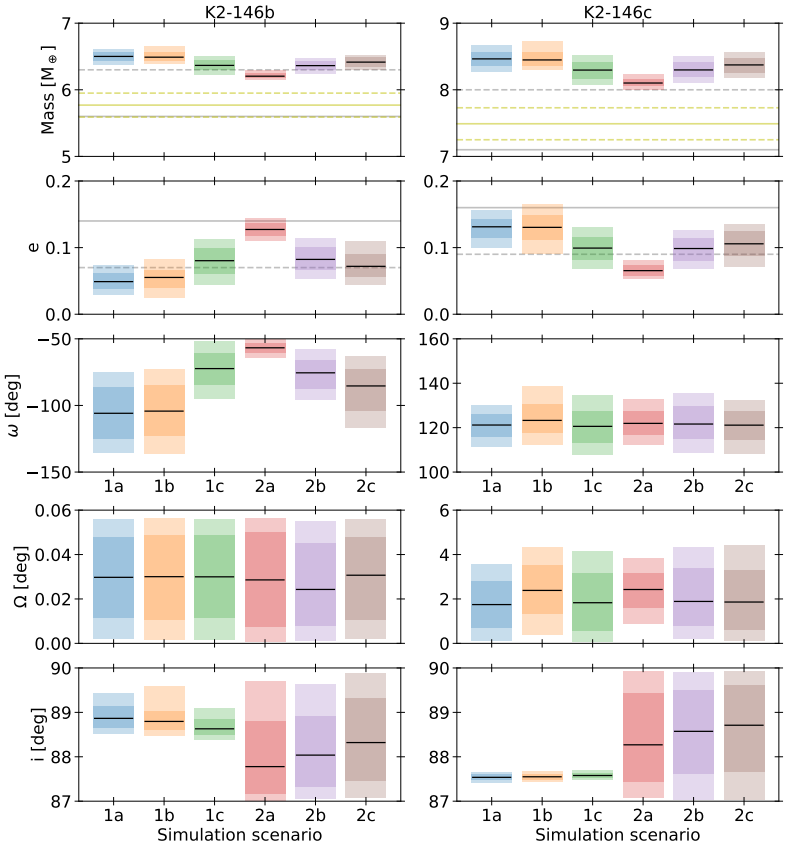

Figure 5.11.: Mass, eccentricity, argument of periastron, longitude of ascending node, and inclination (from top to bottom) for K2-146b (left panels), and K2-146c (right panels). The color code indicates the different scenarios. The black lines mark the 50% percentiles of the posterior estimate. The 64% percentiles (99% percentiles) are indicated by the dark (light) shaded area, respectively. The gray and yellow lines mark the median (solid lines) and uncertainties (dashed lines) solutions from Lam et al. (2020), and Hamann et al. (2019).

ferent reference time. Therefore, only the values for the time-independent parameter, the planetary mass, are marked in Fig. 5.11 with yellow lines. The estimated planetary masses from `PyTTV` are higher than the values determined by Lam et al. (2020) and Hamann et al. (2019) for all the scenarios. The eccentricities derived by Lam et al. (2020) have large uncertainties. They cover all the values, except the values for the eccentricity of scenario 2a for K2-146c.

The comparison with the values in Lam et al. (2020) and Hamann et al. (2019) reveal a discrepancy between the TTV analysis presented here and the TTV analysis of Lam et al. (2020) and Hamann et al. (2019). The reason for this discrepancy can be explained by the choice of different priors on the eccentricities, because the parameter estimation is sensitive to the choice of a prior.

TTVs and TDVs The estimated parameters using TTVs and TDVs and uniform priors, β-priors, and Rayleigh priors on the eccentricity are shown in blue, orange, and green in Fig. 5.11, respectively. Fitting TTVs and TDVs together changes significantly the values for the planetary masses, eccentricities for both planets and ω of the inner planet compared to the case if only TTVs are fitted. The inclusion of TDVs constrains the inclinations, as expected. It is noticeable, that the inclusion of the TDVs has an opposite effect on the parameters compared to the scenarios 2 (with the same priors on the eccentricities). The inclusion of the TDVs does not help to find a definite solution for the planetary masses and orbital eccentricities, these parameters still dependent on the choice of the prior.

Conclusions The `PyTTV` analysis for K2-146 shows that the solution is sensitive to the choice of eccentricity priors. Nevertheless, the planetary

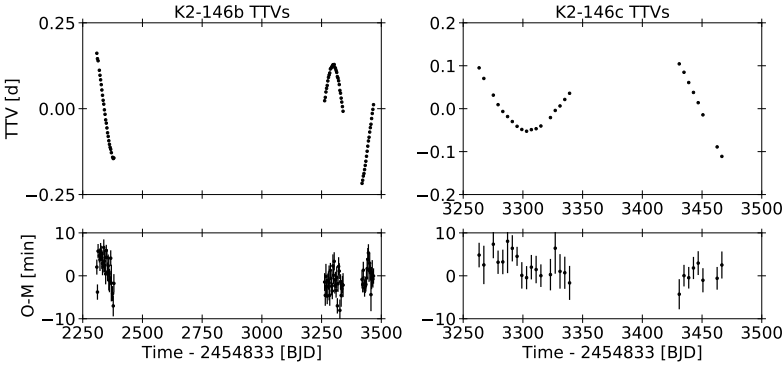

Figure 5.12.: TTVs for K2-146b (upper left panel) and K2-146c (upper right panel) with residuals denotes as observed-modeled (O-M) for the posterior median solution of scenario 1a. The observed TTVs are marked in black.

masses are well-constrained and do not change significantly from scenario to scenario. The sensitivity on the priors in this case, complicates the interpretation of the solutions as in the cases presented in Jontof-Hutter et al. (e.g. 2016), and Hadden & Lithwick (2017). A detailed migration model or long-term stability analysis would be valuable to study the different orbital configuration and planetary masses.

As the final result, the scenario 1a is chosen, since it uses the least restrictive priors on the eccentricities and includes the information from TTVs and TDVs (see Table. 5.4 and Fig. 5.12).

Table 5.4.: Parameter posteriors for the K2-146 system modeling TTVs and TDVs estimated from `PyTTV` simultaneously (scenario 1a). The reported values are valid for the reference time reported in $t_0 = 2458300.5372$. Stellar mass and radius are fixed on the values of $M_\star = 0.358 M_\odot$ and $R_\star = 0.350\,R_\odot$ derived in Hirano et al. (2018). The values for $R_p/R_\star$ are fitted from the light curve by `PyTTV`.

Parameter	K2-146b	K2-146c
	Values	
Fitted parameters		
$P_{\rm orb}$ [days]	2.66962 ± 0.00004	3.9669 ± 0.0002
T_0 [days]	-0.1000 ± 0.0004	-0.9341 ± 0.0008
$\log_{10} M_p/M_\star$	-4.709 ± 0.004	-4.595 ± 0.005
$R_p/R_\star$	0.058 ± 0.001	0.08 ± 0.01
$\sqrt{e}\cos\omega$	-0.20 ± 0.03	0.31 ± 0.02
$\sqrt{e}\sin\omega$	-0.06 ± 0.07	-0.19 ± 0.03
i [°]	88.9 ± 0.2	87.54 ± 0.06
Ω [°]	0.03 ± 0.02	1.7 ± 1.0
Derived parameters		
M_p [$M_\oplus$]	6.50 ± 0.06	8.5 ± 0.1
R_p [$R_\oplus$]	2.21 ± 0.05	2.9 ± 0.3
ρ_p	3.3 ± 0.2	1.8 ± 0.6
e	0.05 ± 0.01	0.13 ± 0.01
ω [°]	-106 ± 19	121 ± 5
Parameter	K2-146b	K2-146c
	Priors	
Fitted parameters		
$P_{\rm orb}$ [days]	$\mathcal{N}(2.650, 0.005)$	$\mathcal{N}(3.989, 0.005)$
$\log_{10} M_p/M_\star$	$\mathcal{U}(-5.3.-3.5)$	$\mathcal{U}(-5,3.-3.5)$
$\sqrt{e}\cos\omega$	$\mathcal{U}(-1,1)$	$\mathcal{U}(-1,1)$
$\sqrt{e}\sin\omega$	$\mathcal{U}(-1,1)$	$\mathcal{U}(-1,1)$
i [°]	$\mathcal{U}(0.483\pi,\pi/2)$	$\mathcal{U}(0.472\pi,\pi/2)$
Ω [°]	$\mathcal{U}(0,0.001)$	$\mathcal{U}(0,\pi/2)$
Derived parameters		
e	$\mathcal{U}(0,0.7)$	$\mathcal{U}(0,0.7)$
ω [°]	$\mathcal{U}(0,2\pi)$	$\mathcal{U}(0,2\pi)$

6

Summary and future prospects

Since the announcement of the first extrasolar planet around the neutron star
PSR1257+12 (Wolszczan & Frail, 1992), and of the first exoplanet around a sunlike star (51 Pegasi) by Nobel prize laureates D. Queloz and M. Mayor 1995 (Mayor & Queloz, 1995), the speed of discoveries in the field of exoplanet research has increased dramatically. The understanding of the evolution and formation of extrasolar planetary systems requires a detailed characterization of the extrasolar planets by its composition and density which is limited by current conventional observational methods.

Studies of the *Kepler* sample unveiled, among other things, that planetary systems with multiple planets seem to be common (Lissauer et al., 2012; Fabrycky et al., 2014; Rowe et al., 2014). Most of these detected multi-planet systems reside in compact configurations where the planets interact gravitationally with each other. The gravitational interaction between the planets in compact multi-planet systems leads to deviations in their observed transit times and durations (Agol et al., 2005; Holman & Murray, 2005; Agol & Fabrycky, 2018). The system properties, like planetary mass and orbital parameters, are embedded in these deviations.

Thus, measurements of these deviations may reveal the orbital architecture through the inverting of the transit timing variation signal.

One advantage of the TTV method its capability to determine masses, and therefore the densities, of planets that have host stars that are too faint for characterization via radial velocity observation (Xie, 2013, 2014; Jontof-Hutter et al., 2016; Hadden & Lithwick, 2016, 2017; Hadden et al., 2019). TTVs are sensitive to low-mass planets below the current RV detection limit, as well as to non-transiting planets. These advantages and the commonness of multi-planet systems make TTVs a preferable method for characterizing systems that aren't easily accessible with other techniques. However, if TTV and radial velocity measurements are obtained for the same systems, the combinations of both methods can help to constrain the planetary masses. This is of particular interest due to the ambiguity of planetary masses and eccentricities. In addition, measurements of the transit duration help to constrain the inclination.

Although the TTVs are mainly caused by the mutual gravitational interactions between the planets, the orbits of planets in some exoplanet systems cannot be explained purely by gravitational perturbations. The orbit of a planet can also undergo orbital precession due to general relativistic effects and tidal interactions. These forces may have an essential influence for systems with ultra-short-period planets, hot Jupiters, or very compact multi-planet systems. They can produce long-term TTVs which can be measured if the observational time span is long enough.

Combining light curves from different missions like *Kepler* and *TESS* produces the perfect data set to search for these long-term perturbations.

This thesis is focused on the automatic detection of TTVs in short-term observations and in multi-mission and long-term observations of extraso-

lar multi-planet systems, and their characterization by the inversion of the TTV signal.

6.1. Summary of the results

An open-source package, Python Tool for Transit Variations (`PyTTV`), was developed to (1) search and identify transit variations (TTVs, TDVs, and TPVs) automatically and (2) estimate the physical quantities of planets in multi-planet systems based on the derived TTVs. `PyTTV` can process the increasing amount of light curves from past, current, and upcoming exoplanet missions for which a manual search is impractical. `PyTTV` is suitable for the search for variations in light curves observed in different cadences, with different noise properties, and from different telescopes, putting it in an excellent position for the search of transit variations using current and upcoming facilities. `PyTTV` determines the physical quantities of planets in multi-planet systems by an n-body orbit integration that considers the gravitational forces, the effects of general relativity, and tidal interactions to cover both short-term and long-term perturbations in planetary systems. This will become increasingly important in the future when more data from different missions to cover long term perturbations will be available.

Detection of transit variations It has been proven that `PyTTV` can detect short-term and long-term transit variations in various kind of systems:

- short-term TTVs in multi-planet systems with planets close to a first-order MMR (Kepler-9 and K2-146).

- short-term TTVs and TDVs in multi-planet systems with planets with period ratios far from a period commensurability with an atypical periodicity (Kepler-117).

- short-term TTVs, TDVs, and TPVs in multi-planet systems with eccentric planets (Kepler-693).

- short-term TTVs and TDVs in multi-planet systems with planets close to a first-order MMR (Kepler-88).

- short-term TTVs in multi-planet systems with eccentric planets (Kepler-448).

- long-term TTVs in multi-planet systems with outer companions (HAT-P-7).

- long-term TDVs and short-term TTVs in single-planet systems (Kepler-13).

The accuracy of transit times estimated by `PyTTV` is comparable to other literature values and methods. The comparison with the findings by other authors revealed that `PyTTV` functions efficiently and identifies near-automatically all kinds of transit variations (Kepler-9, Kepler-117, Kepler-88, Kepler-448, and Kepler-693). This places it between the leading codes for TTV estimation.

For the first time, a TTV search has been carried out for the systems TOI-1130, TOI-1136, and WASP-126 using all the available *TESS* light curves. No transit variations were found in the systems TOI-1130 and TOI-1136, even though strong TTVs are expected since the systems contain planets close to a period commensurability. Observations over a longer

time span are needed for further verification of those results. The non-detection of TTVs in the WASP-126 system contradicts the reported additional planet in Pearson (2019). One reason for the contradictory results could be that in Pearson (2019), only the first three Sectors of *TESS* light curves were analyzed, while here, 13 Sectors were considered. Kepler-448, HAT-P-7, and Kepler-13A are searched for variations using *Kepler* and *TESS* light curves combined for the first time. Besides the detection of TTVs, the non-detection of variations helps also to characterize the planetary systems, as shown for K2-180, K2-140, K2-100, K2-106, TOI-263, TOI-1130, TOI-1136, WASP-126 and WASP-18. The combination of various transit observations enables the search for long-term disturbances in the light curves caused by orbital precession or orbital decay, as presented for WASP-18b, HAT-P-7b, and Kepler-13Ab.

Characterization of multi-planet systems It is shown that `PyTTV` is able to estimate planetary parameters by modeling transit timing variations, transit duration variations, and radial velocity observations simultaneously. The simultaneous modeling of transit timing variations, transit duration variations, and radial velocity observations has been carried out for the Kepler-9, Kepler-289, and K2-146 systems for the first time.

Kepler-9 The system was modeled considering the gravitational interaction between Kepler-9b and Kepler-9c, but neglecting the effects of the close-in planet Kepler-9d. Kepler-9d was found not to affect the orbits of Kepler-9b and Kepler-9c based on forward modeling with `PyTTV`. In addition to the gravitational forces, the effect of GR was included in the parameter estimation, since its influence was tested with forward modeling with `PyTTV` and found to be of the order

of the uncertainties in the TTVs. The analysis includes the *Kepler* photometry and all available RV measurements, modeled simultaneously for the first time. The influence of the different observations (TTVs, TDVs, and RVs) on the estimated parameters and their uncertainties was studied.

Studying the influence of the TTVs, TDVs, and RVs revealed that modeling TTVs and TDVs simultaneously and modeling of TTVs, TDVs, and RVs simultaneously lead to values for the planet parameters that are indistinguishable between scenarios. As a final result for the parameters, the solution using TTVs, TDVs, and RVs is chosen because all available information is included in the fit. `PyTTV` estimated a planetary mass of $M_\mathrm{p} = 43.6 \pm 0.4\,\mathrm{M}_\oplus$ and $M_\mathrm{p} = 30.0 \pm 0.3\,\mathrm{M}_\oplus$, and $e = 0.0630 \pm 0.0006$ and $e = 0.06787 \pm 0.00007$ for Kepler-9b and Kepler-9c, respectively. These results agree well with the results from Borsato et al. (2019) and Freudenthal et al. (2018), respectively, but with smaller uncertainties.

Kepler-289 The planets are too far away from the star to be influenced by GR as confirmed by `PyTTV` forward modeling. The forward modeling with `PyTTV` also resulted in the neglect of the tidal influence of the outer on the middle planet in this analysis. Therefore, only gravitational forces were used for the `PyTTV` analysis. The influence of TTVs, TDVs, and RVs on the parameter extraction was studied, because so far the system was only analyzed via TTVs or RVs alone.

The simultaneous modeling of the TTVs, TDVs, and RVs for Kepler-289 shows that the inclusion of the RV measurements improves the parameter estimation, in particular for planetary mass and eccen-

tricity. Also, the transit duration measurements help to constrain the orbital inclination. Allowing for eccentric orbits favors non-zero eccentricity for the innermost planet and moderate eccentricities for the outer planets. In addition, allowing for eccentric orbits significantly improved the mass estimate for the inner planet. The simulation revealed the lower limit for the mass of the inner planet was not constrain if forcing circular orbits. As a final result, the solution using TTVs, TDVs, and RVs is chosen because all available information is included in the fit. The analysis of the system using TTVs, TDVs, and RVs leads to more constrained values for the planetary masses for all the planets with significantly smaller uncertainties. `PyTTV` estimated planetary masses of $M_{\rm p} = 1.5 \pm 0.9\,{\rm M}_{\oplus}$, $M_{\rm p} = 3.6 \pm 0.4\,{\rm M}_{\oplus}$, and $M_{\rm p} = 115 \pm 8\ {\rm M}_{\oplus}$, and $e = 0.12 \pm 0.04$, $e = 0.021 \pm 0.006$, and $e = 0.012 \pm 0.004$ for Kepler-289b, Kepler-289d, and Kepler-289c, respectively.

The discrepancy in the mass of the outer planet found by Santerne et al. (2016) disappears. The solution for the planet mass found by `PyTTV` assuming circular orbits agrees within 3σ with the value derived from the RVs by Santerne et al. (2016). This highlights the importance of individual analysis and re-analysis for systems where TTVs and RVs lead to disagreeing values. The TTV and RV discrepancy could be solved, simply through a re-analysis and including eccentric orbits.

K2-146 The system was modeled considering the gravitational forces between the planets. Forward modeling with `PyTTV` ruled out the influence of GR and tidal interactions. The simultaneous modeling using the TTVs and TDVs was carried out for the first time. Since

no chopping signal that would break the mass-eccentricity ambiguity was detected in the TTVs, the influence on the planetary masses by different priors on the eccentricity has been studied for TTVs and for the combination of TTVs and TDVs.

The PyTTV analysis for K2-146 showed that the solution is sensitive to the choice of eccentricity priors. Nevertheless, the planetary masses are well-constrained and do not change significantly. As a final result for the parameters, the solution using TTVs and TDVs is chosen because the least restrictive prior on the eccentricities is used, and all available information is included in the fit. PyTTV estimated planetary masses of $M_{\rm p} = 6.50 \pm 0.06\,{\rm M}_{\oplus}$ and $M_{\rm p} = 8.5 \pm 0.1\,{\rm M}_{\oplus}$, and $e = 0.05 \pm 0.01$ and $e = 0.13 \pm 0.01$ for K2-146b and K2-146c, respectively. These results differ from the values in Lam et al. (2020) and Hamann et al. (2019). The reason for this discrepancy can be explained by the choice of different priors on the eccentricities, because the parameter estimation is sensitive to the choice of a prior.

These examples of Kepler-9, Kepler-289, and K2-146 showed the capabilities and accuracy of the TTV parameter estimation by PyTTV. These systems are shown in the mass-radius and mass-period diagram in Fig. 6.1, where Kepler-9b and Kepler-9c (red squares), and K2-146b and K2-146c (green diamonds) lie on the border separating low-mass TTV planets and higher mass RV planets. The PyTTV estimated masses fit perfectly to the sample of well-determined systems. The inner planets for Kepler-289 (red triangles) have one of the lowest well-constrained masses obtained by combing TTVs and RVs. The mass-density diagram is shown in Fig. 6.2. The K2-146 planets are in the upper left, the Kepler-9 planets are just

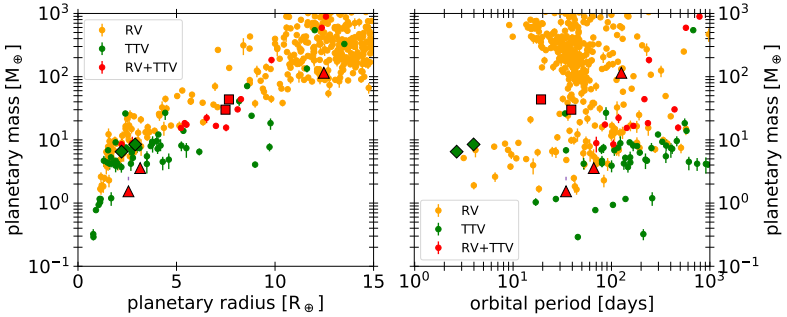

Figure 6.1.: Mass-radius (left) and mass-period (right) diagram for mass determinations better to 30% from RVs (yellow), TTVs (green), and a combination of both methods (red). The data are taken from the TEPCat catalog(Southworth, 2011) and have been checked and updated with literature values. Diamonds, squares, and triangles symbolize the planets of the K2-146, Kepler-9, and Kepler-289 system, respectively. The colors indicate the kind of observation used by `PyTTV` to estimate their planetary masses.

above the line for the theoretical relationship for H/He dominated giant objects, and the inner planets of the Kepler-289 system are in the lower left quadrant.

Kepler-9 and Kepler-289 represent two systems where the planet masses and eccentricities can be determined uniquely using TTVs alone due to the chopping effect. The inclusion of TDVs helps to constrain the orbital parameters which cannot be constrained via TTVs alone. While the inclusion of the RV does not significantly change the estimated parameters for Kepler-9, the values for Kepler-289 are improved.

Furthermore, the examples of Kepler-289 and K2-146 show how crucial the choice of priors is. K2-146 represents a system where the orbital parameters are sensitive to the choice of priors on the eccentricity. However, the planetary masses are well-constrained. Fitting circular orbits for the

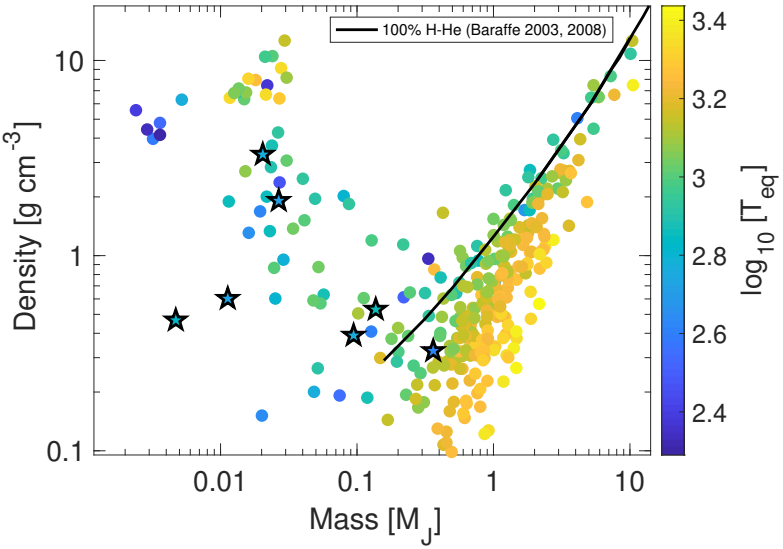

Figure 6.2.: Mass-density diagram for planets with a precision in measured mass and density $< 20\%$. The star symbols mark the locations of the planets from Kepler-9, Kepler-289, and K2-146. The black line represents the theoretical relation for H-He dominated giant planets without irradiation from Baraffe et al. (2003, 2008). The planets are color-coded according to their equilibrium temperatures, T_{eq}.

planets in Kepler-289 system leads to miscalculated values for the planetary mass, although the chopping signal would allow a robust parameter estimation. Allowing for eccentric orbits solved the previously found discrepancy in values for the planet mass derived from TTVs and RVs separately. This highlights the importance of the re-analysis for systems where TTVs and RVs lead to disagreeing values. Besides additional planets in the systems or additional physical mechanism as GR or tidal interactions,

the TTV and RV discrepancy can simply be solved through a re-analysis with a larger parameter space. The most important result is that due to the wide parameter space and the ambiguities between the parameters, a careful TTV analysis is required to estimate planetary properties, since they are needed for the characterization of the internal structure, composition, and density of the planet. Accurate and robustly estimated planetary parameters are in turn essential for understanding the evolution, formation, and migration of planetary systems. The theories developed to explain the observed diversity in orbital configurations and planetary densities (Super-Earth, Sub-Neptune, hot Jupiter, warm Jupiter, ultra-short-period planets) rely on the currently characterized systems, in particular on the accuracy with which the planet mass, planet radius, and orbital parameters are determined. Reducing the uncertainties, as shown in this work, is a large step forward for the development of formation and migration theories.

6.2. Future prospects

The developed software `PyTTV` enables the automated search for variations in the transit times, durations, and depths in past (*Kepler* and *K2*), current (*TESS*), and upcoming (*CHEOPS* and *PLATO*) missions. It also allows the subsequent parameter estimation from the identified variations and additional RV observations.

Detection of transit variations

Kepler The search for long-term transit variation presented here for Kepler-13, WASP-18, and HAT-P-7 can be extended to all available *Kepler* light curves in combination with *TESS* observations. The long ob-

servation time span of ten years enables the search for effects from orbit precession and tidal interaction, e.g., orbital decay. This opens a new area in the characterization of planetary systems and helps to understand the evolution and formation of planetary systems.

K2 `PyTTV` can be applied to search the light curves from the *K2* mission systematically for transit variations. No such search has been carried out to date.

TESS `PyTTV` can be applied to search the light curves from the *TESS* mission systematically for transit variations. Such a search would be beneficial for the targets that are observed by *TESS* for a longer period, as here suggested for TOI-1130.

Characterization of multi-planet systems

Kepler `PyTTV` can be used to re-analyze TTV systems where a discrepancy in the planetary parameters has been found or where the planetary density seems to be nonphysical, e.g., too high or too low (Jontof-Hutter et al., 2014; Masuda, 2014).

TESS Since *TESS* observes targets that are on average brighter compared to *Kepler* and *K2*, it is possible to combine high-precision RV observations and TTV observations for the first time for a large set of planets. This opens a completely new world where `PyTTV` can be used to accurately estimate the planetary parameters.

CHEOPS `PyTTV` can be used to characterize systems based on new transit measurements from *CHEOPS* for planets with known TTVs, where so far no robust parameter estimation has been possible.

Development of `PyTTV` The development of open-source Tool, `PyTTV`, will continue to fulfill any requirements made by further observations.

Astrometry Allowing for astrometric measurements in the parameter extraction can help to constrain the planetary masses and orbital elements

Photodynamical model `PyTTV` will optionally fit the photometry instead of the transit times and durations for tightly packed systems where overlapping transits occur often and complicate accurate estimation of their transit times.

Secondary eclipses The modeling of secondary eclipses will be implemented to further constrain the eccentricity.

This thesis has shown the capability to identify short-term and long-term transit variations and to characterize multi-planet systems using `PyTTV`. The capabilities of `PyTTV` shown in this work are only the beginning. With the upcoming missions, like *PLATO* and *CHEOPS*, and additional data from *TESS*, an increasing number of combined light curves with long baselines are available. This will improve the chances to detect long-term effects caused by GR and tidal interaction. PyTTV is the tool of choice to detect and analyze these effects.

Appendices

A

Abbreviations

Table A.1.: Symbols used in the text along with their definitions

Symbol	Definition
α	Semi-major axis ratio
Θ	Function of orbital elements
ϑ	Correction factor
ν	True Anomaly of the orbit
λ	Sky-projected spin–orbit misalignment
$\rho_\star$	Stellar density
ρ_p	Planetary density
σ	Standard deviation of the normal distribution
ψ	Obliquity
ω	Argument of periastron of the orbit
ω_0	Argument of the periastron at the transit epoch
a	Semi-major axis of the orbit
a_sync	Semi-major axis of the synchronous orbit

Continued on next page

Table A.1 – continued from previous page

Symbol	Definition
$b = b'$	Impact parameter
c	Speed of light in vacuum
D_{p}	Doodson constant
e	Eccentricity of the orbit
f	Oblateness factor
F	Perturbation Function
$F_{\star}$	Stellar property factor
G	Newtonian constant of gravitation
g_{p}	Planetary surface gravity
i	Inclination of the orbit to the plane of the sky
$i_{\star}$	Inclination of the stellar angular momentum to the plane of the sky
J_2	Quadrupole mass moment
k	Squared radius ratio
$k^2 \sim \Delta F$	Transit depth
k_2	Apsidal motion constant
$k_{2,\star}$	Stellar Love number
$k_{2,\mathrm{p}}$	Planetary Love number
K	Radial velocity amplitude
$M_{\star}$	Stellar mass
M_{p}	Planetary mass
M_{Jup}	Jupiter mass
n	Mean motion of the orbit, mean orbital angular velocity

Continued on next page

Table A.1 – continued from previous page

Symbol	Definition
N	Transit number
$Q_\star$	Dissipation factor
$Q'_\star$	Tidal quality factor
p, q	Integers
P_{rot}	Rotational period
P_{TTV}	Period of the TTV
$P_{\mathbf{orb}}$	Orbital period
r	Orbital separation
$R_\star$	Stellar radius
R_{p}	Planetary radius
R_{eq}	Equatorial radius
R_{pol}	Polar radius
t	Transit time
t_0	Time of first transit
t_{d}	Transit duration
t_{F}	Full transit duration
t_{T}	Total transit duration
T_{eq}	Equilibrium temperature
v_{tan}	Tangential velocity during transit

Bibliography

Adams, E. R., López-Morales, M., Elliot, J. L., Seager, S., & Osip, D. J. 2010, Astrophysical Journal, 714, 13

Adams, E. R., López-Morales, M., Elliot, J. L., Seager, S., & Osip, D. J. 2011a, Astrophysical Journal, 728, 125

Adams, E. R., López-Morales, M., Elliot, J. L., et al. 2011b, Astrophysical Journal, 741, 102

Adams, J. C. 1846, Monthly Notices of the Royal Astronomical Society, 7, 149

Agol, E. & Deck, K. 2016, The Astrophysical Journal, 818, 177

Agol, E. & Fabrycky, D. C. 2018, in Handbook of Exoplanets (Springer International Publishing AG), 797–816

Agol, E., Steffen, J., Sari, R., & Clarkson, W. 2005, Monthly Notices of the Royal Astronomical Society, 359, 567

Agol, E. & Steffen, J. H. 2007, Monthly Notices of the Royal Astronomical Society, 374, 941

Albrecht, S., Winn, J. N., Johnson, J. A., et al. 2012, Astrophysical Journal, 757, 18

Almenara, J. M., Diáz, R. F., Bonfils, X., & Udry, S. 2016, Astronomy and Astrophysics, 595

Almenara, J. M., Díaz, R. F., Dorn, C., Bonfils, X., & Udry, S. 2018a, Monthly Notices of the Royal Astronomical Society, 478, 460

Almenara, J. M., Díaz, R. F., Hébrard, G., et al. 2018b, Astronomy & Astrophysics, 615, A90

Almenara, J. M., Díaz, R. F., Mardling, R., et al. 2015, Monthly Notices of the Royal Astronomical Society, 453, 2644

Alonso, R. 2018, in Handbook of Exoplanets (Springer International Publishing), 1441–1467

Andert, T. P., Rosenblatt, P., Pätzold, M., et al. 2010, Geophysical Research Letters, 37

Angerhausen, D., DeLarme, E., & Morse, J. A. 2015, Publications of the Astronomical Society of the Pacific, 127, 1113

Arras, P., Burkart, J., Quataert, E., & Weinberg, N. N. 2012, Monthly Notices of the Royal Astronomical Society, 422, 1761

Auvergne, M., Bodin, P., Boisnard, L., et al. 2009, Astronomy and Astrophysics, 506, 411

Bailey, A. & Goodman, J. 2019, Monthly Notices of the Royal Astronomical Society, 482, 1872

Bakos, G. Á., Howard, A. W., Noyes, R. W., et al. 2009, Astrophysical Journal, 707, 446

Bakos, G. Á., Noyes, R. W., Kovács, G., et al. 2004, Publications of the Astronomical Society of the Pacific, 116, 266

Ballard, S., Christiansen, J. L., Charbonneau, D., et al. 2010, Astrophysical Journal, 716, 1047

Ballard, S., Fabrycky, D., Fressin, F., et al. 2011, Astrophysical Journal, 743, 200

Baraffe, I., Chabrier, G., & Barman, T. 2008, Astronomy and Astrophysics, 482, 315

Baraffe, I., Chabrier, G., Barman, T. S., Allard, F., & Hauschildt, P. H. 2003, Astronomy and Astrophysics, 402, 701

Barker, A. J. & Ogilvie, G. I. 2009, Monthly Notices of the Royal Astronomical Society, 395, 2268

Barnes, J. W., Linscott, E., & Shporer, A. 2011, Astrophysical Journal, Supplement Series, 197, 10

Barragán, O., Aigrain, S., Kubyshkina, D., et al. 2019, Monthly Notices of the Royal Astronomical Society, 490, 698

Barriot, J. P., Valès, N., Balmino, G., & Rosenblatt, P. 1998, Geophysical Research Letters, 25, 3743

Barros, S. C., Almenara, J. M., Demangeon, O., et al. 2015, Monthly Notices of the Royal Astronomical Society, 454, 4267

Barros, S. C. C., Díaz, R. F., Santerne, A., et al. 2014, Astronomy & Astrophysics, 561, L1

Batalha, N. M., Rowe, J. F., Bryson, S. T., et al. 2013, Astrophysical Journal, Supplement Series, 204, 24

Batista, V. 2018, in Handbook of Exoplanets (Springer International Publishing), 659–687

Bean, J. L. 2009, Astronomy and Astrophysics, 506, 369

Becker, J. C. & Adams, F. C. 2017, Monthly Notices of the Royal Astronomical Society, 468, 549

Becker, J. C., Vanderburg, A., Adams, F. C., Rappaport, S. A., & Schwengeler, H. M. 2015, Astrophysical Journal Letters, 812, L18

Benomar, O., Masuda, K., Shibahashi, H., & Suto, Y. 2014, Publications of the Astronomical Society of Japan, 66, 94

Biersteker, J. & Schlichting, H. 2017, The Astronomical Journal, 154, 164

Birkby, J. L. 2018, in Handbook of Exoplanets (Springer International Publishing), 1485–1508

Birkby, J. L., Cappetta, M., Cruz, P., et al. 2014, Monthly Notices of the Royal Astronomical Society, 440, 1470

Bonomo, A. S., Desidera, S., Benatti, S., et al. 2017, Astronomy and Astrophysics, 602, A107

Borkovits, T., Csizmadia, S., Forgács-Dajka, E., & Hegedüs, T. 2011, Astronomy & Astrophysics, 528, A53

Borkovits, T., Érdi, B., Forgács-Dajka, E., & Kovács, T. 2003, Astronomy and Astrophysics, 398, 1091

Borsato, L., Malavolta, L., Piotto, G., et al. 2019, Monthly Notices of the Royal Astronomical Society, 484, 3233

Borsato, L., Marzari, F., Nascimbeni, V., et al. 2014, Astronomy and Astrophysics, 571, A38

Borucki, W. J., Koch, D., Basri, G., et al. 2010, Science, 327, 977

Borucki, W. J., Koch, D., Jenkins, J., et al. 2009, Science, 325, 709

Borucki, W. J., Koch, D. G., Basri, G., et al. 2011a, Astrophysical Journal, 728, 117

Borucki, W. J., Koch, D. G., Basri, G., et al. 2011b, Astrophysical Journal, 736, 19

Bouma, L. G., Winn, J. N., Baxter, C., et al. 2019, The Astronomical Journal, 157, 217

Bourrier, V., Lecavelier Des Etangs, A., Hébrard, G., et al. 2015, Astronomy and Astrophysics, 579, A55

Brown, A. G., Vallenari, A., Prusti, T., et al. 2018, Astronomy and Astrophysics, 616, A1

Bruno, G., Almenara, J.-M., Barros, S. C. C., et al. 2015, Astronomy & Astrophysics, 573, A124

Carter, J. A., Agol, E., Chaplin, W. J., et al. 2012, Science, 337, 556

Carter, J. A. & Winn, J. N. 2010, Astrophysical Journal, 716, 850

Chen, J. & Kipping, D. 2017, The Astrophysical Journal, 834, 17

Cochran, W. D., Fabrycky, D. C., Torres, G., et al. 2011, Astrophysical Journal, Supplement Series, 197, 7

Contreras, A. P. G. & Boley, A. C. 2018, The Astronomical Journal, 155, 139

Correia, A. C. M., Delisle, J.-B., & Laskar, J. 2018, in Handbook of Exoplanets (Springer International Publishing), 2693–2711

Croll, B., Rappaport, S., & Levine, A. M. 2015, Monthly Notices of the Royal Astronomical Society, 449, 1408

Csizmadia, S., Hellard, H., & Smith, A. M. 2019, Astronomy and Astrophysics, 623, 1

Csizmadia, S., Renner, S., Barge, P., et al. 2010, Astronomy and Astrophysics, 510, 1

Cubillos, P., Erkaev, N. V., Juvan, I., et al. 2017, Monthly Notices of the Royal Astronomical Society, 466, 1868

Cumming, A., Marcy, G. W., & Butler, R. P. 1999, The Astrophysical Journal, 526, 890

Dai, F., Masuda, K., Winn, J. N., & Zeng, L. 2019, The Astrophysical Journal, 883, 79

Dai, F., Winn, J. N., Arriagada, P., et al. 2015, Astrophysical Journal Letters, 813, L9

Dai, F., Winn, J. N., Berta-Thompson, Z., Sanchis-Ojeda, R., & Albrecht, S. 2018, The Astronomical Journal, 155, 177

Damiani, C. & Lanza, A. F. 2011, Astronomy and Astrophysics, 535, A116

Dawson, R. I. 2018, in Handbook of Exoplanets (Springer International Publishing), 2713–2730

Dawson, R. I., Johnson, J. A., Fabrycky, D. C., et al. 2014, Astrophysical Journal, 791, 89

Deck, K. M. & Agol, E. 2015, Astrophysical Journal, 802, 116

Deck, K. M. & Agol, E. 2016, The Astrophysical Journal, 821, 96

Deck, K. M., Agol, E., Holman, M. J., & Nesvorný, D. 2014, Astrophysical Journal, 787, 132

Delisle, J. B., Correia, A. C., Leleu, A., & Robutel, P. 2017, Astronomy and Astrophysics, 605, A37

Delisle, J. B. & Laskar, J. 2014, Astronomy and Astrophysics, 570, L7

Denham, P., Naoz, S., Hoang, B. M., Stephan, A. P., & Farr, W. M. 2019, Monthly Notices of the Royal Astronomical Society, 482, 4146

Dobbs-Dixon, I., Lin, D. N. C., & Mardling, R. A. 2004, The Astrophysical Journal, 610, 464

Doyle, L. R. & Deeg, H.-J. 2004, Symposium - International Astronomical Union, 213, 80

Dreizler, S. & Ofir, A. 2014, ArXiv e-prints

Eggleton, P. P., Kiseleva, L. G., & Hut, P. 1998, Astrophysical Journal, 499, 853

Einstein, A. 1916, Annalen der Physik, 354, 769

Espinoza, N., Kossakowski, D., & Brahm, R. 2019, Monthly Notices of the Royal Astronomical Society, 490, 2262

Essick, R. & Weinberg, N. N. 2015, The Astrophysical Journal, 816, 18

Esteves, L. J., De Mooij, E. J., & Jayawardhana, R. 2013, Astrophysical Journal, 772, 51

Fabrycky, D. C. 2010, in Exoplanets,, ed. S. Seager (Tucson, AZ: University of Arizona Press), 217–238

Fabrycky, D. C., Ford, E. B., Steffen, J. H., et al. 2012, Astrophysical Journal, 750, 114

Fabrycky, D. C., Lissauer, J. J., Ragozzine, D., et al. 2014, Astrophysical Journal, 790, 146

Faigler, S., Tal-Or, L., Mazeh, T., Latham, D. W., & Buchhave, L. A. 2013, Astrophysical Journal, 771, 26

Ford, E. B. 2014, Proceedings of the National Academy of Sciences of the United States of America, 111, 12616

Ford, E. B., Fabrycky, D. C., Steffen, J. H., et al. 2012a, Astrophysical Journal, 750, 113

Ford, E. B. & Holman, M. J. 2007, The Astrophysical Journal, 664, L51

Ford, E. B., Ragozzine, D., Rowe, J. F., et al. 2012b, Astrophysical Journal, 756, 185

Ford, E. B., Rowe, J. F., Fabrycky, D. C., et al. 2011, Astrophysical Journal, Supplement Series, 197, 2

Foreman-Mackey, D., Agol, E., Ambikasaran, S., & Angus, R. 2017, The Astronomical Journal, 154, 220

Foreman-Mackey, D., Hogg, D. W., Lang, D., & Goodman, J. 2013, Publications of the Astronomical Society of the Pacific, 125, 306

Foreman-Mackey, D., Morton, T. D., Hogg, D. W., Agol, E., & Schölkopf, B. 2016, The Astronomical Journal, 152, 206

Fortier, A., Beck, T., Benz, W., et al. 2014, in Space Telescopes and Instrumentation 2014: Optical, Infrared, and Millimeter Wave, Vol. 9143 (SPIE), 91432J

Freudenthal, J., von Essen, C., Dreizler, S., et al. 2018, Astronomy & Astrophysics, 618, A41

Freudenthal, J., von Essen, C., Ofir, A., et al. 2019, Astronomy & Astrophysics, 628, A108

Fukui, A., Narita, N., Tristram, P. J., et al. 2011, Publications of the Astronomical Society of Japan, 63, 287

Fulton, B. J. & Petigura, E. A. 2018, The Astronomical Journal, 156, 264

Fulton, B. J., Petigura, E. A., Howard, A. W., et al. 2017, The Astronomical Journal, 154, 109

Fulton, B. J., Shporer, A., Winn, J. N., et al. 2011, Astronomical Journal, 142, 84

Furlan, E. & Howell, S. B. 2017, The Astronomical Journal, 154, 66

Gajdoš, P., Vaňko, M., & Parimucha, Š. 2019, Research in Astronomy and Astrophysics, 19, 041

Gelman, A., Carlin, J. B., Stern, H. S., et al. 2013, Bayesian Data Anal. Third Ed., 3rd edn. (CRC Press), 667

Gibson, N. P., Pollacco, D., Simpson, E. K., et al. 2009, Astrophysical Journal, 700, 1078

Gibson, N. P., Pollacco, D., Simpson, E. K., et al. 2008, Astronomy and Astrophysics, 492, 603

Giles, H. A., Bayliss, D., Espinoza, N., et al. 2018, Monthly Notices of the Royal Astronomical Society, 475, 1809

Goldreich, P. & Soter, S. 1966, Icarus, 5, 375

Griessmeier, J.-M. 2018, in Handbook of Exoplanets (Springer International Publishing), 3269–3283

Guenther, E. W., Barragán, O., Dai, F., et al. 2017, Astronomy and Astrophysics, 608, 1

Hadden, S., Barclay, T., Payne, M. J., & Holman, M. J. 2019, The Astronomical Journal, 158, 146

Hadden, S. & Lithwick, Y. 2014, Astrophysical Journal, 787, 1

Hadden, S. & Lithwick, Y. 2016, The Astrophysical Journal, 828, 44

Hadden, S. & Lithwick, Y. 2017, The Astronomical Journal, 154, 5

Hamann, A., Montet, B. T., Fabrycky, D. C., Agol, E., & Kruse, E. 2019, The Astronomical Journal, 158, 133

Hands, T. O. & Alexander, R. D. 2016, Monthly Notices of the Royal Astronomical Society, 456, 4121

Hatzes, A. P. 2016a, Space Science Reviews, 205, 267

Hatzes, A. P. 2016b, in Methods of Detecting Exoplanets, ed. S. A. Bozza V., Mancini L. (Springer, Cham), 3–86

Hellier, C., Anderson, D. R., Cameron, A. C., et al. 2009, Nature, 460, 1098

Herman, M. K., de Mooij, E. J. W., Huang, C. X., & Jayawardhana, R. 2018, The Astronomical Journal, 155, 13

Hermes, J. J. 2018, in Handbook of Exoplanets (Springer International Publishing), 787–796

Hernández, J. I. G., Pepe, F., Molaro, P., & Santos, N. 2018, in Handbook of Exoplanets (Springer International Publishing), 1–19

Heyl, J. S. & Gladman, B. J. 2007, Monthly Notices of the Royal Astronomical Society, 377, 1511

Hirano, T., Dai, F., Gandolfi, D., et al. 2018, The Astronomical Journal, 155, 127

Holczer, T., Mazeh, T., Nachmani, G., et al. 2016, The Astrophysical Journal Supplement Series, 225, 9

Holman, M. J., Fabrycky, D. C., Ragozzine, D., et al. 2010, Science, 330, 51

Holman, M. J. & Murray, N. W. 2005, Science, 307, 1288

Howell, S. B., Sobeck, C., Haas, M., et al. 2014, Publications of the Astronomical Society of the Pacific, 126, 398

Hoyer, S. & Hamman, J. J. 2017, Journal of Open Research Software, 5

Huang, C. X., Petrovich, C., & Deibert, E. 2017, The Astronomical Journal, 153, 210

Huber, D., Carter, J. A., Barbieri, M., et al. 2013, Science, 342, 331

Hunter, J. D. 2007, Computing in Science and Engineering, 9, 99

Hut, P. 1981, Astronomy and Astrophysics, 99, 126

Iorio, L. 2011a, Monthly Notices of the Royal Astronomical Society, 411, 167

Iorio, L. 2011b, Astrophysics and Space Science, 331, 485

Jackson, B., Greenberg, R., & Barnes, R. 2008, The Astrophysical Journal, 678, 1396

Jin, S. & Mordasini, C. 2018, The Astrophysical Journal, 853, 163

Johnson, M. C., Cochran, W. D., Albrecht, S., et al. 2014, Astrophysical Journal, 790, 30

Johnson, M. C., Cochran, W. D., Cameron, A. C., & Bayliss, D. 2015, Astrophysical Journal Letters, 810, L23

Jontof-Hutter, D., Ford, E. B., Rowe, J. F., et al. 2016, The Astrophysical Journal, 820, 39

Jontof-Hutter, D., Lissauer, J. J., Rowe, J. F., & Fabrycky, D. C. 2014, Astrophysical Journal, 785, 15

Jontof-Hutter, D., Rowe, J. F., Lissauer, J. J., Fabrycky, D. C., & Ford, E. B. 2015, Nature, 522, 321

Jontof-Hutter, D., Weaver, B. P., Ford, E. B., Lissauer, J. J., & Fabrycky, D. C. 2017, The Astronomical Journal, 153, 227

Jordan, A. & Bakos, G. A. 2008, Proceedings of the International Astronomical Union, 4, 492

Kane, M., Ragozzine, D., Flowers, X., et al. 2019, The Astronomical Journal, 157, 171

Kedziora-Chudczer, L., Zhou, G., Bailey, J., et al. 2019, Monthly Notices of the Royal Astronomical Society, 483, 5110

Kipping, D. M. 2009a, Monthly Notices of the Royal Astronomical Society, 392, 181

Kipping, D. M. 2009b, Monthly Notices of the Royal Astronomical Society, 396, 1797

Kipping, D. M. 2010, Monthly Notices of the Royal Astronomical Society, 408, 1758

Kipping, D. M. 2012, Monthly Notices of the Royal Astronomical Society, 427, 2487

Kipping, D. M. 2013, Monthly Notices of the Royal Astronomical Society: Letters, 434, L51

Knutson, H. A., Fulton, B. J., Montet, B. T., et al. 2014, Astrophysical Journal, 785, 126

Korth, J., Csizmadia, S., Gandolfi, D., et al. 2019, Monthly Notices of the Royal Astronomical Society, 482, 1807

Kozai, Y. 1968, Publications of the Astronomical Society of Japan, 42, 355

Kramm, U., Nettelmann, N., Redmer, R., & Stevenson, D. J. 2011, Astronomy and Astrophysics, 528, 1

Lai, D. & Pu, B. 2016, The Astronomical Journal, 153, 42

Lam, K. W. F., Korth, J., Masuda, K., et al. 2020, The Astronomical Journal, 159, 120

Laskar, J., Boué, G., & Correia, A. C. 2012, Astronomy and Astrophysics, 538, A105

Lazio, T. J. W. 2018, in Handbook of Exoplanets (Springer International Publishing), 817–833

Le Verrier, U. J. 1859, Annales de l'Observatoire Imperial de Paris, Recherches Astronomiques, Chapitre XV, 5, 1

Le Verrier, U. J. 1877, Annales de l'Observatoire de Paris, 14, 1

Lee, M. H., Fabrycky, D., & Lin, D. N. 2013, Astrophysical Journal, 774, 52

Leleu, A., Lillo-Box, J., Sestovic, M., et al. 2019, Astronomy and Astrophysics, 624, A46

Levrard, B., Winisdoerffer, C., & Chabrier, G. 2009, Astrophysical Journal, 692, L9

Linial, I., Gilbaum, S., & Sari, R. 2018, The Astrophysical Journal, 860, 16

Lissauer, J. J., Fabrycky, D. C., Ford, E. B., et al. 2011, Nature, 470, 53

Lissauer, J. J., Jontof-Hutter, D., Rowe, J. F., et al. 2013, Astrophysical Journal, 770, 131

Lissauer, J. J., Marcy, G. W., Rowe, J. F., et al. 2012, Astrophysical Journal, 750, 112

Lithwick, Y., Xie, J., & Wu, Y. 2012, Astrophysical Journal, 761, 122

Livingston, J. H., Endl, M., Dai, F., et al. 2018, The Astronomical Journal, 156, 78

Lomb, N. R. 1976, Astrophysics and Space Science, 39, 447

Lopez, E. D. & Fortney, J. J. 2013, Astrophysical Journal, 776, 2

Love, A. E. H. 1911, Some Problems of Geodynamics Publisher: Cambridge University Press

Maciejewski, G., Dimitrov, D., Fernández, M., et al. 2016, Astronomy and Astrophysics, 588, L6

Maciejewski, G., Dimitrov, D., Neuhäuser, R., et al. 2010, Monthly Notices of the Royal Astronomical Society, 407, 2625

Maciejewski, G., Dimitrov, D., Neuhäuser, R., et al. 2011, Monthly Notices of the Royal Astronomical Society, 411, 1204

Maciejewski, G., Fernández, M., Aceituno, F., et al. 2018, Acta Astronomica, 68, 371

Malavolta, L., Borsato, L., Granata, V., et al. 2017, The Astronomical Journal, 153, 224

Malbet, F. & Sozzetti, A. 2018, in Handbook of Exoplanets (Springer International Publishing), 689–704

Malhotra, R. 2015, Astrophysical Journal, 808, 71

Mandel, K. & Agol, E. 2002, The Astrophysical Journal, 580, L171

Mardling, R. A. 2007, Monthly Notices of the Royal Astronomical Society, 382, 1768

Masuda, K. 2014, Astrophysical Journal, 783, 2

Masuda, K. 2015, Astrophysical Journal, 805, 28

Masuda, K. 2017, The Astronomical Journal, 154, 64

Matsumura, S., Peale, S. J., & Rasio, F. A. 2010, Astrophysical Journal, 725, 1995

Maxted, P. F., Anderson, D. R., Collier Cameron, A., et al. 2016, Astronomy and Astrophysics, 591, A55

Maxted, P. F., Anderson, D. R., Doyle, A. P., et al. 2013, Monthly Notices of the Royal Astronomical Society, 428, 2645

Mayo, A. W., Vanderburg, A., Latham, D. W., et al. 2018, The Astronomical Journal, 155, 136

Mayor, M. & Queloz, D. 1995, Nature, 378, 783

Mazeh, T., Nachmani, G., Holczer, T., et al. 2013, Astrophysical Journal, Supplement Series, 208, 16

Mazeh, T., Nachmani, G., Sokol, G., Faigler, S., & Zucker, S. 2012, Astronomy and Astrophysics, 541, A56

McDonald, I. & Kerins, E. 2018, Monthly Notices of the Royal Astronomical Society: Letters, 477, L21

McKinney, W. 2010in , 51–56

McLaughlin, D. B. 1924, The Astrophysical Journal, 60, 22

Meibom, S. & Mathieu, R. D. 2005, The Astrophysical Journal, 620, 970

Miller-Ricci, E., Rowe, J. F., Sasselov, D., et al. 2008, The Astrophysical Journal, 682, 593

Mills, S. M. & Fabrycky, D. C. 2017a, The Astronomical Journal, 153, 45

Mills, S. M. & Fabrycky, D. C. 2017b, The Astrophysical Journal, 838, L11

Mills, S. M., Fabrycky, D. C., Migaszewski, C., et al. 2016, Nature, 533, 509

Mills, S. M., Howard, A. W., Weiss, L. M., et al. 2019, The Astronomical Journal, 157, 145

Mills, S. M. & Mazeh, T. 2017, The Astrophysical Journal, 839, L8

Miralda-Escude, J. 2002, The Astrophysical Journal, 564, 1019

Mislis, D. & Hodgkin, S. 2012, Monthly Notices of the Royal Astronomical Society, 422, 1512

Montalto, M., Gregorio, J., Boué, G., et al. 2012, Monthly Notices of the Royal Astronomical Society, 427, 2757

Morris, B. M., Mandell, A. M., & Deming, D. 2013, Astrophysical Journal Letters, 764, L22

Morton, T. D., Bryson, S. T., Coughlin, J. L., et al. 2016, The Astrophysical Journal, 822, 86

Murray, C. D. & Dermott, S. F. 1999, Solar system dynamics (Cambridge, UK: Cambridge University Press), 592

Narita, N., Sato, B., Hirano, T., & Tamura, M. 2009, Publications of the Astronomical Society of Japan, 61, L35

Narita, N., Takahashi, Y. H., Kuzuhara, M., et al. 2012, Publications of the Astronomical Society of Japan, 64, L7

Nascimbeni, V., Cunial, A., Murabito, S., et al. 2013, Astronomy and Astrophysics, 549, A30

Nascimbeni, V., Piotto, G., Bedin, L. R., et al. 2011, Astronomy and Astrophysics, 532, A24

Nespral, D., Gandolfi, D., Deeg, H. J., et al. 2017, Astronomy and Astrophysics, 601, A128

Nesvorný, D. 2009, Astrophysical Journal, 701, 1116

Nesvorný, D. & Beaugé, C. 2010, Astrophysical Journal Letters, 709, 44

Nesvorný, D., Kipping, D., Terrell, D., & Feroz, F. 2014, Astrophysical Journal, 790, 31

Nesvorný, D., Kipping, D., Terrell, D., et al. 2013, Astrophysical Journal, 777, 3

Nesvorný, D. & Morbidelli, A. 2008, The Astrophysical Journal, 688, 636

Nesvorný, D. & Vokrouhlický, D. 2014, Astrophysical Journal, 790, 58

Nesvorný, D. & Vokrouhlický, D. 2016, The Astrophysical Journal, 823, 72

Neveu-VanMalle, M., Queloz, D., Anderson, D. R., et al. 2016, Astronomy and Astrophysics, 586, A93

Ni, D. 2018, Astronomy and Astrophysics, 613, A32

Nutzman, P. & Charbonneau, D. 2008, Publications of the Astronomical Society of the Pacific, 120, 317

Nymeyer, S., Harrington, J., Hardy, R. A., et al. 2011, Astrophysical Journal, 742, 35

Ofir, A., Dreizler, S., Zechmeister, M., & Husser, T. O. 2014, Astronomy and Astrophysics, 561, A103

Ofir, A., Xie, J.-W., Jiang, C.-F., Sari, R., & Aharonson, O. 2018, The Astrophysical Journal Supplement Series, 234, 9

Ogilvie, G. I. 2014, Annual Review of Astronomy and Astrophysics, 52, 171

Owen, J. E. & Wu, Y. 2013, Astrophysical Journal, 775, 105

Owen, J. E. & Wu, Y. 2017, The Astrophysical Journal, 847, 29

Pál, A. 2012, Monthly Notices of the Royal Astronomical Society, 420, 1630

Pál, A., Bakos, G. Á., Torres, G., et al. 2008, The Astrophysical Journal, 680, 1450

Pál, A. & Kocsis, B. 2008, Monthly Notices of the Royal Astronomical Society, 389, 191

Papaloizou, J. C. 2011, Celestial Mechanics and Dynamical Astronomy, 111, 83

Parviainen, H. 2015, Monthly Notices of the Royal Astronomical Society, 450, 3233

Parviainen, H. 2018, in Handbook of Exoplanets (Cham: Springer International Publishing), 1567–1590

Parviainen, H., Palle, E., Zapatero-Osorio, M. R., et al. 2020, Astronomy & Astrophysics, 633, A28

Patra, K. C., Winn, J. N., Holman, M. J., et al. 2017, The Astronomical Journal, 154, 4

Pätzold, M., Andert, T. P., Hahn, M., et al. 2019, Monthly Notices of the Royal Astronomical Society, 483, 2337

Pätzold, M., Carone, L., & Rauer, H. 2004, Astronomy and Astrophysics, 427, 1075

Pätzold, M. & Rauer, H. 2002, The Astrophysical Journal, 568, L117

Peale, S. J. 1999, Annual Review of Astronomy and Astrophysics, 37, 533

Pearson, K. A. 2019, The Astronomical Journal, 158, 243

Pérez, F. & Granger, B. E. 2007, Computing in Science and Engineering, 9, 21

Perryman, M. A. C. 2018, The Exoplanet Handbook, second edi edn. (Cambridge University Press), 952 p

Petigura, E. A., Benneke, B., Batygin, K., et al. 2018, The Astronomical Journal, 156, 89

Petigura, E. A., Howard, A. W., & Marcy, G. W. 2013, Proceedings of the National Academy of Sciences of the United States of America, 110, 19273

Petrovich, C. & Tremaine, S. 2016, The Astrophysical Journal, 829, 132

Petrovich, C., Tremaine, S., & Rafikov, R. 2014, Astrophysical Journal, 786, 101

Petrucci, R., Jofré, E., Ferrero, L. V., et al. 2018, Monthly Notices of the Royal Astronomical Society, 473, 5126

Pichierri, G., Batygin, K., & Morbidelli, A. 2019, Astronomy and Astrophysics, 625, A7

Piskunov, N. & Valenti, J. A. 2017, Astronomy and Astrophysics, 597, A16

Pollacco, D., Skillen, I., Cameron, A., et al. 2006, Publications of the Astronomical Society of the Pacific, 118, 1407

Pope, B. J., Parviainen, H., & Aigrain, S. 2016, Monthly Notices of the Royal Astronomical Society, 461, 3399

Price-Whelan, A. M., Sipőcz, B. M., Günther, H. M., et al. 2018, The Astronomical Journal, 156, 123

Pu, B. & Lai, D. 2018, Monthly Notices of the Royal Astronomical Society, 478, 197

Pueyo, L. 2018, in Handbook of Exoplanets (Cham: Springer International Publishing), 705–765

Rafikov, R. R. 2009, Astrophysical Journal, 700, 965

Ragozzine, D. & Holman, M. J. 2010, ArXiv e-prints

Ragozzine, D. & Wolf, A. S. 2009, The Astrophysical Journal, 698, 1778

Rappaport, S., Levine, A., Chiang, E., et al. 2012, Astrophysical Journal, 752, 1

Rauer, H., Catala, C., Aerts, C., et al. 2014, Experimental Astronomy, 38, 249

Rein, H. & Liu, S. F. 2012, Astronomy and Astrophysics, 537, A128

Rein, H. & Spiegel, D. S. 2015, Monthly Notices of the Royal Astronomical Society, 446, 1424

Ricker, G. R., Winn, J. N., Vanderspek, R., et al. 2014, Space Telescopes and Instrumentation 2014: Optical, Infrared, and Millimeter Wave, 9143, 914320

Robitaille, T. P., Tollerud, E. J., Greenfield, P., et al. 2013, Astronomy and Astrophysics, 558, A33

Rossiter, R. A. 1924, The Astrophysical Journal, 60, 15

Rowe, J. F., Bryson, S. T., Marcy, G. W., et al. 2014, The Astrophysical Journal, 784, 45

Rowe, J. F., Coughlin, J. L., Antoci, V., et al. 2015, Astrophysical Journal, Supplement Series, 217, 16

Santerne, A., Moutou, C., Tsantaki, M., et al. 2016, Astronomy and Astrophysics, 587, A64

Sartoretti, P. & Schneider, J. 1999, Astronomy and Astrophysics Supplement Series, 134, 553

Scargle, J. D. 1982, The Astrophysical Journal, 263, 835

Scharf, C. A. 2007, The Astrophysical Journal, 661, 1218

Schmitt, J. R., Agol, E., Deck, K. M., et al. 2014, Astrophysical Journal, 795, 167

Seager, S. & Mallen-Ornelas, G. 2003, The Astrophysical Journal, 585, 1038

Shakura, N. I. & I., N. 1985, SvAL, 11, 224

Shporer, A., Jenkins, J. M., Rowe, J. F., et al. 2011, Astronomical Journal, 142, 195

Shporer, A., Wong, I., Huang, C. X., et al. 2019, The Astronomical Journal, 157, 178

Silva Aguirre, V., Davies, G. R., Basu, S., et al. 2015, Monthly Notices of the Royal Astronomical Society, 452, 2127

Simon, A., Szatmáry, K., & Szabó, G. M. 2007, Astronomy and Astrophysics, 470, 727

Sinukoff, E., Howard, A. W., Petigura, E. A., et al. 2017a, The Astronomical Journal, 153, 271

Sinukoff, E., Howard, A. W., Petigura, E. A., et al. 2017b, The Astronomical Journal, 153, 70

Siverd, R. J., Beatty, T. G., Pepper, J., et al. 2012, Astrophysical Journal, 761, 123

Sotiriadis, S., Libert, A. S., Bitsch, B., & Crida, A. 2017, Astronomy and Astrophysics, 598, A70

Southworth, J. 2011, Monthly Notices of the Royal Astronomical Society, 417, 2166

Southworth, J., Hinse, T. C., Dominik, M., et al. 2009, Astrophysical Journal, 707, 167

Steffen, J. H. 2016, Monthly Notices of the Royal Astronomical Society, 457, 4384

Steffen, J. H. & Agol, E. 2005, Monthly Notices of the Royal Astronomical Society: Letters, 364, L96

Steffen, J. H., Batalha, N. M., Borucki, W. J., et al. 2010, Astrophysical Journal, 725, 1226

Steffen, J. H., Fabrycky, D. C., Agol, E., et al. 2013, Monthly Notices of the Royal Astronomical Society, 428, 1077

Steffen, J. H., Fabrycky, D. C., Ford, E. B., et al. 2012a, Monthly Notices of the Royal Astronomical Society, 421, 2342

Steffen, J. H., Ford, E. B., Rowe, J. F., et al. 2012b, Astrophysical Journal, 756, 186

Steffen, J. H. & Hwang, J. A. 2015, Monthly Notices of the Royal Astronomical Society, 448, 1956

Sterne, T. E. 1939, Monthly Notices of the Royal Astronomical Society, 99, 451

Struve, O. 1952, Proposal for a project of high-precision stellar radial velocity work

Szabó, G. M., Pál, A., Derekas, A., et al. 2012, Monthly Notices of the Royal Astronomical Society: Letters, 421, L122

Szabó, G. M., Simon, A., & Kiss, L. L. 2014, Monthly Notices of the Royal Astronomical Society, 437, 1045

Szabó, G. M., Szabó, R., Benk, J. M., et al. 2011, Astrophysical Journal Letters, 736, L4

Szabó, G. M., Szatmáry, K., Divéki, Z., & Simon, A. 2006, Astronomy and Astrophysics, 450, 395

Szabó, G. M., Theodor, Pribulla, et al. 2020, Monthly Notices of the Royal Astronomical Society: Letters, 492, L17

Szabó, R., Szabó, G. M., Dálya, G., et al. 2013, Astronomy and Astrophysics, 553, 1

Tamayo, D., Rein, H., Shi, P., & Hernandez, D. M. 2019, Monthly Notices of the Royal Astronomical Society, 491

Thompson, S. E., Coughlin, J. L., Hoffman, K., et al. 2018, The Astrophysical Journal Supplement Series, 235, 38

Uehara, S., Kawahara, H., Masuda, K., Yamada, S., & Aizawa, M. 2016, The Astrophysical Journal, 822, 2

Valsecchi, F. & Rasio, F. A. 2014, Astrophysical Journal Letters, 787, L9

Van Der Walt, S., Colbert, S. C., & Varoquaux, G. 2011, Computing in Science and Engineering, 13, 22

Van Eylen, V., Agentoft, C., Lundkvist, M. S., et al. 2018, Monthly Notices of the Royal Astronomical Society, 479, 4786

Van Eylen, V. & Albrecht, S. 2015, Astrophysical Journal, 808, 126

Van Eylen, V., Albrecht, S., Huang, X., et al. 2019, The Astronomical Journal, 157, 61

Van Eylen, V., Lindholm Nielsen, M., Hinrup, B., Tingley, B., & Kjeldsen, H. 2013, Astrophysical Journal Letters, 774, L19

Veras, D., Ford, E. B., & Payne, M. J. 2011, Astrophysical Journal, 727, 74

Virtanen, P., Gommers, R., Oliphant, T. E., et al. 2020, Nature Methods, 17, 261

Vissapragada, S., Jontof-Hutter, D., Shporer, A., et al. 2020, The Astronomical Journal, 159, 108

Wang, S., Addison, B., Fischer, D. A., et al. 2018, The Astronomical Journal, 155, 70

Waskom, M., Botvinnik, O., O'Kane, D., et al. 2018

Watson, C. A. & Marsh, T. R. 2010, Monthly Notices of the Royal Astronomical Society, 405, 2037

Weiss, L. M., Agol, E., Fabrycky, D. C., et al. 2019, ArXiv e-prints

Weiss, L. M., Deck, K. M., Sinukoff, E., et al. 2017, The Astronomical Journal, 153, 265

Weiss, L. M. & Marcy, G. W. 2014, Astrophysical Journal Letters, 783, L6

Welsh, W. F., Orosz, J. A., Seager, S., et al. 2010, Astrophysical Journal Letters, 713, L145

Wheatley, P. J., West, R. G., Goad, M. R., et al. 2018, Monthly Notices of the Royal Astronomical Society, 475, 4476

Wilkins, A. N., Delrez, L., Barker, A. J., et al. 2017, The Astrophysical Journal, 836, L24

Winn, J. N. 2010, in Exoplanets, ed. S. Seager (Tucson, AZ: University of Arizona Press), 55–77

Winn, J. N. 2018, in Handbook of Exoplanets (Springer International Publishing), 1949–1966

Winn, J. N., Johnson, J. A., Albrecht, S., et al. 2009, Astrophysical Journal, 703, L99

Wolszczan, A. & Frail, D. A. 1992, Nature, 355, 145

Wu, D.-H., Wang, S., Zhou, J.-L., Steffen, J. H., & Laughlin, G. 2018, The Astronomical Journal, 156, 96

Wu, Y. & Lithwick, Y. 2013, Astrophysical Journal, 772, 74

Xie, J.-W. 2013, The Astrophysical Journal Supplement Series, 208, 22

Xie, J. W. 2014, Astrophysical Journal, Supplement Series, 210, 25

Xie, J. W., Dong, S., Zhu, Z., et al. 2016, Proceedings of the National Academy of Sciences of the United States of America, 113, 11431

Xie, J. W., Wu, Y., & Lithwick, Y. 2014, Astrophysical Journal, 789, 165

Xu, W. & Fabrycky, D. 2019, ArXiv e-prints

Yang, M., Liu, H. G., Zhang, H., Yang, J. Y., & Zhou, J. L. 2013, Astrophysical Journal, 778, 110

Zahn, J. P. 1977, Astronomy and Astrophysics, 500, 121

Zechmeister, M. & Kürster, M. 2009, Astronomy and Astrophysics, 496, 577

Zhao, S., Jiang-hui, J., & Yao, D. 2018, Chinese Astronomy and Astrophysics, 42, 101

Zhu, W., Huang, C. X., Zhou, G., & Lin, D. N. 2014, Astrophysical Journal, 796, 67

Zhu, W., Petrovich, C., Wu, Y., Dong, S., & Xie, J. 2018, The Astrophysical Journal, 860, 101

Acknowledgments

Der Wunsch, mich mit der Charakterisierung von extrasolaren Planeten zu befassen, entstand während meiner Tätigkeit als studentische Hilfskraft beim RIU, wurde vertieft durch meine Masterarbeit auf diesem Gebiet und findet einen vorläufigen Abschluss in dieser Doktorarbeit.

Diese Doktorarbeit wäre ohne die Unterstützung von vielen Menschen nicht möglich gewesen, die mir in dieser Zeit zur Seite gestanden haben. Als erstes möchte ich meinem Doktorvater PD Dr. Martin Pätzold für die Möglichkeiten danken, die er mir mit der Arbeit in seinem Team eröffnet hat. Er hat mich in die Materie der extrasolaren Planeten eingeführt, mein Interesse dafür geweckt und mich ermutigt, mich eingehend mit dieser Thematik zu beschäftigen.

Herrn Prof. Dr. Joachim Saur gilt mein Dank für seine engagierte Übernahme des Ko-Referat und seine Orientierungshilfen in meinem gesamten Studium.

Meinen Kollegen, die immer ein offenes Ohr für meine wissenschaftlichen Fragen hatten, möchte ich für die vielen fruchtbaren Diskussionen danken. Die Unterstützung und Hinweise der Kollegen vom RIU, besonders Dr. Silvia Tellmann und Herrn Sascha Grziwa, ermöglichten mir die optimale Darstellung und Auswertung meiner Forschungsergebnisse. Herrn Sascha Grziwa möchte ich herzlich für seinen hilfreichen wissenschaftlichen Rat und seine konstruktive Kritik danken.

Ich danke meiner Mutter für ihre emotionale Unterstützung. Sie ist auch in schwierigen Situationen immer für mich da.

An dieser Stelle möchte ich allen danken, die die Fertigstellung meiner Dokorarbeit ermöglichten.

Erklärung

Ich versichere, dass ich die vorgelegte Dissertation selbststädig angefertigt, die benutzen Quellen und Hilfsmittel vollstandig angegeben und die Stellen der Arbeit - einschließlich Tabellen, Karten und Abbildungen -, die in anderen Werken im Wortlaut oder dem Sinn nach entnommen sind, in jedem Einzelfall als Entlehnung kenntlich gemacht habe; dass diese Dissertation noch keiner anderen Fakultät oder Universität zur Prüfung vorgelegen hat; dass sie - abgesehen von unten angegebenen Teilpublikationen - noch nicht veröffentlicht worden ist, sowie, dass ich eine solche Veröffentlichung vor Abschluss des Promotionsverfahrens nicht vornehmen werde. Die Bestimmungen der Promotionsordnung sind mir bekannt. Die von mir vorgelegte Dissertation ist von PD Dr. Martin Pätzold betreut worden.

Teilpublications:

1. Korth, J., Sz. Csizmadia, D. Gandolfi, et al.; K2-140b and K2-180b - Characterization of a hot Jupiter and a mini-Neptune from the K2 mission. *MNRAS*, 482, 1807–1823, 2019.

2. Lam, K. W. F., J. Korth, K. Masuda, et al., It takes two planets in resonance to tango around K2-146. *AJ*, 159, 120, 2020.

3. Parviainen, H., E. Palle, M. R. Zapatero-Osorio, et al., MuSCAT2

multicolour validation of TESS candidates: an ultra-short-period substellar object around an M dwarf. *A&A*, 633, A28, 2020.

4. Guenther, E. W., O. Barragán, F. Dai, et al., K2-106, a system containing a metal-rich planet and a planet of lower density. *A&A*, 608, 1–10, 2017.

5. Barragán, O., S. Aigrain, D. Kubyshkina, et al., Radial velocity confirmation of K2-100b: a young, highly irradiated, and low density transiting hot Neptune. *MNRAS*, 490, 698–708, 2019.

Ort, Datum

Unterschrift